INELASTIC NEUTRON SCATTERING

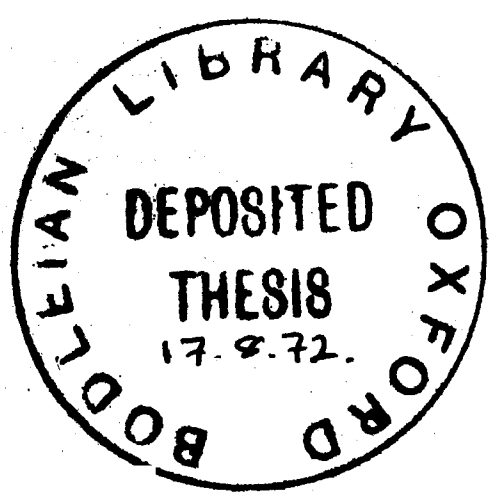
BY

MOLECULAR CRYSTALS

Ronen E. Ghosh

A thesis submitted for the Degree
of Doctor of Philosophy at Oxford
University.

St. John's College. April, 1972



ABSTRACT

High resolution optical data has long shown effects of the interactions in the crystalline state changing the vibrational energy levels of free molecules. With the advances in instrumentation optically active lattice modes may now be measured directly. Since the complementary techniques of electromagnetic scattering only yield information concerning modes at the Brillouin zone centre it is only possible to infer the correlated dynamics of molecules in crystals.

Inelastic scattering of neutrons, both coherently and incoherently, has been used to measure contributions from the full spectrum of the normal modes of vibration. In the first chapter the bases of the scattering process are presented, distinguishing between coherent and incoherent scattering. The differential cross-section is formulated in terms of the eigenstates of a harmonic oscillator. After describing the space-time correlation functions, the experimental scattering law is introduced.

The reduction of the lattice vibrations of atoms to normal modes of vibration using plane waves is given in chapter two, followed by the extension to include rigid molecules where the normal modes include librations as well as translations. The restriction imposed by symmetry is then discussed. The double differential cross-section for the phonon scattering by extending the harmonic oscillator formalism is given in chapter three.

The following chapters, four and five, are concerned with coherent neutron scattering experiments from a crystal of perdeutero urea. The use of a triple-axis spectrometer is shown to be unfavourable for the proposed measurements

compared with time-of-flight spectrometers. Two of the latter type instrument are compared. A simple structure and ease of deuteration are included in the reason for the choice of specimen: there follows an account of the successful growth from the melt. The results from the scattering experiments performed are succeeded by assignment of the phonon groups with the aid of optical data and symmetry arguments. The librational branches measured show very strong dispersion suggesting a possible onset of rotation in the solid phase.

Measurements of inelastic neutron scattering have been made on polycrystalline urea and urea (d_4) to study the temperature dependence of these effects. The study of scattering from polycrystalline materials is discussed invoking the incoherent approximation for coherent scatterers. To aid interpretation analogous measurements have been made for hexamethylene tetramine and naphthalene for comparison with the model descriptions of Pawley. The scattering from urea and urea (d_4) both show very much more marked temperature dependence than these two systems. This correlates with other physical data and the measured dispersion curves, and again indicates very large libration amplitudes at 295 K.

With hydrogen bonding being the dominant intermolecular force in urea analogous systems of oxamide and thiourea were also examined, at 295 K and the results of the first shown to be consistent with a very rigid lattice, while the second like urea shows some degree of rotation in the crystal.

The intramolecular modes of naphthalene have been measured using both neutron energy gain and loss spectroscopy and show some consistency with a model spectrum. The internal modes of urea and urea (d_4) have been measured and show strong

temperature effects attributed to the more compact and rigid lattice at the lower temperature.

Both coherent and incoherent experimental results show deficiencies in present model calculations, which may be ascribed to the necessary oversimplifications in their construction.

Contents

		Page No.
1.	Theory of Neutron Scattering	1
1.1	Coherent and Incoherent Scattering	2
1.2	Thermal Motion	4
1.3	Nuclear Bragg Scattering	4
1.4	Inelastic Scattering	7
1.5	Scattering by Vibrating Systems	8
1.6	Correlation Formulation	10
1.7	The Scattering Law	11
2.	Lattice Vibrations	14
2.1	Dynamics of Atoms in Crystals	14
2.2	Born von Karman Theory	14
2.3	Dynamics of Molecules in Crystals	17
2.4	Symmetry of Lattice Vibration	19
2.5	Properties of Phonons	21
3.	Neutron Scattering by Phonons	22
3.1	Elastic Scattering	22
3.2	The One Phonon Approximation	23
4.	Experimental Investigation of Normal Modes of Vibration with Neutrons	25
4.1	The Time of Flight Spectrometer	26
4.2	The PLUTO Twin Rotor Spectrometer 7H	27
4.3	The DIDO Cold Neutron Spectrometer 4H5	29
4.4	Comparison of 4H5 and 7H	30
4.5	Data Collection	36
4.6	Calibration of Spectrometer using Vanadium	36
4.7	The Pluto Triple-Axis Spectrometer	37
4.8	Choice of Specimen and Specimen Preparation	40
4.9	Analysis of Crystals	44
5.	Experiments with Single Crystals of Deutero-Urea	45
5.1	Measurements with the PLUTO Triple-Axis Spectrometer	45
5.2	Measurements with Time of Flight Spectrometers	46
5.2.1	Results in <001> Direction	47
5.2.2	Results in <110> Direction	49
5.3	Assignment of Modes	51
5.3.1	<001> Direction	59

		Page No.
	5.3.2 <110> Direction	60
	5.4 Discussion of Coherent Scattering Experiments	63
6.	Scattering by Polycrystalline Solids	65
	6.1 The Frequency Distribution	67
	6.2 Relationship between the Frequency Distribution and Optical Measurements	69
	6.3 Experimental Methods	70
	6.4 The Cold Neutron Spectrometer 4H5, and Long Wavelength Spectrometer 6H	71
	6.5 Sample Preparation and Mounting	72
	6.6 Data Reduction	74
	6.7 The Beryllium Filter Detector	77
7.	Measurement of Intermolecular Modes from Polycrystals	80
	7.1 Hexamethylenetetramine (HMT)	80
	7.2 Naphthalene	84
	7.3 Perdeutero-Naphthalene	88
	7.4 Urea	93
	7.5 Discussion of Urea Results	107
	7.6 Oxamide and Thiourea	115
8.	Measurement of intramolecular modes	120
	8.1 Naphthalene	120
	8.2 Urea	127
	8.3 Conclusions	130
Acknowledgements		133
References		134
List of Diagrams		138

CHAPTER 1

Theory of Neutron Scattering

1. Theory of Neutron Scattering

The basic theory has been given in several treatises, Turchin (1965); Egelstaff (1965), Marshall and Lovesey (1971); only the principal equations will be given here, treating an arbitrary number of atoms in the unit cell of the scatterer. Only direct neutron-nuclear interactions will be considered. The magnetic interaction of the neutron with electrons in unfilled shells as occur in transition metal and rare-earth compounds is not of relevance to the systems studied here.

The Schroedinger equation describing the wave function $\psi(r)$ of a scattered neutron from a fixed nucleus is

$$\left[\nabla^2 + k^2 - \frac{2m}{\hbar^2} V(r)\right] \psi(r') = 0 \qquad 1.1$$

where k is the scattered wavevector, m, the neutron mass, and V(r) the interaction potential at r' between the neutron and nucleus. At a distance r large compared with the range of this interaction the asymptotic solution represents the superposition of the incident plane wave

$$\psi_o = e^{ik_o r} \qquad 1.2$$

and the scattered spherical wave

$$\psi_o + \psi' = e^{ik_o r} - \frac{1}{4\pi} \int \frac{e^{ik(r-r')}}{r-r'} \frac{2m}{\hbar^2} V(r')\psi(r')dr' \qquad 1.3$$

Because the wavelength of thermal neutrons is many orders of magnitude greater than the interaction range, scattering involves only s wave components and is isotropic. This can be characterized by a single parameter as follows.

The flux of an incident beam of neutrons is equal to the number passing through a unit area perpendicular to the beam multiplied by the neutron velocity $v_o \propto k_o$. The flux of neutrons

scattered by a specimen is obtained by integrating over a portion of a sphere about r' at some large distance R. The cross-section σ is the ratio of outgoing to incoming fluxes.

$$\frac{d\sigma}{d\Omega} = \frac{k_1}{k_o} \left| \frac{1}{4\pi} \int_o^R e^{iQ.r} \cdot \frac{2m}{\hbar^2} V(r')\, dr' \right|^2 \qquad 1.4$$

when

$$Q = k_o - k_1$$

and

$$R = r - r'$$

Since $e^{iQ.r}$ will not differ much from unity for the small r' for which the interaction potential is finite, and

$$V(r') = \frac{2\pi}{m} \hbar^2 \delta(r').b.$$

$$\frac{1}{4\pi} \int_o^R e^{iQ.r} \frac{2m}{h} V(r')dr' = b \qquad 1.5$$

where b is a constant called the scattering length, and varies only from nucleus to nucleus. Although b is in general complex the imaginary part is usually negligible except for strong neutron absorbers. The total scattering cross-section for the nucleus is found by integration:

$$\sigma = 4\pi b^2 \qquad 1.6$$

The delta function formulation was invoked by Fermi as a 'pseudo potential' which would give in the Born approximation simple s wave scattering.

1.1 Coherent and Incoherent Scattering

The treatment of a static assembly of atoms must consider the effect of different nuclei (isotopes or elements), possibly with nuclear spin and also in random distribution.

For such an assembly with positions R_1, R_2 ... R_N the pseudo potential is given by

$$V(R_i,r) = \frac{2\pi\hbar}{m} \Sigma\, b_i\, \delta(r-R_i) \qquad 1.7$$

and the corresponding cross section

$$\frac{d\sigma}{d\Omega} = \left| \int e^{iQ.r} \cdot b_i\, \delta(r-R_i)dr \right|^2 \qquad 1.8$$

Expanding and collecting terms

$$\frac{d\sigma}{d\Omega} = \Sigma\, b_i^2 + \sum_{\substack{i\ j \\ i\neq j}} \sum b_i b_j\, e^{iQ.(R_i-R_j)} \qquad 1.9$$

Assuming isotopic disorder and random distribution of spin orientations this may be written

$$\frac{d\sigma}{d\Omega} = N\Sigma\, \bar{b}^2 - (\bar{b})^2 + (\bar{b})^2 \left| \sum_i e^{iQ.R_i} \right|^2 \qquad 1.10$$

$$= \frac{d\sigma}{d\Omega}\,\text{incoh} + \frac{d\sigma}{d\Omega}\,\text{coh} \qquad 1.11$$

Interference effects of scattered waves from two nuclei give rise to coherent effects which depend only on the average scattering length (which may be positive or negative). The incoherent scattering depends on the mean deviation of the scattering lengths from their average values since

$$N(\overline{|b|^2} - |\bar{b}|^2) = N(b-\bar{b})^2 \qquad 1.12$$

The values of $\bar{b}$ and $\overline{b^2}$ are calculated from the concentration c_i and scattering length for each type of atom present.

$$\bar{b} = \Sigma\, c_i\, b_i \quad \text{and} \quad \overline{b^2} = \Sigma\, c_i\, b_i^2 \qquad 1.13$$

Where there is nuclear spin the cross-section depends on whether neutron and nuclear spin are parallel or anti-parallel. For hydrogen b(triplet) = 1.04×10^{-12} cms, b(singlet) = 4.74×10^{-12} cms. The large incoherent scattering cross-section of 81.6 barns is due mainly, as with vanadium, to the large difference in value of these two scattering lengths.

Incoherent scattering results from random deviations of

the scattering potential, and hence can give rise to no interference effects and is (for a static lattice) isotropic, while coherent scattering from atoms in a lattice comes from the periodic part of the potential.

1.2 Thermal Motion

If the nuclei are not static then the scattered waves have their frequencies Doppler shifted. The scattering potential is now time dependent with $\underline{R}_i$ replaced by the operator $\underline{R}_i(t)$. If the incident wave is $e^{i(kr-\omega_o t)}$, the scattered wave may be determined using the time dependent Schroedinger equation, and the final result for the double differential cross-section is given by

$$\frac{d^2\sigma}{d\Omega dE} = \frac{k}{k_o}\frac{1}{2\pi\hbar}\iint dt e^{-i\omega t}\sum_{ij} b_i^* b_j\, e^{iQ.(r-r'')}$$

$$\delta(r'' - R_i.(0))\delta(r-R_j(t))drdr'' \qquad 1.14$$

If the nuclear coordinates are treated merely as vectors, after integration

$$\frac{d^2\sigma}{d\Omega dE} = \frac{k}{k_o}\cdot\frac{1}{2\pi\hbar}\int dt\, e^{-i\omega t}\sum_{ij} b_i b_j\, e^{\overline{i(Q.R_j(t) - R_i(0))}} \qquad 1.15$$

where the bar signifies a time average value.

Elastic scattering ($\omega=0$) arises from the time average distribution of the nucleus unlike the X-ray cross-section which is in effect the integral over all energy changes (all very much smaller than the incident energy so leading to a term in $\delta(t)$ and a corresponding 'snapshot' distribution).

1.3 Nuclear Bragg Scattering

Having set ω to zero, the time integration is dominated by times which are effectively infinite when compared with the real correlation times [$\lesssim 10^{-11}$ secs] in the equation so

$$\frac{d\sigma}{d\Omega} = \sum_{ij} b_i b_j \, e^{iQ.(R_j(\infty) - R_i(0))} \qquad 1.16$$

In a crystal, atoms occur at periodic positions and the position may be defined by

$$\underline{R} = \underline{l} + \underline{p} + \underline{u} \qquad 1.17$$

where $\underline{l}$ gives the position of the unit cell, $\underline{p}$ is the equilibrium position within the cell, and $\underline{u}$ is the mean displacement from the equilibrium position. For every crystal lattice defined by the vector $\underline{l}$ a reciprocal lattice can be defined with vectors τ such that

$$\exp(i\underline{\tau}.\underline{l}) = 1 \text{ for all } \underline{l} \qquad 1.18$$

Thus if the unit cell is defined in terms of three non coplanar vectors $\underline{a}_1$, $\underline{a}_2$, $\underline{a}_3$

$$\underline{l} = l_1 a_1 + l_2 a_2 + l_3 a_3$$

when l_i are the cell indices

Then

$$\underline{\tau}_1 = \frac{2\pi\, \underline{a}_2 \times \underline{a}_3}{\underline{a}_1 \cdot \underline{a}_2 \times \underline{a}_3} \quad \underline{\tau}_2 = \frac{2\pi\, \underline{a}_3 \times \underline{a}_1}{\underline{a}_2 \cdot \underline{a}_3 \times \underline{a}_1} \quad \underline{\tau}_3 = \frac{2\pi\, \underline{a}_1 \times \underline{a}_2}{\underline{a}_3 \cdot \underline{a}_1 \times \underline{a}_2}$$

($a_1 . a_2 \times a_3$ is volume of unit cell, v_o

and, in general, for integer values of t_i

$$\underline{\tau} = t_1\underline{\tau}_1 + t_2\underline{\tau}_2 + t_3\underline{\tau}_3 \qquad 1.19$$

If a_1, a_2 and a_3 are orthogonal

$$\underline{\tau}_1 = \frac{2\pi}{\underline{a}_1}, \quad \underline{\tau}_2 = \frac{2\pi}{\underline{a}_2}, \quad \underline{\tau}_3 = \frac{2\pi}{\underline{a}_3} \qquad 1.20$$

Evaluating the cross-section first of a rigid ($\underline{u}=0$) lattice with only one atom per unit cell ($\underline{p}=0$) (Bravais lattice)

$$\frac{d\sigma}{d\Omega}_{coh} = |\bar{b}|^2 \left|\sum_i \exp i\underline{Q}.\underline{R}_i\right|^2 \qquad 1.21$$

When $\underline{Q}$ is equal to any multiple of a reciprocal lattice vector τ all the terms in the sum over i add up in phase. As $\underline{Q} \neq \underline{\tau}$ the sum drops to zero. So for a large crystal

$$\frac{d\sigma}{d\Omega coh} = \frac{N.(2\pi)^3}{v_o} \left|\bar{b}\right|^2 \sum_{\tau} \delta(\underline{Q}-\underline{\tau}) \qquad 1.22$$

With more than one atom per unit cell

$$\frac{d\sigma}{d\Omega coh} = \frac{N.(2\pi)^3}{v_o} \sum_{\tau} \delta(\underline{Q}-\underline{\tau}) \left|F\ (\underline{\tau})\right|^2 \qquad 1.23$$

where the molecular structure factor F ($\underline{\tau}$) modulates the intensities of the observed Bragg peaks which occur as $\underline{Q} = \underline{\tau}$.

$$F\ (\tau) = \sum_i b_i \exp(i\underline{\tau}.\underline{p}) \qquad 1.24$$

Similarly

$$\frac{d\sigma}{d\Omega}_{incoh} = \{\overline{b_i^2} - (\bar{b}_i)^2\} \qquad 1.25$$

Scattering from polycrystalline powders leads to neutrons being scattered along Debye Scherrer cones, some crystallites always being in the correct orientation to satisfy the Bragg condition. Diffraction from a set of planes becomes impossible if $2k_o < \tau_{min}$, the corresponding wavelength $\lambda > 2a_{max}$ where a is the plane spacing. This is utilised in the construction of neutron filters, either setting polycrystalline materials to reflect out all neutrons of short wavelength, e.g. beryllium, $\lambda_{min} = 3.96\text{Å}$ or bismuth used to reduce γ rays in neutron beams, but set, as a single crystal, to transmit neutrons.

Thermal motions of the nuclei in crystals reduce both coherent and incoherent cross-sections. This effect is Q dependent and is incorporated in the Debye Waller factor W which will be discussed in section (3.3). The final form of the cross-sections are

$$\frac{d\sigma}{d\Omega}^{el}_{coh} = \left|\sum b_i \exp i\underline{Q}.\underline{p}_i\right|^2 e^{-2W_i(Q)} \delta(\underline{Q}-\underline{\tau}) \qquad 1.26$$

$$\frac{d\sigma}{d\Omega}^{el}_{incoh} = \sum b_i^2 - \bar{b}^2\ e^{-2W_i(Q)} \qquad 1.27$$

Since the sum of the thermal vibrations of each atom is reflected in the cross-section, temperature changes affect the contributions of specific atoms differently and the structure factor is modified in a complex fashion.

1.4 Inelastic Scattering

Elastic scattering involves no changes in the quantum mechanical state of the system. During the scattering process a transition may occur from an initial energy state E_o to another energy state E_1 which will correspond to an inelastic cross-section term.

Eigenstate Formulation

The description of the scattering cross-section in terms of the time dependent operators $\underline{R}_i(0)$, $\underline{R}_j(t)$ may be transformed into an expression in terms of the eigenstates of the scatterer (Zemach and Glauber, 1956) using the relationship between the Heisenberg and Schroedinger representations.

$$\underline{R}_j(t) = e^{iHt/\hbar}\ \underline{R}_j(0)\ e^{-iHt/\hbar} \qquad 1.26$$

Thus equation 1.15 becomes

$$\frac{d^2\sigma}{d\Omega dE} = \frac{k_1}{k_o}\frac{1}{2\pi\hbar}\int dt e^{-i\omega t}\ \Sigma\, b_i b_j\ e^{i\underline{Q}.\underline{R}_i(0)}\ \{e^{iHt/\hbar} e^{i\underline{Q}.\underline{R}(0)}\ e^{-iHt/\hbar}\}$$

$$= \frac{k_1}{k_o}\frac{1}{2\pi\hbar}\int dt e^{-i\omega t}\ \sum_{ij}\sum_{o,1} b_i b_j p_o \langle o|\, e^{i\underline{Q}.\underline{R}_i(0)}\,|1\rangle$$

$$\times\ \langle 1|\, e^{iHt/\hbar}\, e^{i\underline{Q}.\underline{R}_j(0)}\, e^{-iHt/\hbar}\,|o\rangle \qquad 1.27$$

where $|0\rangle$ denotes the initial state, and $|1\rangle$ the final state so the time average must weight $|0\rangle$ with its occupation number p_o at temperature T.

$$p_o = (\exp\frac{\hbar\omega}{kT} - 1)^{-1} \qquad 1.28$$

Since

$$\langle 1| e^{iHt/\hbar} = e^{iE_1} \text{ and } e^{-iHt/\hbar}|1\rangle = |1\rangle e^{-E_1 t/\hbar}$$

$$\frac{d^2\sigma}{d\Omega dE} = \frac{k_1}{k_o}\int_o^\infty dt\, e^{-i(\omega-(E_o-E_1)/\hbar)t}$$

$$\times \sum_{ij}\sum_{if} b_i b_j p_p \langle o| e^{i\underline{Q}\cdot\underline{R}_i(0)}|1\rangle\langle 1| e^{-\underline{Q}\cdot\underline{R}_j(0)}|o\rangle \qquad 1.29$$

The sum must be performed over all possible final states. The time integral is performed directly yielding the requirement of energy conservation in the scattering process (an additional constraint being that the neutron energy may not be negative).

$$\frac{d^2\sigma}{d\Omega dE} = \frac{k_1}{k_o}\,\delta(E_1-E_o-\hbar\omega)\sum_{ij}\sum_{01} b_i b_j p_o \langle o| e^{i\underline{Q}\cdot\underline{R}_i}|1\rangle\langle 1| e^{-i\underline{Q}\cdot\underline{R}_j}|0\rangle \qquad 1.30$$

The corresponding coherent and incoherent cross-sections are

$$\frac{d^2\sigma}{d\Omega dE}^{coh} = \frac{k_1}{k_o}\sum_1\left|\sum_i b_i\langle 0| e^{-iQ\cdot R_i}|1\rangle\right|^2 \delta(E_1-E_o-\hbar\omega) \qquad 1.31$$

$$\frac{d^2\sigma}{d\Omega\, dE}^{incoh} = \frac{k_1}{k_o}\sum_1\sum_i (b^{incoh})^2\left|\langle 0| e^{-iQ\cdot R_i}|1\rangle\right|^2 \delta(E_1-E_o-\hbar\omega) \qquad 1.32$$

and these are the basic equations of slow neutron scattering theory.

1.5 Scattering by vibrating systems

Molecular motions and the motions of atoms in crystalline solids are usually described using the harmonic approximation, and the solutions based on the calculation of normal modes of vibration. The scattering by vibrating nuclei with position vectors

$$\underline{r}_i(t) = \underline{l}_i + \underline{u}_i(t) \qquad 1.33$$

depends on

$$\langle 0|\ \exp i\underline{Q}\cdot\underline{u}_j(t)\ \exp -i\underline{Q}\cdot\underline{u}_i(0)\ |0\rangle \qquad 1.34$$

$$= \exp(i\underline{Q}.(\underline{l}_j - \underline{l}_i) \langle 0 \exp(i\underline{Q}.\underline{u}_j(t) \exp -i\underline{Q}.\underline{u}_i(0) 0\rangle \qquad 1.35$$

Because the nuclei are in thermal equilibrium the initial states occupied are distributed, and the average of this function over these states is required. If χ_{ij} denotes the products of the exponential displacements, then

$$\langle\chi\rangle_T = \langle \exp(i\underline{Q}.\underline{u}_j(t)).\exp(-\underline{Q}.\underline{u}_i(0)\rangle_T \qquad 1.36$$

which may be evaluated for a harmonic oscillator. The normal modes of vibration q_λ with amplitude vector C_λ replace $u_i(t)$

$$\underline{u}_i(t) = \sum_\lambda C_\lambda \, q_\lambda \, (t) \qquad 1.37$$

and the exponential function of $u_i(t)$ may be separated into a product of terms

$$\exp i\underline{Q}.u_i(t) = \pi_\lambda \exp(i\underline{Q}.C_{i\lambda} \, q_\lambda(t)) \qquad 1.38$$

Because normal modes are independent there is equipartition of energy amongst them, and the average of the product of two exponentials may be separated into a product of their mean values

$$\langle\chi_{ij}\rangle_T = \pi_\lambda \, \langle\chi_{ij}^\lambda\rangle_T$$

$$= \pi \langle\exp(i\underline{Q}.C_j^\lambda q \, (t)) \exp(-i\underline{Q}.C_i^\lambda q_\lambda(0)\rangle_T \qquad 1.39$$

The temperature dependent term for the thermal average is $\langle q(t)q(0)\rangle$. The double differential cross-section is thus given by

$$\frac{d^2\sigma}{d\Omega dE} = \frac{k_1}{k_o} \Sigma b_i \, b_j \, \exp(i\underline{Q}.(\underline{l}_i - \underline{l}_j) \pi \langle\chi_{ij}\rangle_T . \, \delta\varepsilon \qquad 1.40$$

where

$$\varepsilon = E - E - \hbar\omega$$

Energy transfers are limited to discrete values $\varepsilon = \Sigma n_\lambda \hbar\omega_\lambda$ where ω_λ are the normal mode frequencies, and n are integers. The thermal average is expanded as a Fourier series and individual components in the product $\langle\chi_{ij}\rangle_T$ contribute functions at energy transfer ε, the sum of these for all modes giving the partial cross-section.

$$\frac{d\sigma_\lambda}{d\Omega dE} = \frac{k_1}{k_o} \Sigma_{ij}\, b_i b_j \exp i(\underline{Q}.(\underline{l}_i - \underline{l}_j))\; W_{ij}\; \delta(n_\lambda t) \qquad 1.41$$

where

$$W_{ij} = \pi \exp -[(\underline{Q}.\underline{c}_i^\lambda)^2 + (\underline{Q}.\underline{c}_j^\lambda)^2] \times \frac{1}{4\omega} \coth\left(\frac{\hbar\omega}{2k_B T}\right)$$

$$\times \exp(\hbar\omega/kBT) \times I_{n_\lambda} \frac{(\underline{Q}.\underline{c}_i^\lambda)(\underline{Q}.\underline{c}_j^\lambda)}{2\omega \sinh(\hbar\omega/2k_B T)} \qquad 1.42$$

where $I_{n_\lambda}(x)$ is a modified Bessel function and may be represented for small arguments by the series $I_n(x) = (\frac{1}{2}x)^{|n|}\,(n!)^{-1}$. The probability of a two step excitation is therefore much lower than a single step transition.

Taking each term in the cross-section, it depends on a structure factor, the Debye Waller factor, the thermal population factor, and a polarisation factor.

In a polycrystalline solid or a molecular liquid or gaseous system the molecules will have a random orientation with respect to the wave vector transfer and it is necessary to average over all molecular orientations to determine the differential cross-section. The equation simplifies when only incoherent scattering is considered being then of the form:

$$\frac{d\sigma}{d\Omega dE} = \frac{k_1}{k_o} (\overline{b^2} - \bar{b}^2) \prod \exp(-2Q.C_\lambda)^2 \cdot \coth\left(\frac{\hbar\omega}{2k_B T}\right) \exp\left(\frac{\hbar\omega}{k_B T}\right)$$

$$\times I_n \left(\frac{(Q.C^\lambda)^2}{2\omega \sinh\left(\frac{\hbar\omega}{k_B T}\right)}\right) \delta(\varepsilon) \qquad 1.43$$

This eigenfunction formulation was developed by Zemach and Glauber (1956).

1.6 Correlation Formulation

The differential cross-section may also be described in terms of a space-time correlation function (Van Hove 1954), G(r,t) being the probability of two particles being correlated,

one at time t = 0 and at r = 0, and the other at $\underline{r} = \underline{r}$ after time t.

$$G(r,t) = \frac{1}{N} \sum_{ij} dr' \; \delta(r+R_i(0)-r') \; \delta(r-R_j(t)) \qquad 1.44$$

hence

$$\frac{d^2\sigma}{d\Omega dE} = \frac{Nb^2}{2\pi\hbar} \frac{k_1}{k_o} \int e^{-i\omega t} \, dt \int dr \; e^{iQ.r} \; G(r,t) \qquad 1.45$$

This is only true in the elastic limit when $R_i(t)$ are merely numerical values of coordinates, rather than non commuting operators. Differentiating between the cases of the same particle at time 0 and t, and two different particles leads to the incoherent cross-section being directly related to the self correlation function G_s, and the coherent cross-section related to the distinct correlation G_d.

$$G(r,t) = G_s(r,t) + G_d(r,t) \qquad 1.46$$

$$\frac{d^2\sigma}{d\Omega dE}^{coh} = \frac{\bar{b}^2}{2\pi} \frac{N}{h} \frac{k_1}{k_o} \int e^{i(\underline{Q}.\underline{r}-\omega t)} \; G(r,t) dr dt \qquad 1.47$$

and

$$\frac{d^2\sigma}{d\Omega dE}^{incoh} = (\overline{b^2}-\bar{b}^2) \frac{N}{h} \frac{k_1}{k_o} \int e^{i(\underline{Q}.\underline{r}-\omega t)} \; G_s(r,t) dr dt \qquad 1.48$$

The values of this formulation lies in the easy visualisation of the cross-section in terms of the time dependent displacements of the system and is often used in preference to the eigenstate formulation in systems when the quantum states are ill defined as in a liquid.

1.7 The Scattering Law

The experimental observable $\frac{d^2\sigma}{d\Omega dE}$ is represented in 1.47 and 1.48 as a product of two factors, one dependent only on the neutron, and the second on the space time correlation of the scatterer.

$$\frac{d^2\sigma}{d\Omega dE} = \frac{Nb^2}{2\pi\hbar} \cdot \frac{k}{k_o} S(Q,\omega) \qquad 1.49$$

where

$$S(Q,\omega) = \int e^{i(\underline{Q}.\underline{r}-\omega t)} G(r,t)drdt \qquad 1.50$$

$S(Q,\omega)$, the term expressing the dynamics of the scatterer only is known as the scattering law. Two general properties are true for this function: it obeys the sum rule

$$\int \omega.d\omega\ S(Q,\omega) = \frac{\hbar Q^2}{2M} \qquad 1.51$$

where M is the mass of the scatterer; and the detailed balance condition relating the probability of energy loss ($h\omega$ positive) and gain cross sections

$$S(-Q,-\omega) = e^{-\hbar\omega/kT}.S(Q,\omega) \qquad 1.52$$

A symmetrical form of this function even in energy is

$$\tilde{S}(Q,\omega) = e^{\hbar\omega/2kT} . S(Q,\omega) \qquad 1.53$$

It is convenient to work with the dimensionless variables

$$\alpha = \frac{\hbar^2 Q^2}{2MkT} ; \quad \beta = \frac{\hbar\omega}{kT} \qquad 1.54$$

$$S(\alpha\beta) = \frac{kT}{\hbar} \tilde{S}(Q,\omega) \qquad 1.55$$

$S(\alpha,\beta)$ is thus a symmetrical form of the scattering law.

$S(Q\omega)$ can be divided into two parts corresponding to non interference and interference scattering

$$S(Q,\omega) = S_s(Q\omega) + \frac{|<b>|^2}{<|b|^2>} S_d(Q\omega) \qquad 1.56$$

corresponding to G_s and G_d correlation functions of van Hove. With more than one type of atom present additional cross-terms for different atoms are required for $S_d(Q\omega)$. The time fourier transform is known as the intermediate scattering function $I(Q,t)$

$$S(Q\omega) = \frac{1}{2\pi}\int I(Q,t)\ \exp i\omega t\ dt \qquad 1.57$$

This corresponds to the spatial part of the transforms 1.47, 1.48.

$$I(Q,t) = \frac{1}{2\pi\hbar}\int dr\ e^{iQ.r}\ G(rt) \qquad 1.58$$

CHAPTER 2

Lattice Vibrations

2. Lattice Vibrations

2.1 Dynamics of Atoms in Crystals

The formal foundation of lattice dynamics in the harmonic approximation was provided by Born and his collaborators, with a treatise on the subject (Born and Huang, 1954). A more recent review comes from Maradudin, Montroll and Weiss (1963), through current work now extends studies of simple systems to include anharmonic interactions and imperfect crystals. Ionic and simple covalent solids are reviewed by Cochran (1971). More complex solids are dealt with in the review by Venkataraman and Sahni (1970).

2.2 Born von Karman Theory

The potential energy ϕ of a crystal may be expressed as a power series of the atomic displacements. If atom p at equilibrium position $\underline{\rho} = \underline{l} + \underline{p}$ is given a small displacement $\underline{u}_x$ in the x direction and p' corresponds to an atom at ρ' the potential is written

$$\phi = \phi_o + \phi_1 + \phi_2 + \cdots \qquad 2.1$$

where

$$\phi_1 = \sum_{p,x} \frac{\partial \phi}{\partial x(p)} \cdot u_x(p)$$

$$\phi_2 = -\tfrac{1}{2} \sum_{p,x} \sum_{p'y} \frac{\partial^2 \phi}{\partial x(p) \partial y(p')} \cdot u_x(p)\, u_y(p')$$

$$= \sum_{px} \sum_{p'y} \phi x_y(pp')\, u_x(p)\, x_y(p')$$

The derivatives are evaluated at the equilibrium position (which ignores zero point energy and assumes zero temperatures).

The equilibrium potential energy is ϕ_o and is constant; the term ϕ_1 is equal to zero since the crystal is initially in equilibrium. ϕ_2 is a force constant of the force on atom p in the x direction when the atom p' is displaced in the y direction.

The nature of these force constants is restricted to be invariant with the space group of the crystal, else equilibrium could not be maintained. Symmetry is often invoked to simplify possible force fields. Curtailing the series at this term implies that the vibrations are harmonic so the crystal has zero coefficient of expansion, the elastic constants are independent of temperature, and other properties which may in favourable systems be investigated using perturbation theory.

When all atoms are displaced equally there is no net force, and the force constant for self interaction is

$$\phi_{xy}(pp') = - \sum_{p'y} \phi_{xy}(pp')\, u_y(p') \qquad 2.2$$

To avoid explicit consideration of the surface of the crystal periodic boundary conditions are introduced. The equation of motion of atom p, mass mp is then

$$mp\, \ddot{u}_x(p) = \frac{\partial \phi_2}{\partial u_x(p)} = - \sum_{p'y} \phi_{xy}(pp')\, u_y(p') \qquad 2.3$$

The solution of these equations of motion involves finding linear combinations of the displacements (normal coordinates) such that the system of equations represented in 2.3 separate into independent equations. Plane displacement waves provide normal coordinates since the crystal possesses translational symmetry. If the time dependence of the displacement is $\exp(-i\omega t)$ the solution may be expressed in terms of the travelling waves

$$u_x(p) = \frac{u_x}{\sqrt{mp}} \exp i(\underline{q}.\underline{\rho} - \omega(\underline{q})t) \qquad 2.4$$

Substituting this into the equation of motion

$$mp\, \omega^2(\underline{q}).U_p = \sum_{p'y} D(pp', \underline{q})\, U_y(p'.\underline{q}) \qquad 2.5$$

where

$$D_{xy}(pp'\ \underline{q}) = \sum_{l'} \phi_{xy}(p,p') \exp i(\underline{q}.(\underline{l}'-\underline{l})) \qquad 2.6$$

The element D_{xy} is an element of the dynamical matrix, and is independent of the actual unit cells in which p and p' atoms are sited, depending only on the difference, so $\underline{l}$ may be set to zero. In matrix notation

$$\omega^2 M U = D U \qquad 2.7$$

where M is a diagonal matrix U(p) the eigenvector column-matrix and D is a square matrix of order 3n x 3n for the unit cell containing n atoms. For non trivial solutions

$$\det (D-M\omega^2) = 0 \qquad 2.8$$

and this determines 3n frequencies $\omega_j(\underline{Q})$; j = 1,.,.,.,3n branches for each value of $\underline{Q}$. The displacement amplitude is given by

$$\underline{U}_x(p\underline{Q}) = \sum_j \underline{U}_{xj}(p\underline{Q}) \qquad 2.9$$

It is convenient to normalise these amplitudes such that

$$\sum_k m_k \left|\hat{U}(p\underline{Q})\right|^2 = m, \qquad 2.10$$

where m is the mass of one unit cell. For a given $\underline{Q}$ $A_j(\underline{Q})$ the normal coordinate for the mode characterises the actual phase and excitation extent of the mode, which is time dependent

$$U_{xj}(p\underline{Q}) = A_j(\underline{Q})\, \hat{U}_{xj}(p\underline{Q}) \qquad 2.11$$

and the displacement resulting from simultaneous excitations of all modes is given by

$$\underline{u}(p) = \sum_{\underline{Q}j} A_j(\underline{Q})\, \hat{U}_j(p\underline{Q}) \exp\{i\underline{Q}.\underline{n} - \omega(\underline{Q})t\} \qquad 2.12$$

Because in the N unit cells there are 3nN atoms, there can only be 3nN normal modes, and for each $\underline{Q}$ there are 3n branches for the dispersion curve so there may only be N distinct values for Q. For a macroscopic crystal N is so large that these values may be regarded as continuous and uniformly distributed in reciprocal space. The frequencies $\omega^2(\underline{Q})$ are periodic in the reciprocal space, but the wave amplitudes defined in 2.4 do not have this simple periodicity. These normal coordinates represent 3nN

independent harmonic oscillators, and their energy is quantised. The energy associated with one mode of vibration is

$$E_j(Q) = mN\left|A_j(Q)\right|^2 \omega_j^2(Q) \qquad 2.13$$

$$= (n_j(Q) + \tfrac{1}{2})\hbar\omega_j(Q)$$

where $n_j(Q)$ is the number of phonons in mode j for a crystal in thermal equilibrium at temperature T,

$$n_j = [\exp(\hbar\omega/kT) - 1]^{-1} \qquad 2.14$$

The number of modes having frequencies between ω and $\omega+d\omega$ is $g(\omega)d\omega$, defining the frequency distribution of the normal modes.

$$\int_0^\infty g(\omega)d\omega = 1 \qquad 2.15$$

The procedure for calculating the eigenfrequencies and eigenvectors involves postulating a form for the potential, then setting up and diagonalising numerically the dynamical matrix (2.7).

2.3 Dynamics of Molecules in Crystals

The problem of setting up a dynamical matrix of dimensions $3n \times 3n$ greatly increases with the number of atoms n in a unit cell. Atoms in molecules are strongly bonded covalently, and the intramolecular vibration modes often have frequencies above $500cm^{-1}$. Intermolecular forces, on which the ultimate mechanical and physical properties of the solid depend, are, typically, weak van der Waals or hydrogen bond intermolecular forces with maximum vibration energies about $150cm^{-1}$. The dynamical matrix is greatly simplified if the coupling through the intermolecular forces of the internal modes is ignored. Treating the molecular modes as in a free molecule, removes the wavevector dependence of these frequencies, and introduces

errors in ignoring the interactions. Few molecules have been treated fully with coupled internal and external interactions (Pawley and Cyvin (1969)).

If only the lattice modes are considered assuming all other bonds to be rigid (Cochran and Pawley, 1964) the procedure of the previous section may be followed with p now identifying a molecule rather than an atom, and there are n molecules per unit cell. The displacement of a molecule involves both translational and librational components

$$\underline{u}(p) = \underline{U}(p,\underline{Q}) \exp(i\underline{Q}\underline{\rho}_p - \omega(\underline{Q})t) \qquad 2.16$$

$$\underline{\theta}(p) = \underline{\theta}(p,\underline{Q}) \exp(i\underline{Q}\underline{\rho}_p - \omega(\underline{Q})t) \qquad 2.17$$

If the index a identifies an atom, and the normalised wave amplitude A_j is introduced, the displacement of an atom by one mode j will be

$$\underline{u}(pa) = A_j(Q) [\underline{\hat{U}}_j(p\underline{Q}) + \underline{\theta}_j(p\underline{Q}) \wedge \underline{a}] \exp i(\underline{Q}\rho - \omega(\underline{Q})t) \qquad 2.18$$

where $\underline{a}$ is the position of an atom relative to the centre of mass of the molecule at $\underline{\rho}$. In an analogous situation to equation 2.5 the dynamical matrix elements are obtained from 2.16, 2.17

$$mp\,\omega^2(\underline{Q})U_x(p) = \sum_{p'y} \phi_{xy}(pp')U_y(p') \exp i\underline{Q}.\underline{\rho} + \sum_{\beta} \phi_{x\beta}^{(pp')}\Theta_{\beta}(p') \exp i\underline{Q}.\rho \qquad 2.19$$

$$Ip\,\omega^2(\underline{Q})\Theta_{\alpha}(p) = \sum_{y} \phi_{\alpha y}^{(pp')}U_y(p') \cdot \exp\underline{Q}.\underline{\rho} + \sum_{\beta} \phi_{\alpha\beta}^{(pp')}\Theta_{\beta}(p') \exp i\underline{Q}.\underline{\rho} \qquad 2.20$$

In matrix notation

$$(\eta\mathbb{z})\,\omega^2\,(\mathbb{U}\theta) = \mathbb{D}(\mathbb{U}\theta) \qquad 2.21$$

where $(\mathbb{U}\theta)$ is a 6n vector of displacements and rotation vectors, the $\eta\mathbb{z}$ matrix is a diagonal matrix of the atomic masses and moments of inertia, and $\mathbb{D}$ the dynamical matrix. The equations are solved as an eigenvalue problem in the form

$$\omega^2 \left[(m_z)^{\frac{1}{2}} (U\theta)\right] = \left[(m_z)^{-\frac{1}{2}} D (m_z)^{-\frac{1}{2}}\right] \left[(m_z)^{\frac{1}{2}} (U\theta)\right] \qquad 2.22$$

The summations extend over the p' molecules in the other cells. Symmetry transformation T are used to simplify the interaction matrix Φ, with $\tilde{T}$ the transpose

$$\phi(pp'') = T\Phi(pp')\tilde{T} \qquad 2.23$$

For the case where

$$\phi(pp') = T\Phi(pp')\tilde{T} \qquad 2.24$$

bringing both molecules to their initial positions there is a restriction on the number of independent elements of $\Phi(pp')$. The dynamical matrix is Hermitian and in general will lead to eigenvectors with both imaginary components and cross terms of libration and displacements. Linear transformations altering the relative phases of the components may be used to reduce the imaginary components and allow some physical interpretation to be placed on the real part of the eigenvector. The presence of a centre of symmetry in a unit cell reduces the problem to solving a real 6n x 6n matrix.

In such an example Pawley (1967) proposed a 6-exp potential to simulate the Van der Waals interaction between atoms for naphthalene, and then summed the non-bonded atom interactions in adjacent cells to construct the dynamical matrix which could then be solved to determine the eigenvalues and eigenvectors of the dispersion curves.

2.4 Symmetry of Lattice Vibration

It is the invariance of the potential energy of the crystal to symmetry transformations and the interchange of equivalent particles which limits the number of interparticle forces, so as in free molecules the normal modes reflect the structure, and by symmetry arguments alone the displacement polarisations may be determined. Even the most crude model by simulating the structure

correctly may be used to determine the eigenvectors for any direction, though equivalent transformations are possible at arbitrary points in the Brillouin zone. The pure rotational elements in a space group G comprise a point group G_o. When this operates on either the wavevector or the eigenvector the result is invariant. By using character tables with suitable basis functions the irreducible representations may be obtained. Kovalev (1965) tabulates these functions for all symmetry points and lines in the 230 space groups. Using these tables and projection-operator algebra it is possible to obtain the eigenvectors of the normal modes (Maradudin and Vosko, 1968). This technique has been used with solids as complex as Gallium (Waeber, 1970) to calculate dynamical structure factors for inelastic neutron scattering experiments. Though the frequencies $\omega(\underline{q})$ and the magnitude of the eigenvectors are invariant with the translational symmetry, the extent of excitation of the modes is zone dependent in a complex fashion which is in principle a function of the full lattice symmetry. The formulation in terms of rigid molecule motions has been solved for a few compounds of high symmetry e.g. hexamine, adamantane, NH_4Cl (Chen and Dvorak, 1968). As is the case with determining symmetry coordinates in free molecules, the most useful function is to classify the normal modes, each problem being quite individual. Recently numerical techniques have been developed to deal with up to four atoms per unit cell, (Worlton and Warren, 1971). An indication of the advantageous use of symmetry is the reduction of the general Hermitian dynamical matrix to a real matrix when there is a centre of symmetry in the unit cell since polar and axial vectors transform under different irreducible representations, and there is no cross coupling of librations and translations.

2.5 Properties of Phonons

The phonons, represented by the dispersion relation $\omega(\underline{q})$ reflect intimately the force constants between atoms in a system. There are general properties of phonons in all crystals.

1. In all crystals as $\underline{q} \rightarrow 0$ there are three branches in which $\omega(\underline{q}) \rightarrow 0$. These are the acoustic modes, corresponding in the limit of zero $\underline{q}$ to sound waves with all the atoms vibrating in phase. The slope of $\omega(\underline{q})$ versus $\underline{q}$, the velocity of sound in the material, is related to the elastic constants as $q \rightarrow 0$, both of which depend on the direction in the crystal, and the polarisation of the wave.

2. The remaining $3n-3$ branches are known as optic modes since the net antiphase correlation at $\underline{q} = 0$ allows interaction with electromagnetic radiation. In molecular crystals intramolecular modes may not couple with other molecules, the corresponding phonon branch being independent of $\underline{q}$ with an energy similar to the free molecule.

3. The phonons are bosons and the occupation of eigenstates in thermal equilibrium is related to the energy $\hbar\omega$ and temperature by

$$p = (\exp \hbar\omega/kT - 1)^{-1}$$

In real crystals anharmonicity gives rise to finite phonon lifetimes hence an energy broadening.

CHAPTER 3

Neutron Scattering by Phonons

3. Neutron Scattering by Phonons

To determine the cross-section it is necessary to calculate the matrix element in 1.30.

$$\langle 1 | \; e^{-\underline{\kappa}\cdot\underline{R}_p} \; | 0 \rangle \;=\; \left[e^{-\underline{Q}\cdot\underline{\rho}_p} \cdot e^{-i\underline{Q}\cdot\underline{u}_p} \right]_{n_o}^{n_1} \qquad 3.1$$

where n_1, n_o are the occupation numbers of the states. The only dynamical variable is $\underline{u}_p$ which is treated as from 1.26 as an operator. The solution for these harmonic oscillators is now dependent on the phonon wavevector $\underline{Q}$

$$\frac{d^2\sigma}{d\Omega dE} \;=\; \frac{k_1}{k_o} \sum_{pp'} b_p b_{p'} \int \{ \exp(-i\omega t) \exp i\underline{Q}\cdot(\underline{\rho}_p - \underline{\rho}_{p'}) \} \; W_{pp'} dt \qquad 3.2$$

$$W_{pp'} \;=\; \pi_j \exp - \left[\underline{Q}\cdot\underline{U}_j^2(p\underline{Q}) + \underline{Q}\cdot\underline{U}_j^2(p'\underline{Q}) \right] \times \frac{1}{4\omega} \coth \frac{\hbar\omega}{2kT} \times$$

$$\times \exp \left(\frac{\hbar\omega_j}{kT} \right) \times I_n \left(\frac{\underline{Q}\cdot\underline{U}_j(p\underline{Q}) \cdot \underline{Q}\cdot\underline{U}_j(p'\underline{Q})}{2\omega_j \sinh(\hbar\omega/2kT)} \right) \qquad 3.3$$

I_n is a modified Bessel function, which may for the small arguments involved be:

$$I_n(x) \sim (\tfrac{1}{2}x)^n \; (|n|!)^{-1} \qquad 3.4$$

3.1 Elastic Scattering

Elastic scattering when n = 0 is given by

$$\frac{d\sigma}{d\Omega}^{coh} \;=\; \left| \Sigma \, b_p \exp i\underline{Q}\cdot\underline{p} \right|^2 \cdot \exp(-2W_p(\underline{Q}))\delta(\underline{Q}-\underline{\tau}) \qquad 3.5$$

$$\frac{d\sigma}{d\Omega}^{incoh} \;=\; N \sum_p \overline{b_p^2} - \bar{b}_p^2 \exp(-2W_p(\underline{\omega})) \qquad 3.6$$

Where W is known as the Debye-Waller factor, which is a function of the number of normal mode distribution $G(\omega)$

$$G(\omega) \;=\; \frac{1}{3N} \Sigma_{j\underline{Q}} \, \delta(\omega - \omega(\underline{Q})) \qquad 3.7$$

$$W(\underline{Q}) = W_{pp'} = 3N \int G(\omega)d\omega \frac{\hbar}{4NM\omega} \coth \frac{\hbar\omega}{kT} \{\underline{Q}\cdot U(p)\}_{av}$$

3.8

$W(\underline{Q})$ is dependent on the thermal population factor and is insensitive to detail in $G(\omega)$. Atoms in different dynamical situation have different $W(\underline{Q})$ factors leading to different contributions with changing temperature.

3.2 The One Phonon Approximation

One phonon creation or annihilation requires only knowledge of the ground and first excited states, for creation:

$$\frac{d^2\sigma_j^{coh}}{d\Omega dE}_{inel} = \frac{k_1}{k_o} \sum_\tau \left| \sum_p b_p \exp(-W_p(Q)) \times \right.$$

$$\left. \times \exp(i\underline{Q}\cdot\underline{\rho}) \cdot \underline{Q}\cdot\underline{U}_j(p\underline{Q}) \right|^2 \times \frac{1}{z(1-\exp(z))} \cdot \delta(E-\omega_j(\underline{Q})) \ \delta(\underline{Q}-\underline{q}-\underline{\tau})$$

3.9

where the $z = \hbar\omega/kT$ and E and Q are the energy and momentum transfers.

$$E = \hbar^2(k_1^2 - k_o^2)/2m \quad |\underline{Q}| = \underline{k}_1 - \underline{k}_o$$

Study of the discrete cross-section in $(\underline{Q},\omega)$ space by varying E and Q yields the dispersion relation $\omega(\underline{q})$ as a function of $\underline{q}$. Putting $p = p'$

$$\frac{d^2\sigma_j}{d\Omega dE}^{incoh}_{inel} = \frac{k_1}{k_o} \exp(-2W(\underline{Q})) \sum_p \left|\underline{Q}\cdot\underline{U}_j(p\underline{Q})\right|^2 \cdot \frac{1}{z(1-\exp(z))}$$

$$\delta(E-\omega_j(\underline{Q}))$$

3.10

There are no momentum conservation requirements, only in energy. The sum over all modes is

$$\frac{d^2\sigma}{d\Omega dE}^{incoh}_{inel} = \frac{k_1}{k_o} \exp(-2W(\underline{Q})) \left\{\left|\underline{Q}\cdot\underline{U}\right|^2\right\}_{av} \frac{G(\omega)}{\hbar\omega} \frac{\delta(E-\hbar\omega)}{(1-\exp(z))}$$

3.11

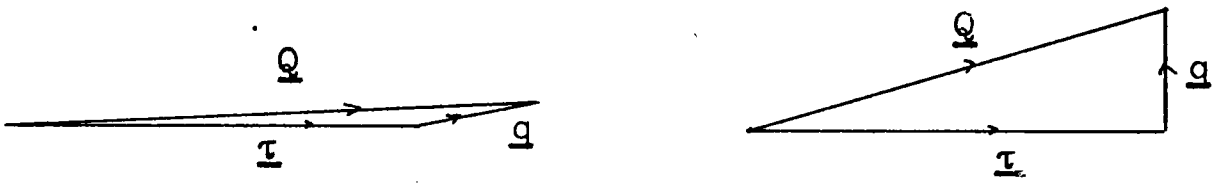
Incoherent inelastic scattering has therefore a continuous energy distribution which is proportional to $G(\omega)$. $G(\omega)$ may be obtained from measurements of the scattering intensity as a function of $\underline{Q}$.

CHAPTER 4

Experimental Investigation of Normal Modes of Vibration with Neutrons

4. Experimental Investigation of Normal Modes of Vibration with Neutrons

By setting an incident monoenergetic collimated beam of neutrons, $\underline{k}_o$, on a single crystal and detecting with energy and direction analysis the scattered neutrons $\underline{k}_1$ the energy and momentum transfer in the scattering process is determined and hence the $\omega(\underline{Q})$ versus $\underline{Q}$ dispersion relationship. By suitable orientation of wavevector $\underline{Q}$ with respect to the crystal the number of modes capable of fulfilling the conservation conditions for coherent scattering may be reduced. Along directions of some symmetries longitudinally and transversely polarised phonons may be distinguished by setting $\underline{Q}$ as indicated below.



(a) longitudinal (b) transverse

In general directions the contributions of the modes to the scattering are not so easily distinguished, the polarisation vectors are complex and the lattice waves elliptically polarised, severely limiting the complexity of crystal which can be studied.

The criteria for a suitable experiment are: a large crystal (>2 cm^3) (since phonon cross-sections are small) of perfect mosaic (there is no extinction in phonon scattering), with a simple highly symmetric structure and few atoms per unit cell, with maximum phonon energies of 300 cm^{-1}. Incoherent inelastic experiments require the same incident beam but after scattering from the sample (usually polycrystalline) the detectors may be placed in an extended array on a cone about the axis of k_o

since scattering is only $|\underline{Q}|$ dependent.

There are three basic methods of setting k_o and k_1 and may be used in combination.

(a) Bragg scattering from a single crystal.

(b) Measuring the neutron velocity by timing the neutron traversing a known distance.

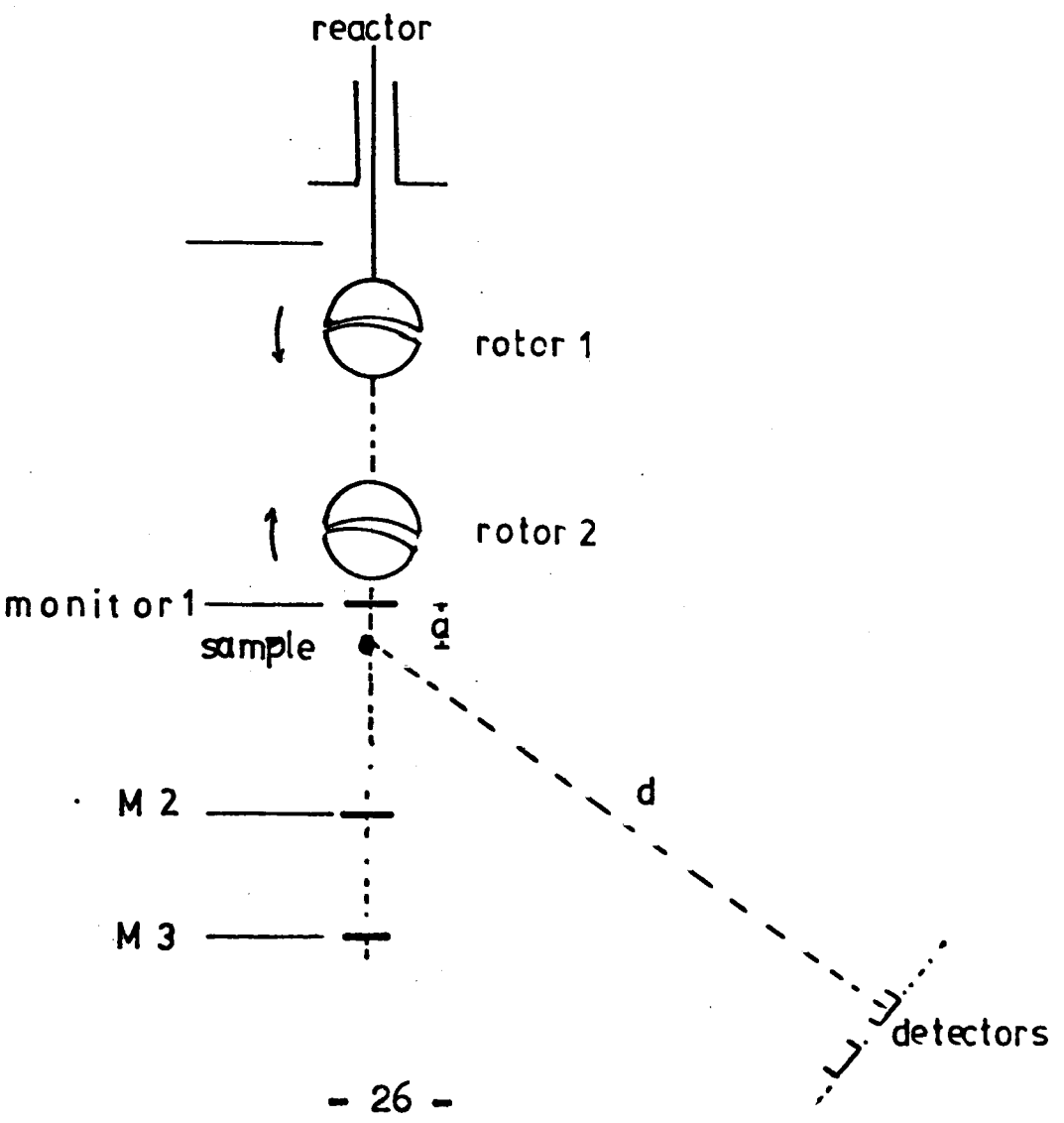
(c) Use of a polycrystalline filter which Bragg scatters all neutrons with wavelength shorter than the cut-off (Section 1.3), and acting as a low-energy-neutron pass-filter.

Further discussion of spectrometers for incoherent scattering studies will be in sec. 6.3.

There are two types of spectrometer used for coherent studies; the pulsed monochromator time-of-flight spectrometer, and the crystal monochromator and analyser triple-axis spectrometer.

4.1 The Time of Flight Spectrometer

This is shown schematically below:



A mechanical velocity selector of two discs of highly neutron-absorbing material with curved slots spin in a vacuum tank at a constant high speed with a specific phase relationship between the slots so only a limited velocity range is transmitted. The mean resultant velocity τ_o is measured by timing the neutron pulse with low sensitivity monitors at fixed distances M1, M2, M3. The time of arrival of the scattered neutron at the detector at an angle θ distance d metres is used to determine the neutron velocity change, hence the energy and momentum transfers involved. The time channel t_o when the neutrons are at the sample position is,

$$t_o = t_{M1} + \frac{\tau_o \, a}{\Delta t}$$

for channel width of Δt secs and t_{M1} is the time channel of the M1 peak. If t_{el} is the channel in which the peak of the elastically scattered neutrons are detected at d, the reciprocal velocity τ' is given by

$$\tau' = \tau_o \frac{(t'-t_o)}{(t_{el}-t_o)}$$ for inelastically

scattered neutrons arriving at time t'. A magnetic pick-up on each rotor is used to control the speed and phasing and to reset a crystal clock once each revolution, the timing reference. Counts are encoded with the time of detection and counter angle and accumulated over a period of 20 to 30 hours.

Samples are mounted on arcs which also rotate in the scattering plane enabling crystals to be set up with a Bragg reflection into one of the detectors, and then offset predetermined amounts for the experimental run.

4.2 The PLUTO Twin Rotor Spectrometer

This instrument is on 7H13 hole on Pluto reactor at Harwell

(Dyer and Low 1961). The seven inch diameter hole is tangential to the reactor, the neutrons being scattered down this hole by a light water source block. Though the thermal neutron flux is only 70% of that from a radial hole the γ-radiation is a factor of 10 less. Cooled crystals of bismuth are used to reduce the γ-ray content still further, the single crystals being set to transmit neutrons.

On the Pluto Spectrometer (which will be referred to as 7H), two 10" diameter rotors with single diverging slots are used, which are spun in opposite directions. The second rotor is used to pick out a narrow band of velocities from the spectrum transmitted by the first. Changing the rotor phasing makes possible small changes of this wavelength of the emergent beam without changing the period of rotation. The time and velocity spread of the neutron burst leaving the second rotor is small, but since there is a velocity distribution, the pulse will broaden as it passes through M1 to Monitor 2 and monitor 3. To minimise the total time spread at the sample it is placed as near as possible to Monitor 1.

The detectors are either ^{6}Li neutron scintillators mounted on 11 stage photomultipliers (30% efficient) or ^{3}He filled proportional gas counters (~90% efficient) there being 30 in all at 1.8 m from the sample. To define the scattered neutron velocity well in space these counters in the horizontal plane have diameters normal to the beam of two inches, and are spaced at 2^{o} intervals. The counter box may be moved on air pads so the maximum angle of scatter is 100^{o}, the minimum angle can place the first counter in the bank in the main beam.

The mean velocity passed through a rotor depends on its curvature and angular velocity (N_s/T_s, neutron speed/tip speed

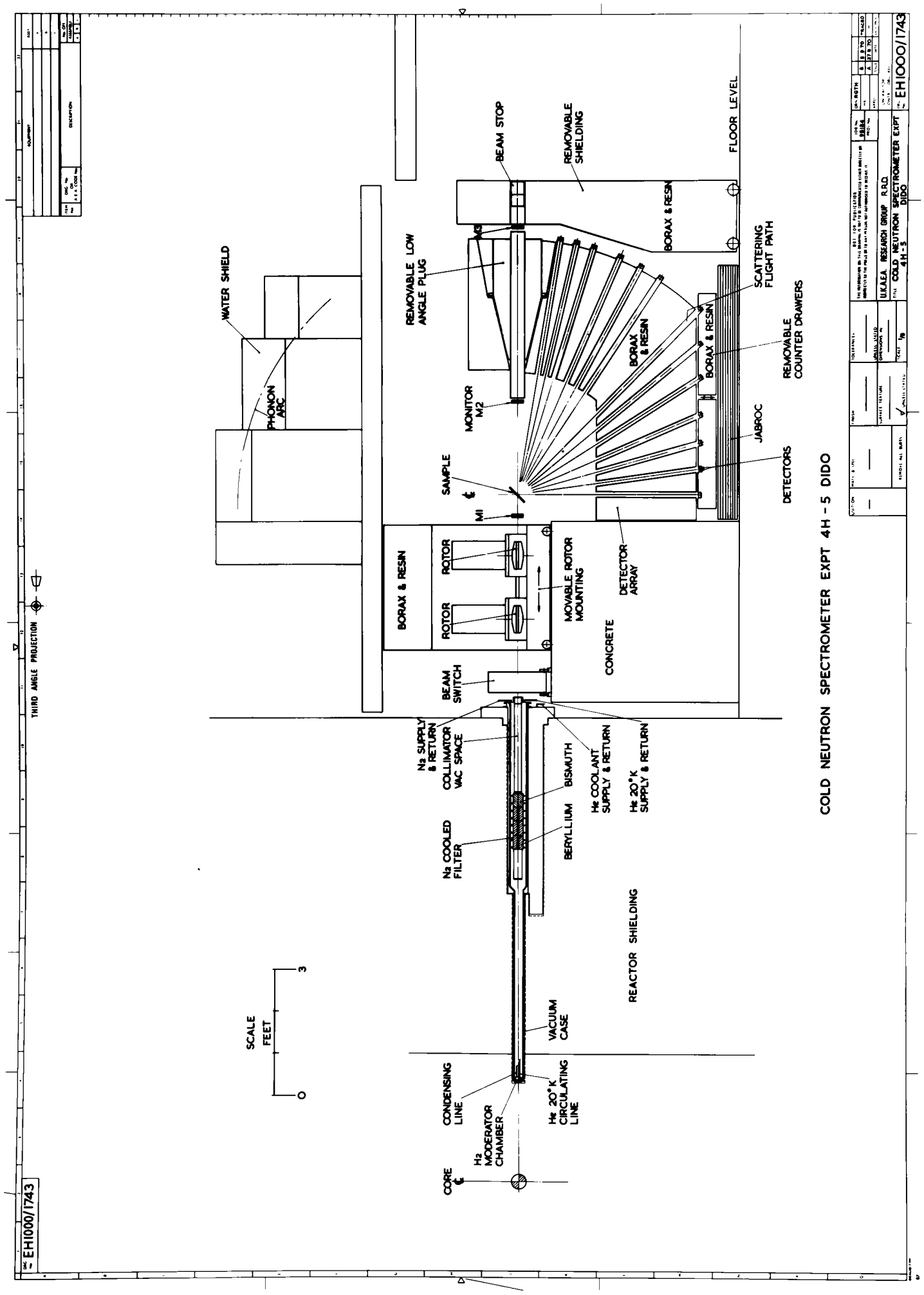

WATER SHIELD
PHONON ARC
REMOVABLE LOW ANGLE PLUG
BEAM STOP
REMOVABLE SHIELDING
FLOOR LEVEL
BORAX & RESIN
SCATTERING FLIGHT PATH
MONITOR M2
SAMPLE
M1
JABROC
DETECTORS
REMOVABLE COUNTER DRAWERS
DETECTOR ARRAY
MOVABLE ROTOR MOUNTING
ROTOR
CONCRETE
BEAM SWITCH
N2 SUPPLY & RETURN
COLLIMATOR VAC SPACE
BISMUTH
He COOLANT SUPPLY & RETURN
He 20°K SUPPLY & RETURN
N2 COOLED FILTER
BERYLLIUM
REACTOR SHIELDING
SCALE FEET
VACUUM CASE
CONDENSING LINE
He 20°K CIRCULATING LINE
H2 MODERATOR CHAMBER
CORE
COLD NEUTRON SPECTROMETER EXPT 4H-5 DIDO
U.K.A.E.A. RESEARCH GROUP R.R.D.
COLD NEUTRON SPECTROMETER EXPT 4H-5 DIDO
EH1000/1743

fig 4.1

is a constant dependent on slot): with different pairs of rotors the incident wavelength obtainable is between 1.8 and 4 Å, though the flux reflects the thermal distribution of the reactor at 40°C, being very low at the longer wavelengths.

With such a large angle covered by the counters, the region of $(Q\omega)$ space scanned in each experiment is very large.

The rotors have slots passing a final beam of 1 x 2 cm, which, together with the excellent shielding makes it useful for small crystal samples, which are usually studied for the larger magnetic rather than phonon-cross-sections.

4.3 The DIDO Cold Neutron Spectrometer

This machine has been described by Harris et. al., 1961, and Peckham 1965, figure 4.1 and will be referred to as '4H5'. To increase the number of long wavelength neutrons there is a chamber in the 4" diameter radial beam hole which is cooled by helium gas and hydrogen vapour condensed within. By scattering, neutrons thermalise with the hydrogen and emerge with an energy distribution peaked at 20°K. The beam then passes through a cooled bismuth filter (to reduce the γ-ray content) then a block of polycrystalline beryllium which scatters out neutrons with a wavelength less than 3.96 Å.

Either one or two 8" diameter multislotted rotors are used to velocity select the pulse and beam. The cross-section of the transmitted beam is thus large (2" x 1" vertically) without loss of resolution. The wavelength is changed by varying the rotor period since the rotors only pass a narrow velocity band, unlike 7H with the larger single slot widths.

Scattered neutrons are detected in the 'Phonon arc' of 24 scintillators mounted in a vertical scattering plane between 36° and 91°. With a flight path of 2.26 m. longer incident

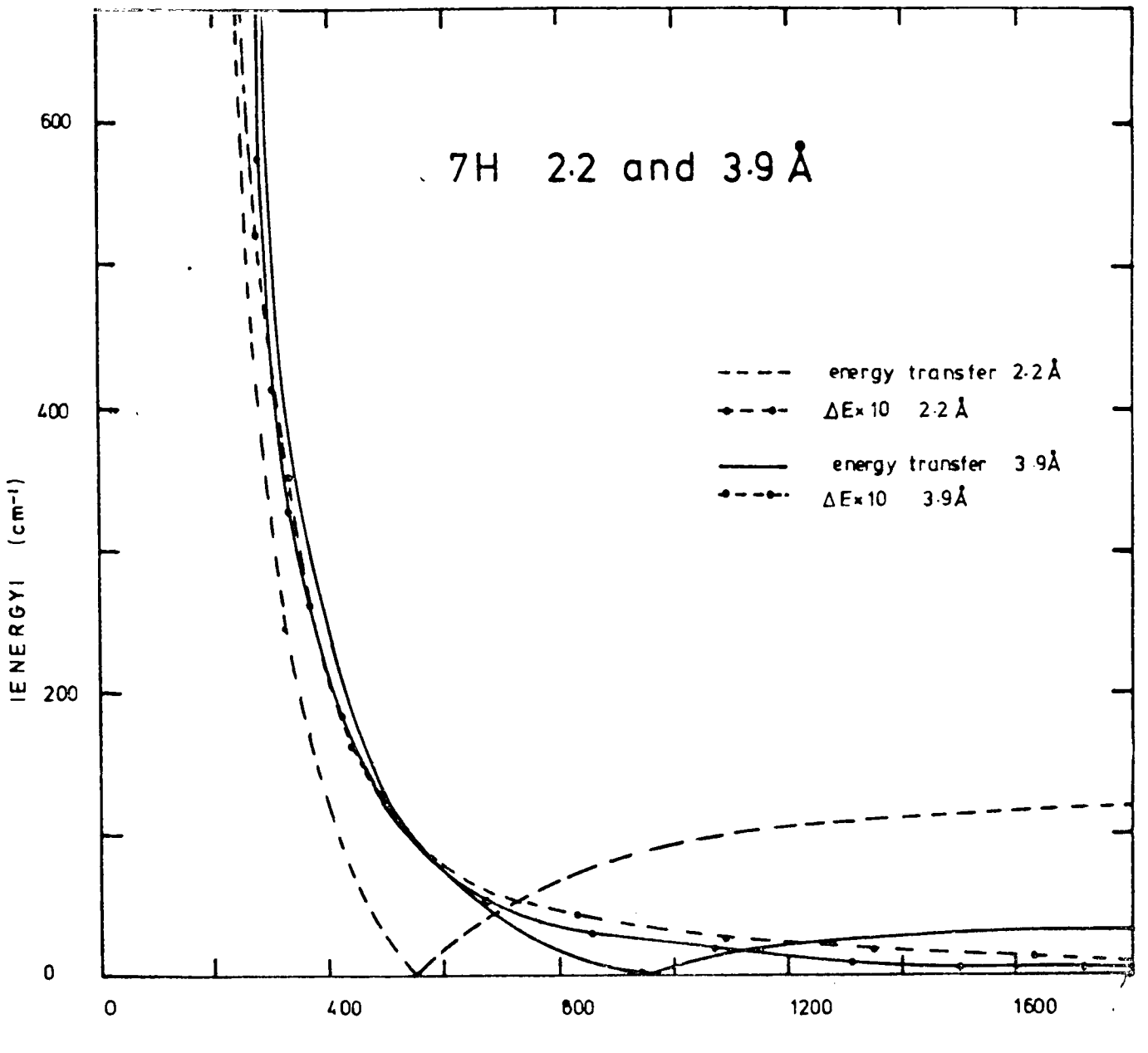
wavelengths than 4.1 Å (obtained with a rotor period of 2118 secs) introduce problems of ambiguity when relating the rotor pulses to the arrival time of the scattered neutron ('frame-overlap').

4.4 Comparison of 4H5 and 7H

Table 4.1 compares the performance of 4H5 and 7H from the aspects of efficiency. To compare their utility in a molecular crystal phonon experiment it is important to compare the resolution of each in $(\underline{Q},\omega)$ space; figures 4.2 and 4.3 the energy and momentum resolution of the two spectrometers were calculated using Royston's method (1962), using the monitor peak widths to assess the wavelength spread.

Each point in the $(\underline{Q},\omega)$ space accessed by the experiment is represented by an ellipsoid $(\Delta Q_x, \Delta Q_y, \omega)$. Specific calculation for each point is difficult and the figures indicating $|\Delta \underline{Q}|$ and ΔE indicate one standard deviation from the nominal $(|\underline{Q}|,\omega)$. Since for a given rotor combination $\Delta E/E_o$ and $\Delta\lambda/\lambda_o$ are approximately constant the absolute incident resolution is improved by going to longer wavelengths. In molecular systems where the real lattices are large this is of considerable importance since ΔQ must be less than 0.2τ to define the terminal point of $\underline{Q}$ in the Brillouin zone. Most simple solids have much smaller real lattices.

Another way of considering the problem that arises with poor resolution is considering the tip of the resolution ellipsoid cutting the scattering surface or skirting a reciprocal lattice point. Very strong scattering is observed which is not represented by the mean $(\underline{Q},\omega)$ of the neutron group, much of the indeterminancy in $\underline{k}_1-\underline{k}_o$ lying in the wavelength spread and finite burst time of the incident beam. In simple systems the number of branches is small and the dispersion curves well characterised


ENERGY RESOLUTIONS
7H 2.2 and 3.9 Å
energy transfer 2.2 Å
ΔE×10 2.2 Å
energy transfer 3.9 Å
ΔE×10 3.9 Å
IENERGYI (cm⁻¹)
600
400
200
0
0
400
800
1200
1600

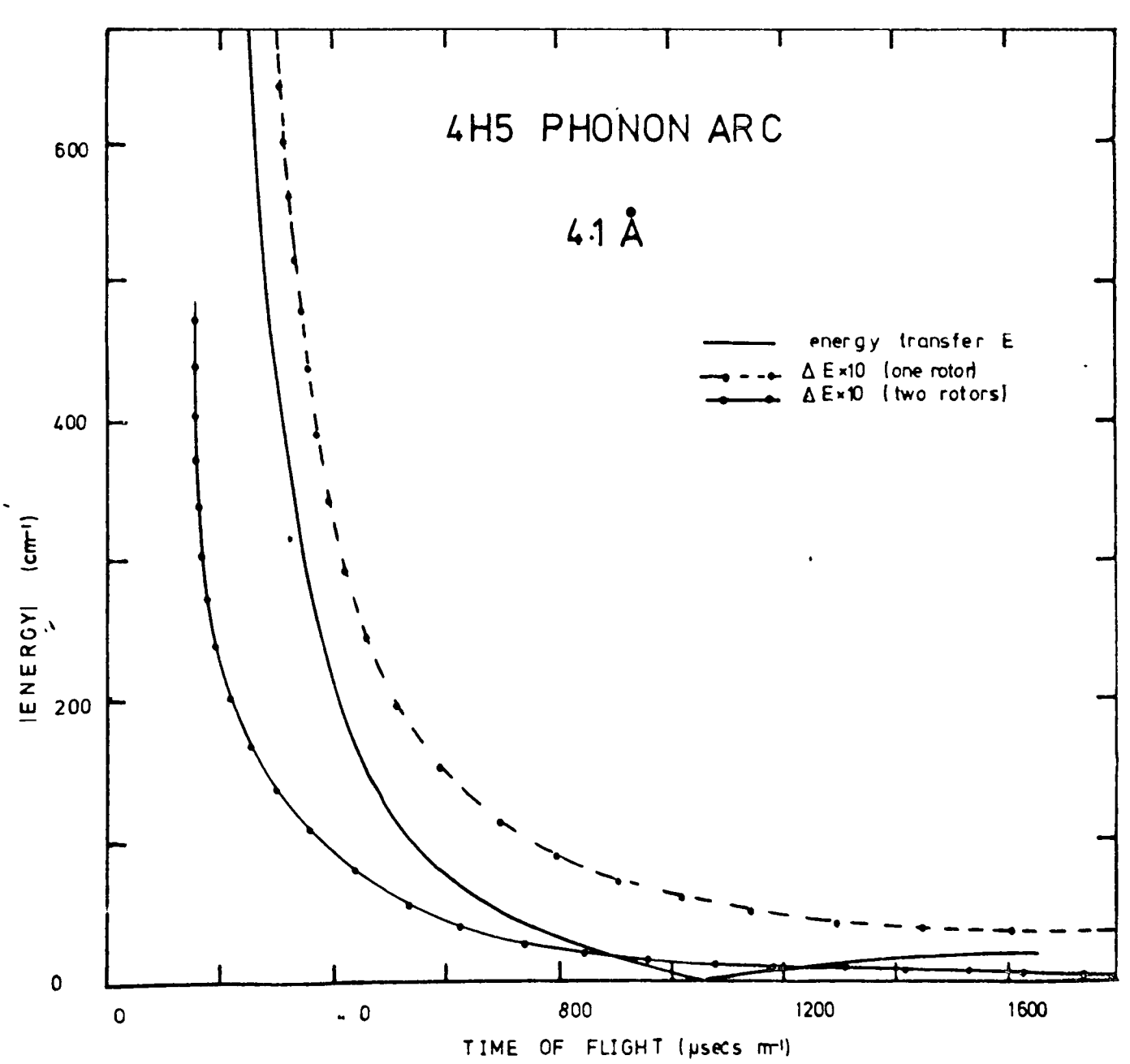
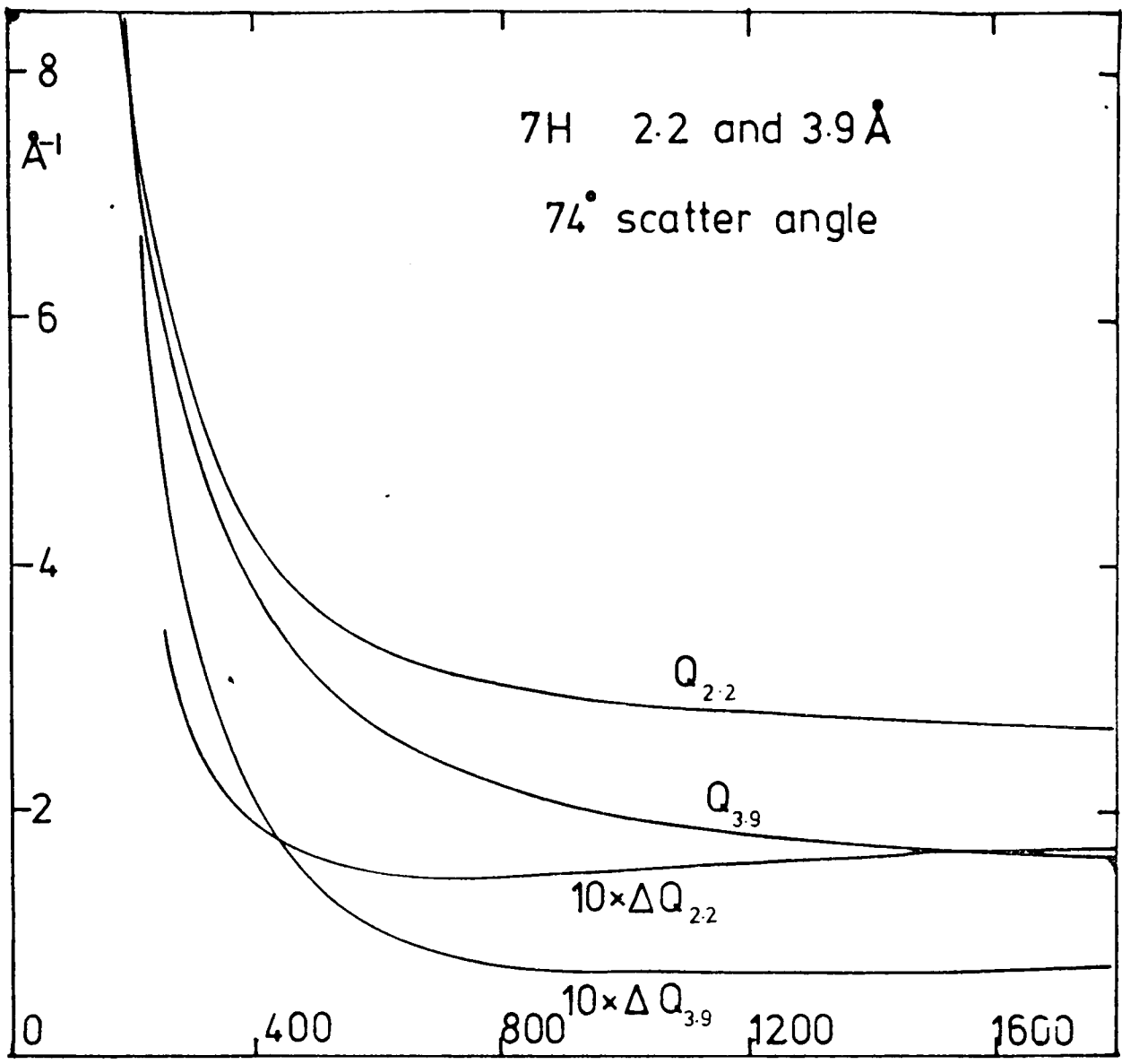

4H5 PHONON ARC
4.1 Å
energy transfer E
Δ E×10 (one rotor)
Δ E×10 (two rotors)
IENERGYI (cm⁻¹)
600
400
200
0
0
0
800
1200
1600
TIME OF FLIGHT (μsecs m⁻¹)

Fig. 4.2

MOMENTUM RESOLUTIONS



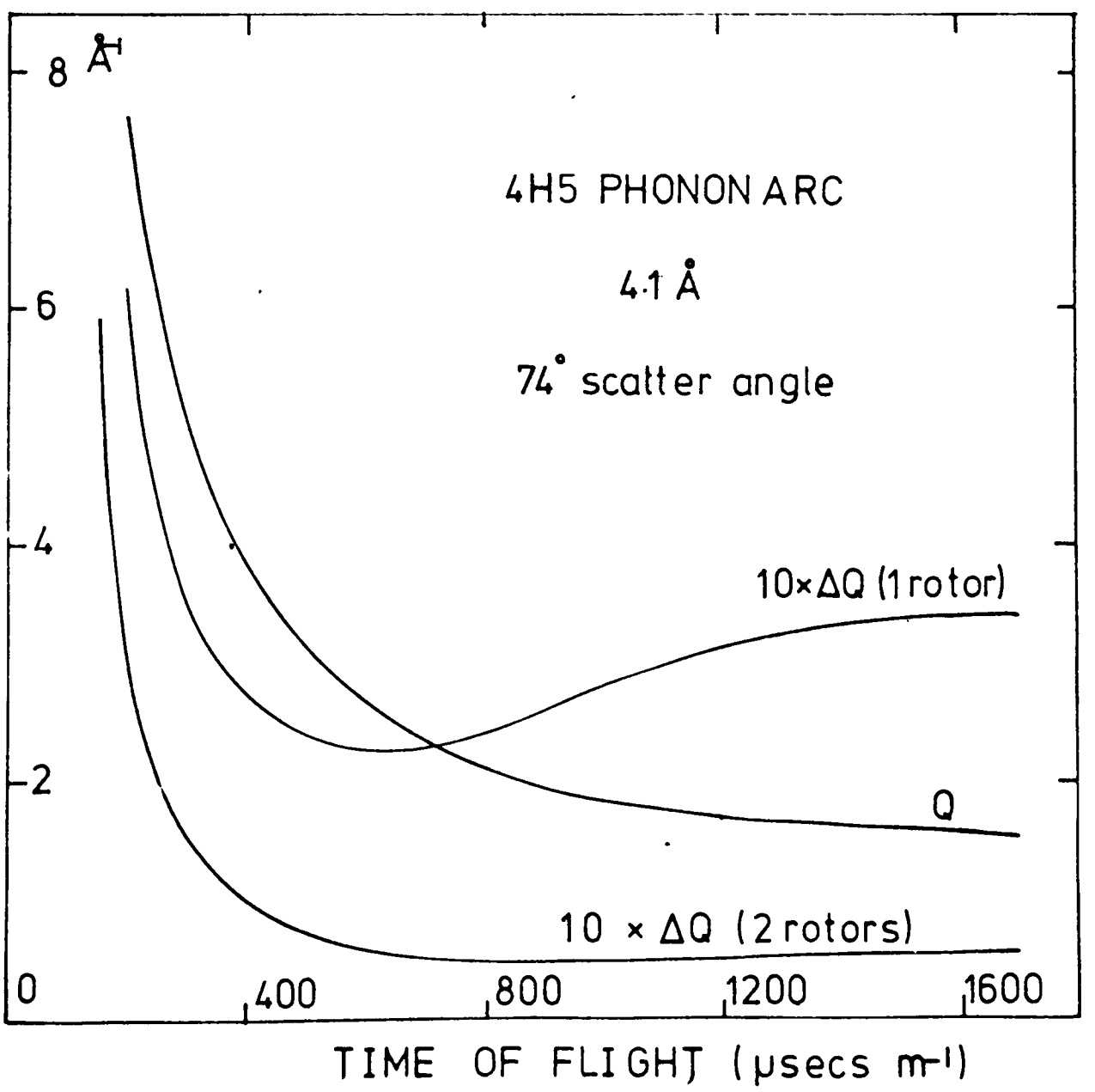


Fig. 4·3

by other physical properties, eliminating these problems.

The area of reciprocal space covered by the two incident wavelengths, 2.2 Å and 4 Å may be compared in fig. 4.4. Though the $(\underline{Q}.\underline{U}(p^{\circ}))(\underline{Q}.\underline{U}(p'^{\circ}))$ term (eq. 3.9) enables much larger cross-sections to be measured at high $\underline{Q}$ values available at 2 Å incident wavelength it is at the expense of resolution. For this reason the analysis was limited principally to neutron energy loss. Using cold neutrons only neutron energy gain is usually observed except for very low energy phonons. A very similar region of $(Q\omega)$ space is available to the two instruments, and experiments at the longer wavelengths are preferable.

Because the phonon arc is a secondary facility of 4H5 full advantage of the collimation resulting from the multi-slotted rotors cannot be taken in the vertical plane: use of cryostats and furnaces on 7H is simpler with the horizontal scattering plane.

The spatial resolution on 4H5 is much better than that of the incident beam. Reducing the flight path would increase the counting rate without effect on resolution. The scintillators and photomultipliers used on 4H5 have an efficiency less than 20% and show signs of progressive deterioration. The actual flux is approximately 1.43×10^{4} n cm^{-2} sec^{-1} for the two 6 slot rotor combination.

With more recent better designed shielding the backgrounds on 7H are very low, and even at 4 Å the neutrons cm^{-2} of beam actually detected is comparable though resolution is poor with these rotors. The gain in flux obtained when DIDO reactor was upgraded from 17 to 22 MW is of limited use with the higher background levels also present now. Experiments were performed without hydrogen but with cooled filters after the cold source developed a leak and had to be replaced.

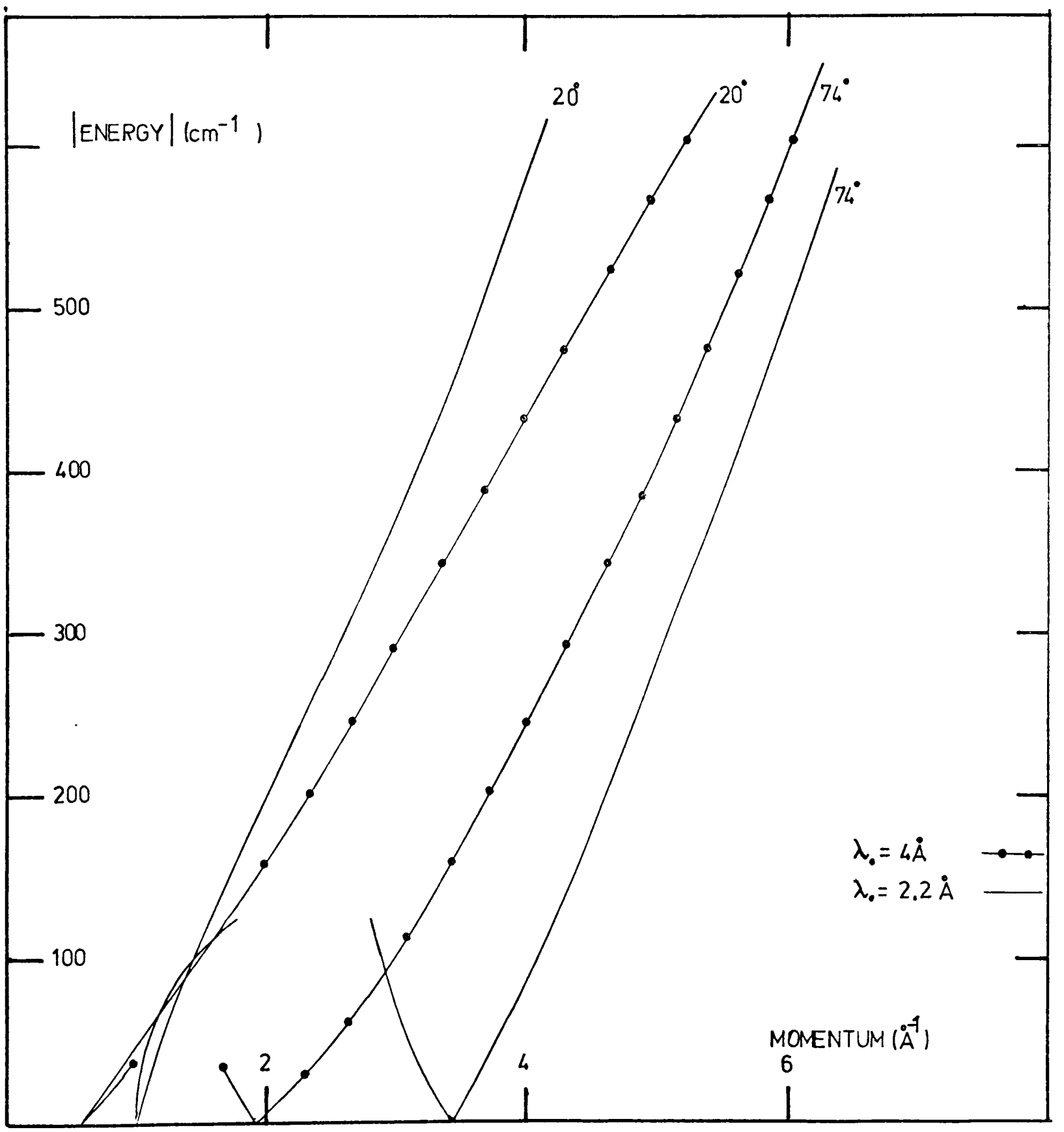

TRACKS IN (Q,ω) SPACE ACCESSED BY COUNTERS
|ENERGY| (cm⁻¹)
500
400
300
200
100
20°
20°
74°
74°
λ₀ = 4Å
λ₀ = 2.2 Å
2
4
6
MOMENTUM (Å⁻¹)

Fig. 4·4

Table 4.1
Comparison of 4H5 and 7H

General Features	7H	4H5
Scattering Plane	horizontal	vertical
Number of Detectors	30	24
Scatter Angles (°)	Fixed range of 58 with first counter set 0-40	36-91
Solid angle per counter (ster)	5×10^{-5}	3.4×10^{-5}
Flight Path (m)	1.8	2.26
Nominal beam size at sample (cm)	2x1	2.5 x 5

Elastic Scattering by 2mm Vanadium Standard

	7H	7H	4H5	4H5	4H5*
Reactor power (MW)	22	22	22	22	17
Number of rotors	2	2	2	1	1
N_S/T_S slot curvature	10.2	7.6	3.125	3.125	3.125
Number of slots	1	1	6	6	5
Diameter (cms)	25	25	20	20	20
Rotor period	2208	2856	2118	2118	2118
Mean wavelength (Å)	2.2	3.95	4.08	4.18	4.21
Elastic peak $\Delta E(cm^{-1})$	9.6	3.2	1.5	2.6	3
$\Delta E/E_o$ FWHM (%)	17	15	8	16	18
Average counts per ctr min^{-1}	9.2 ≠	1.4 ≠	5.7	27.8	7.7
Counts cm^{-2} min^{-1}	4.6	0.7	0.5	2.2	0.6
Background cts min^{-1} per counter	3	2	15	80	8
Vanadium peak height/ background ratio after 20 hrs	126	22	15	15	8
Estimated incident flux n cm^{-2} sec^{-1} for 100% efficient counters	8×10^4	1.2×10^4	0.22×10^4	0.87×10^4	0.29×10^4

* No liquid hydrogen in source chamber.

≠ ^{3}He are approximately double these.

4.5 Data Collection

The events from 7H, 6H and 4H5 time of flight spectrometers are encoded and stored in a 12K PDP8 computer system, CASSANDRA (Hall and Egelstaff, 1970). For each machine a rotor pulse resets a crystal clock, which increments until an event (coded to refer to the originating counter) arrives. The clock time and the counter code together define that element of spectrum; sorting and accumulating of like events is performed using a magnetic drum as a backing store. The current spectrum of counts versus time for each scatter angle may be displayed on an oscilloscope. When sufficient data has been acquired the spectra are copied onto DEC magnetic tape and finally these recordings transferred to a standard IBM 9 track magnetic tape which is used for all subsequent data processing.

4.6 Calibration of Spectrometer using Vanadium

The scattering from vanadium is predominantly incoherent and with a high Debye temperature of 320K it is mostly elastic and isotropic. By measuring the integrated counts collected by each counter they may be normalised for their different efficiencies, and it is also possible to place an absolute scale on other spectral measurements, though an accuracy better than 15% is rarely achieved with the latter. Knowing the incident beam τ_o, the mean time of arrival of the x elastically scattered neutrons may be used to calculate the distance between the sample and detector. This procedure is used for gas filled proportional counters e.g. ^{3}He since they are physically thick and the mean position of ionisation is not predictable, unlike the case of the scintillation detectors. A program PRESCAT (Heard, Cocking, Baston: Wignall, 1967) performs this analysis, which may be cross-checked by the measured distance d between

sample and scintillators. Knowing the distance the final neutron energy and momentum are easily expressed in terms of the timing-gate-width/d, the number of μsec m^{-1} per channel. An estimate of the instrumental resolution may be made from the time width of the elastic peak at the detector.

4.7 The Pluto Triple-Axis Spectrometer

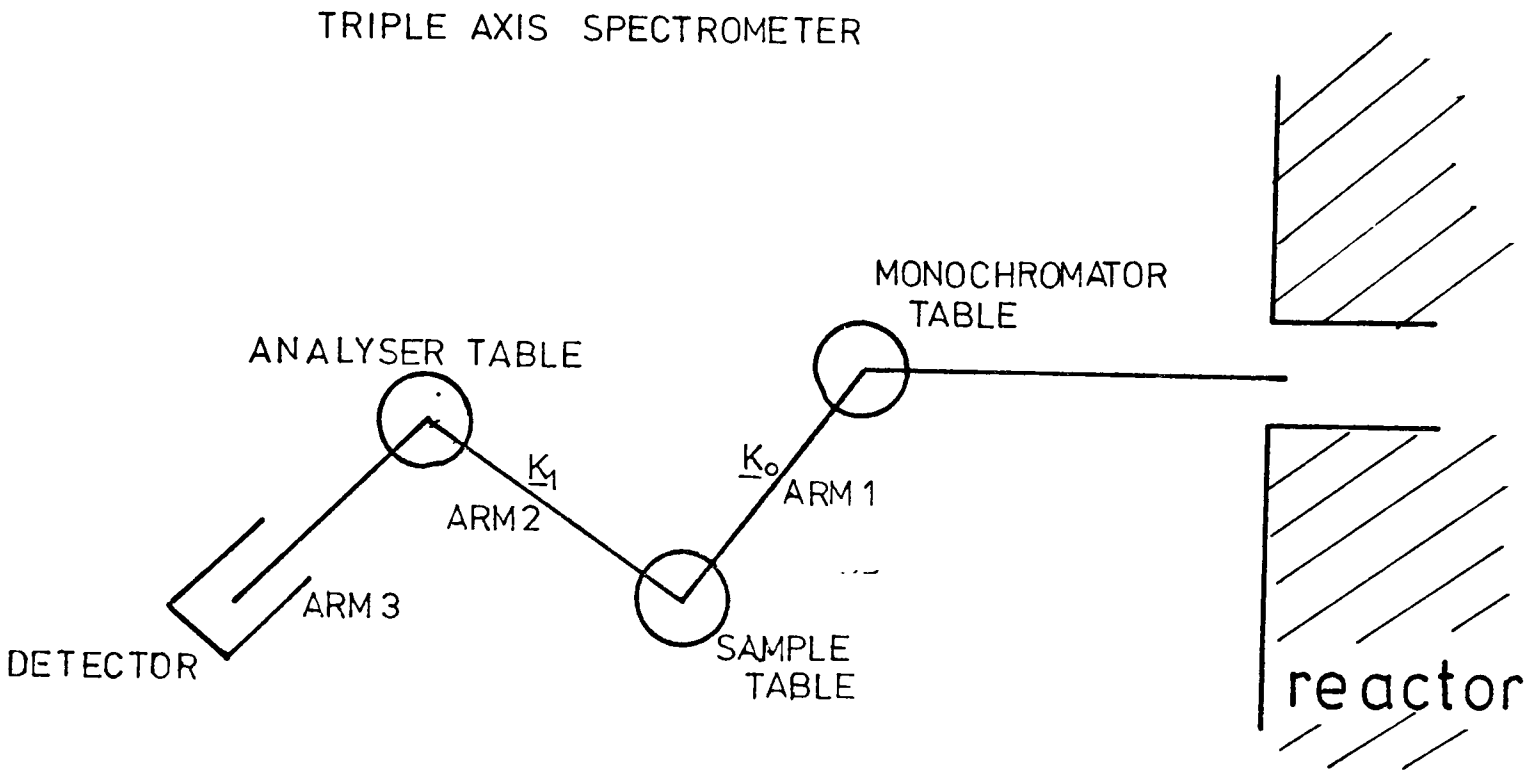
The incident and final neutron wavevectors on the sample are set and determined respectively by Bragg scattering at monochromating and analysing crystals, before being detected, (fig. 4.5).

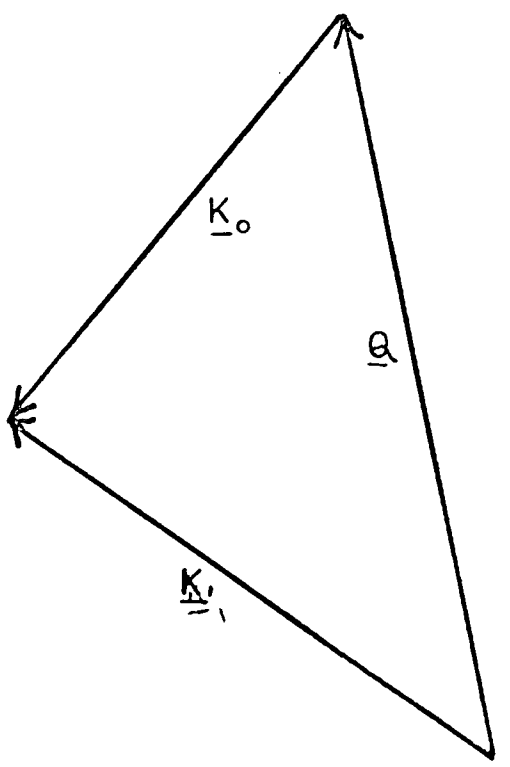
since $\underline{Q} = \underline{k}_1 - \underline{k}_o$ and $E = \hbar^2/2m\ (k_1^2 - k_o^2)$

suitably arranging the magnitudes of k_1 and k_o about a direction in the sample enables the measurement of $S(\underline{Q},\omega)$ directly. The positioning is achieved by having the three arms 1, 2, 3 and the three tables at their intersection independently positionable. Control is performed by a PDP8 computer which calculates setting angles given monochromator and analyser plane spacings, and zero angles, and calculates the positioning of the crystal gives the lattice parameters and zero angle.

The shaft settings are sensed by optical digitisers, and allowed to move when air pressure is applied between the flat floor and the instrument to raise it. Vertically lifting segments are included in the heavy shielding of the monochromator drum fig. 4.6 allowing it to rotate. A detailed description is given by Chumbley, Dyer and Wallis (1968). The advantage of choosing a $(\underline{Q},\omega)$ scan enables the path to be taken to cross the scattering surface in a favourable manner. The intensity of a phonon group is also a function of $\underline{Q}$ and by keeping it constant the integrated intensity of the $(\underline{Q},\omega)$ scan remains

Fig. 4·5


TRIPLE AXIS SPECTROMETER
MONOCHROMATOR TABLE
ANALYSER TABLE
K_1
ARM 2
K_o
ARM 1
ARM 3
DETECTOR
SAMPLE TABLE
reactor


K_o
Q
K_1

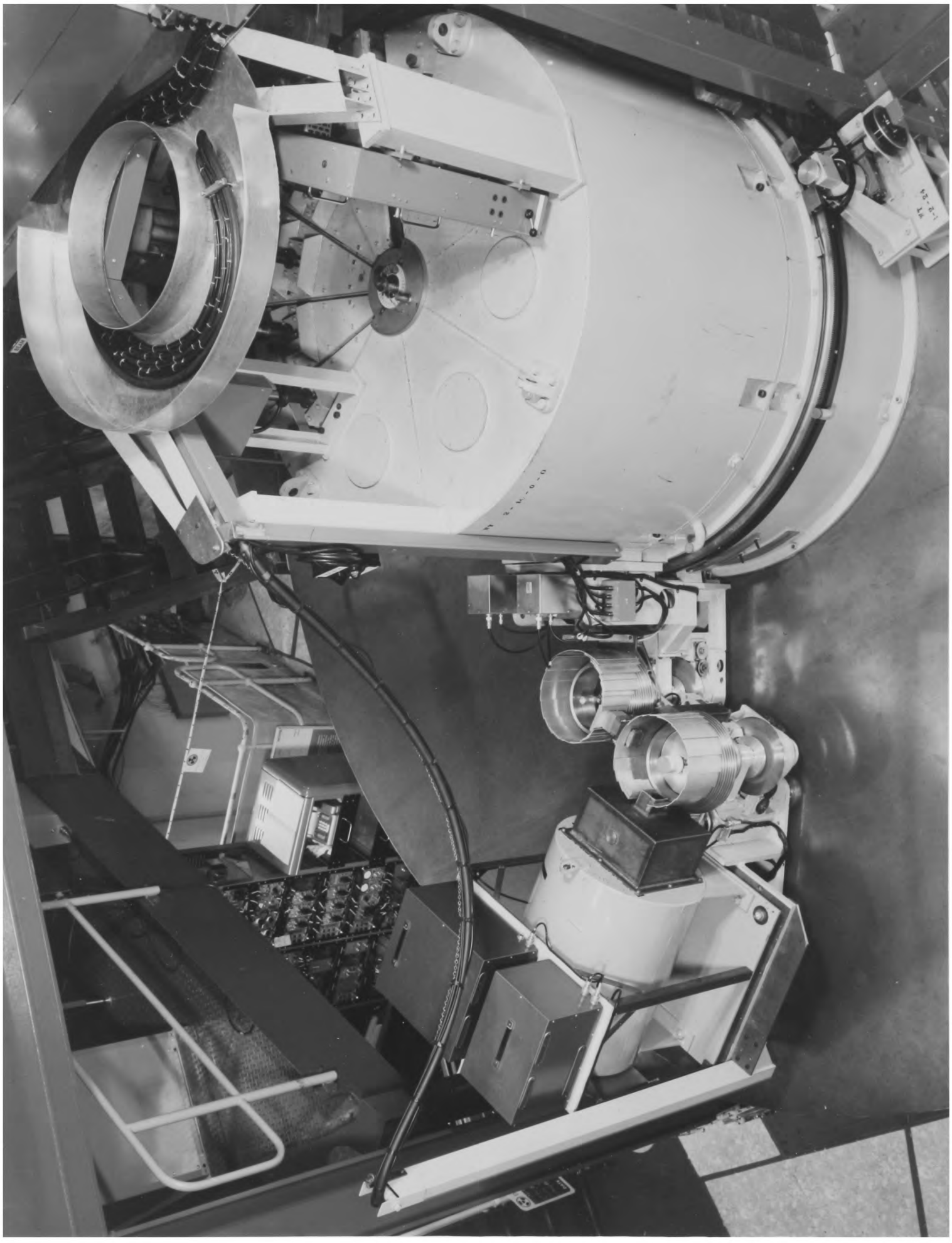


Fig 4.6 The Pluto Triple Axis Spectrometer

constant, and the width of the group a function of the intersection of the scan and the scattering surface, (Brockhouse, Becka and Rao, 1963).

The resolution is dependent on monochromator and analyser crystal mosaics and collimation angles giving in an ellipsoid in (Qx,Qy,E) where x and y are in the scattering plane: only with good knowledge of the gradients of the dispersion curves can these ellipsoids be set to minimise uncertainty in the measured peak position.

4.8 Choice of Specimen and Specimen Preparation

Urea, $CO(NH_2)_2$ was chosen for this experimental study. The crystal structure is tetragonal with two molecules per unit cell. The lowest internal mode frequency is 520 cm^{-1} and the small molecule may be treated in the rigid-body approximation. Directional intermolecular hydrogen bonding in all three directions suggest simple quadratic potentials might be applicable for these bonds. The hydrogen is readily substituted by deuterium reducing the interference from the incoherent cross-section in a coherent scattering experiment, without greatly changing the dynamical situation of the molecule.

The crystal morphology is simple with (110), (111) and (001) principal faces, and the reciprocal lattice of the primitive tetragonal structure is also simple tetragonal. The space group is D^3_{2d}. ($P\bar{4}2_1m$, no. 113 in the International Tables for X-ray Crystallography, 1969) and the molecular axes lie along symmetry directions, fig. 4.7. The small lattice (a = 5.662, c = 4.716 Å) enables $\underline{c}$ to be determined accurately in the large reciprocal lattice. The high solubility of urea in water and temperature dependence of this, plus the high probability of occluded water in the resulting crystal after

THE STRUCTURE OF UREA

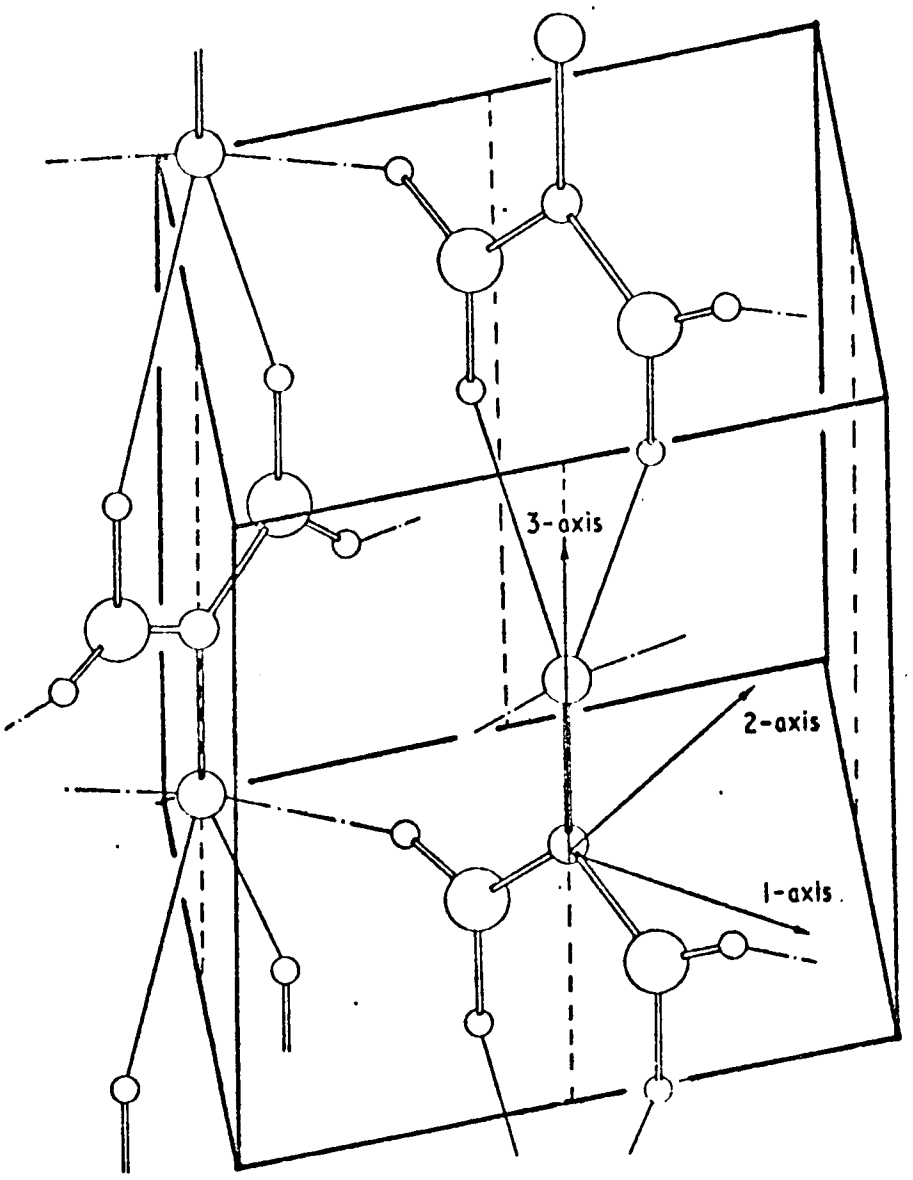


FIG. 4.7

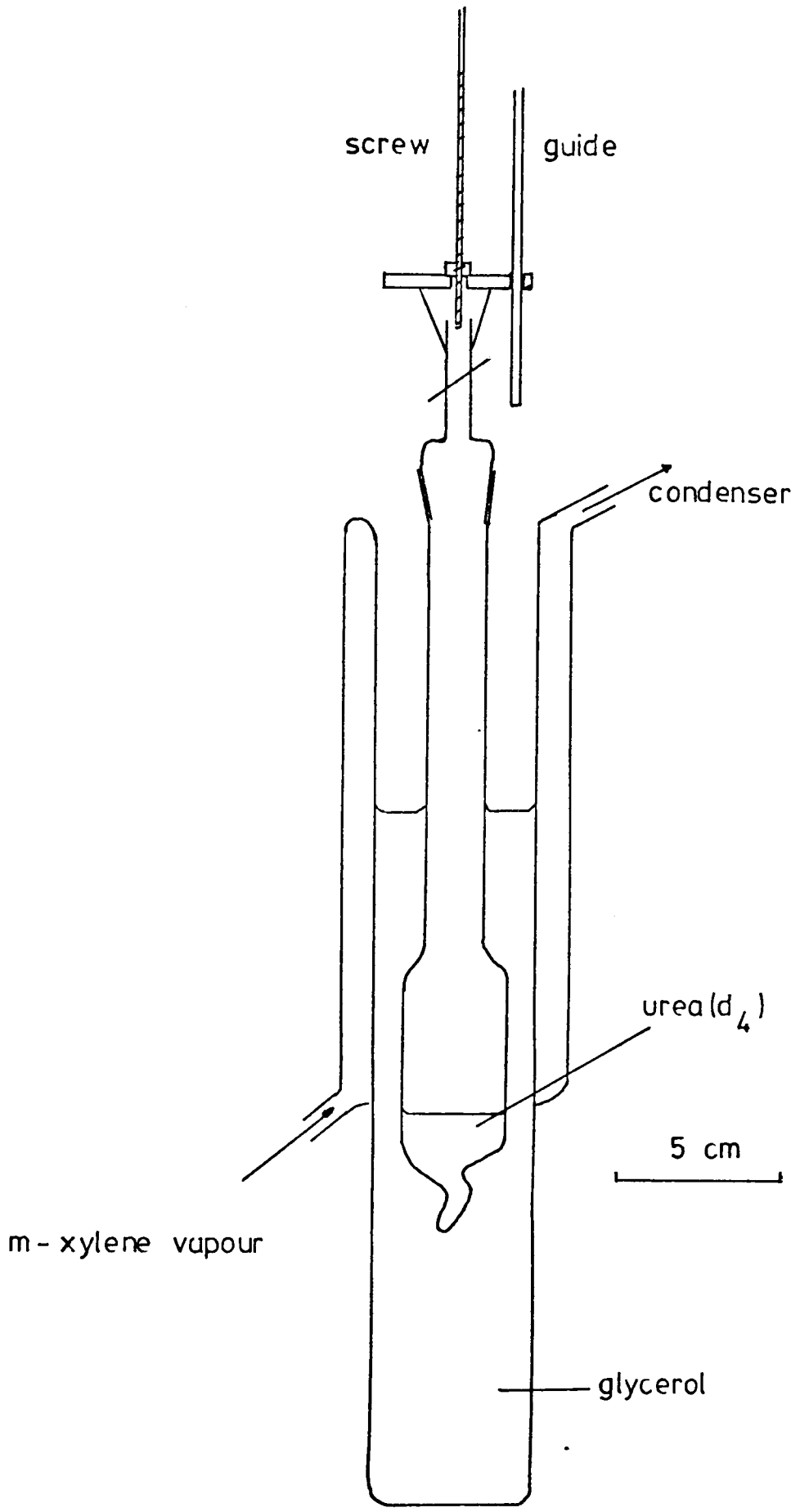
weeks of growth leads to the choice of crystallisation from a melt as a better procedure to adopt for a fully deuterated sample, where all the initial material would be available for a crystal. Urea (m.pt. 132°) does slowly decompose when heated to give condensation products including Biuret.

$$2CO(NH_2)_2 \rightarrow NH_2.CO.NH.CO.NH_2 + NH_3$$

Measurement of the volume of ammonia evolved indicated that only 3% of the sample would have decomposed after two days at 140°C in agreement with van Berkel (1958). By growing a crystal progressively from one end it was hoped that impurities would be concentrated in the melt. The sample material contained in an evacuated sealed tube was lowered from a hot zone through a temperature gradient (figure 4.8) using a lead-screw driven by a slow speed synchronous motor, the rate depending on the choice of motor speed and screw pitch, but usually 1.5 mm per hour. Uniform heating was achieved using a vapour jacket of gently refluxing m-xylene (Bpt. 138°C). Filling the tube with glycerol ensured temperature equilibration and, additionally, thermal inertia. Deuteration was performed in the growth tube by recrystallising from D_2O, with approximately 20 gms of D_2O used for the 10 gm of $CO(NH_2)_2$ at each stage. A small-scale experiment indicated that pumping off the D_2O residues to constant weight seven times would result in better than 99% deuteration (judged by the change of the N-H to N-D stretching frequencies in the infra-red). The D_2O residues were trapped with liquid nitrogen for assessment of the exchange by n.m.r. analysis. 0.5% w/w of urea nitrate was added to catalyse the exchange.

After final drying the tube was evacuated and crystal growth attempted. The partial pressure of ND_3 evolved corresponded

Fig. 4·8



UREA CRYSTALLISATION APPARATUS

to 2.8% decomposition in one case. The crystal was extracted after breaking the lower part of the tube. One crystal was grown from a sample of $CO(ND_2)_2$ (Kodak Ltd) which was put into the tube and sealed in a dry box.

4.9 Analysis of Crystals

Infra-red spectra in Nujol mulls of the melt recrystallised urea compared directly with those of the pure compound. Neutron Laue photographs showed that several large crystals were present, and it was necessary to cleave the boule to obtain individual crystals. Atmospheric exchange of deuterium was reduced by tightly wrapping the cleaved crystals in aluminium foil when on the spectrometers, the visible morphology being of considerable help in alignment. Diffraction measurements on these crystals, and normal solution grown specimens were identical (B.A. Wilson, private communication), both showing strong extinction for low order planes. The diffraction pattern was measured on a 'Badger' neutron diffractometer on DIDO reactor while rotating the crystal about first the <001> axis, then the $<1\bar{1}0>$ axis, fig. 4.9. One spurious peak was found also to be present in a background run and is labelled aluminium but no forbidden peaks were observed and the possibilities of crystal twinning and polycrystalline regions are eliminated. The crystal lattice parameter was also checked when orienting the crystal on the inelastic neutron spectrometers. A(220) Bragg peak rocking curve measured on the Pluto triple axis had a full width at half maximum of 0.55°, in the same order as instrumental resolution, and the mosaic spread in the crystal is therefore very small, as the extinction effects indicate.

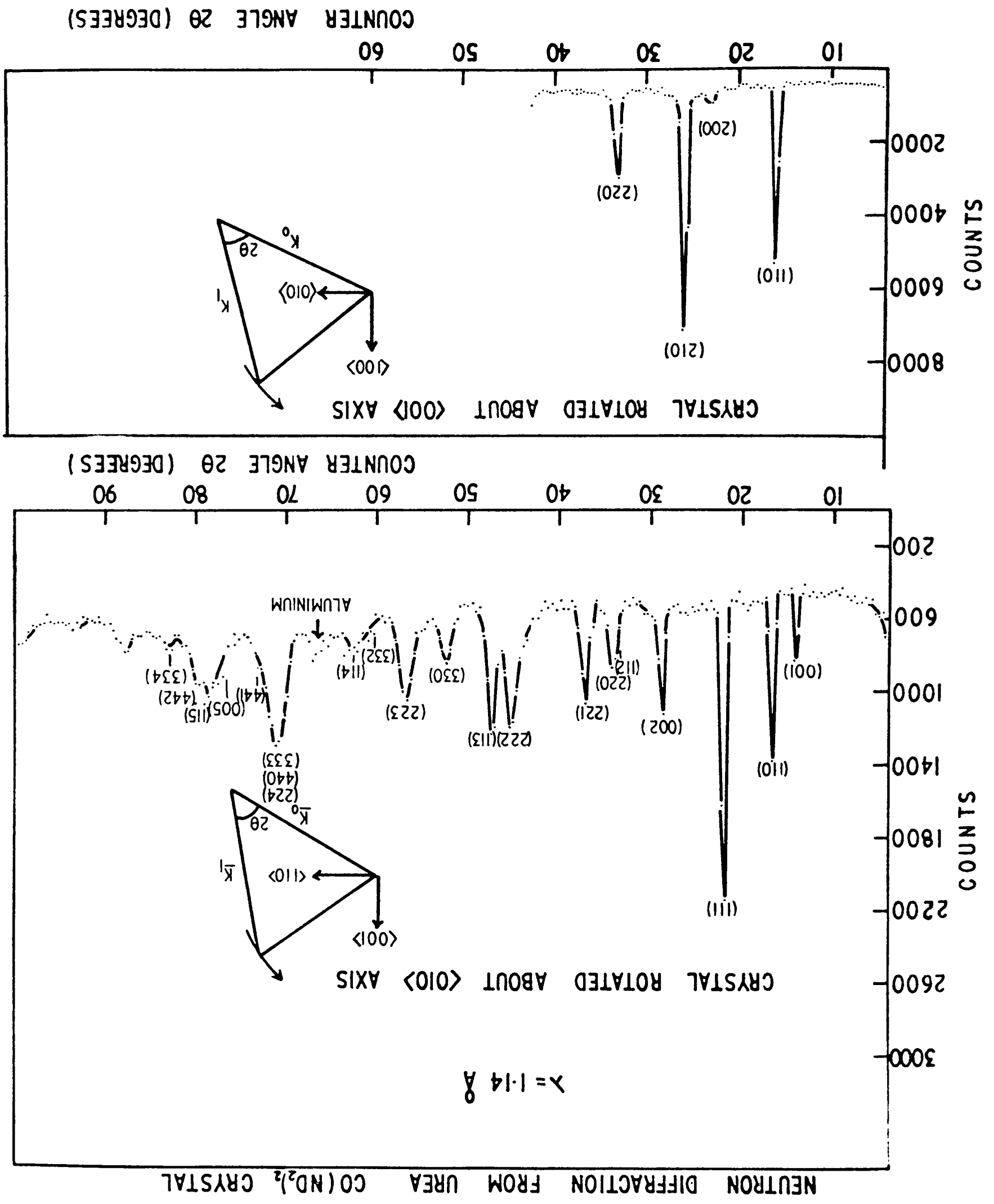

NEUTRON DIFFRACTION FROM UREA CO(ND2)2 CRYSTAL
λ = 1·14 Å
CRYSTAL ROTATED ABOUT ⟨010⟩ AXIS
⟨001⟩
⟨110⟩
2θ
COUNTS
COUNTER ANGLE 2θ (DEGREES)
CRYSTAL ROTATED ABOUT ⟨001⟩ AXIS
⟨100⟩
⟨010⟩
2θ
COUNTS
COUNTER ANGLE 2θ (DEGREES)
ALUMINIUM
(001)
(110)
(111)
(002)
(221)
(220)
(330)
(223)
(114)
(332)
(115)
(005)
(441)
(442)
(334)
(200)
(210)
(220)
(110)

Fig. 4·9

CHAPTER 5

Experiments with Single Crystals of Deutero-Urea

5. Experiments with Single Crystals of Deutero-Urea

The two types of instrument described in section four have been used to examine the dispersion relations in a single crystal of Urea (d_4). Results are given here together with an assessment of the techniques used applied to molecular crystal systems.

5.1 Measurements with the PLUTO triple axis spectrometer

The calculated and experimental dynamical structure factors of molecular crystals are found to vary rapidly with position in the Brillouin zone; an order of magnitude in 0.5 $\mathring{A}^{-1}$ is frequently observed with the corresponding effect on the observed intensity (Reynolds, Kjems and White, 1972). Without very reliable calculation of eigenvectors and hence the cross-section, systematic study of the dispersion relations is difficult. There has been success in only one experiment using a triple axis spectrometer, for Hexamine (Powell, 1968) after which refinements were made to the model used to calculate the original eigenvectors.

Initial experiments were performed on the DIDC triple axis spectrometer which then had a hot-source to increase the available flux at shorter wavelengths. With high incident energies no phonon groups were observed at all in constant $\underline{Q}$ scans, principally because of the low resolution in both $\underline{Q}$ and ω, and very low counting rates comparable with the background. Any intense low energy acoustic modes merged with the incoherent elastic peaks.

After a number of time of flight experiments it was apparent that a study of the (210) Brillouin zone might result in observable groups for some branches. Performing energy scans between 0 and 80 cm^{-1}, in 4 cm^{-1} steps, at constant $\underline{Q}$ at five

positions along a direction (2ξ0), counting for 15 minutes at each setting, phonon groups were observed and are shown in figure 5.1a. The dispersion relation ω(q) corresponding to these groups is shown in figure 5.1b. The slope of this acoustic mode lies between the velocity of sound values obtained for the longitudinal ($V_{L_{110}}$) and transverse ($V_{T_{110}}$) modes obtained by ultrasonic experiments (Fischer and Zarembowitch, 1970): since $\underline{Q}$ is not propogating along a crystal symmetry direction the polarisation is of mixed character. Assuming the crystal mosaic to be very small the resolution at zero energy transfer was estimated by stepping across the (200) Bragg peak and measuring the widths of the rocking curves, (full widths at half maximum, FWHM), the results being (Δq_x, Δq_y, ΔE) = (0.045 $\mathring{A}^{-1}$, 0.045 $\mathring{A}^{-1}$, 4 cm^{-1}). The rise in background levels due to the incoherent elastic scattering at zero energy transfer is evident. The molecular form factor, $\sum_i b_i \exp(i\,\underline{Q}.\underline{\rho})$ which appears, rather modified, in equation 3.9 was calculated for each $\underline{Q}$ value, and varies from 0.97 at (Qx,Qy) = (2, 1.1) to 0.25 at (Qx,Qy) = (2, 1.5); other terms in eq. 3.9 must therefore be considered to account for the marked change in intensity.

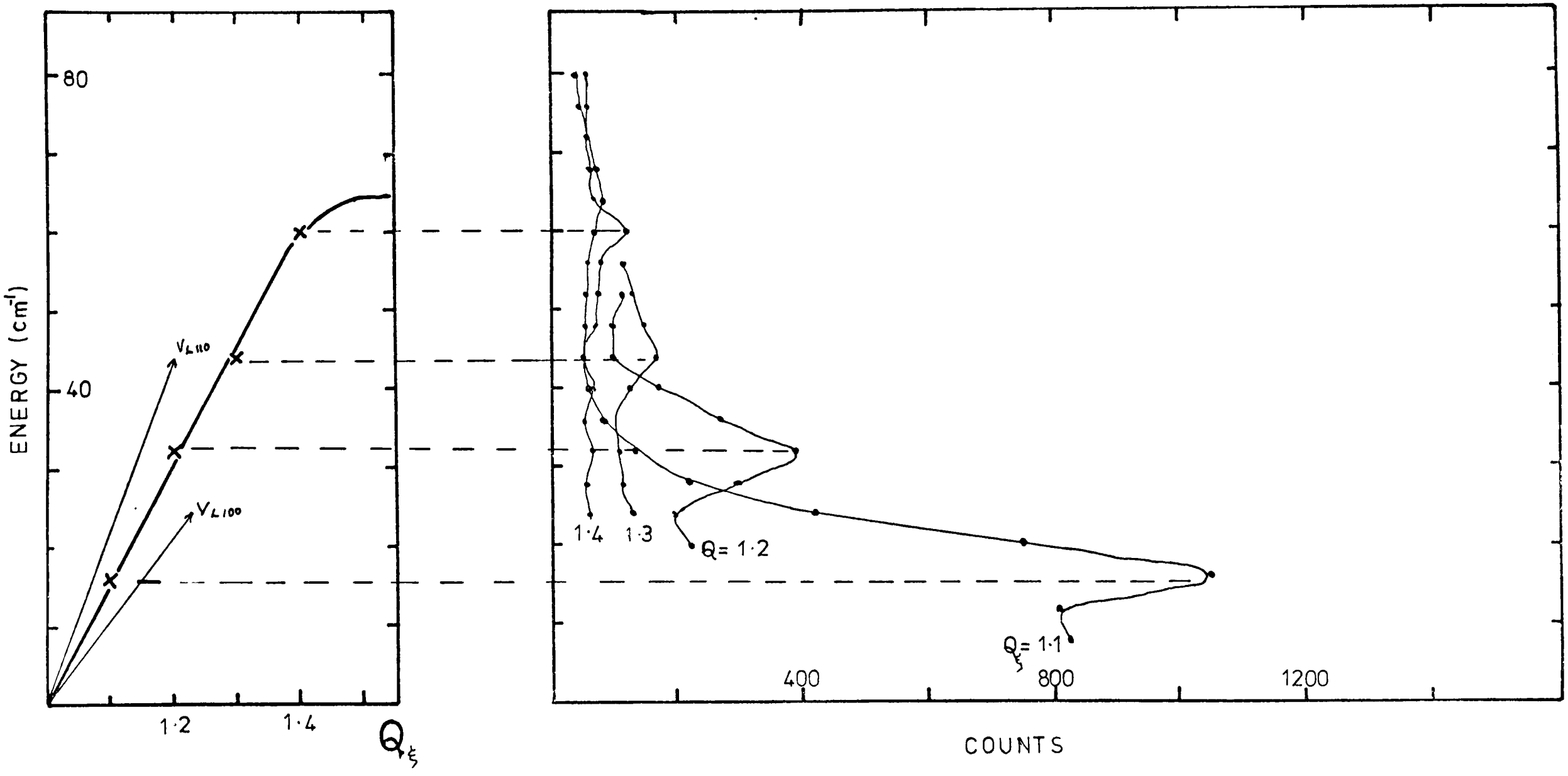
5.2 Measurements with Time of Flight Spectrometers

The remaining experiments on coherent scattering from the perdeutero urea crystals used the multi-detector arrays on the 4H5 and 7H time of flight spectrometers with incident wavelengths of 4 $\mathring{A}$ and 2.2 $\mathring{A}$. Without the aid of symmetry arguments and use of optical data assignment becomes very difficult and the results presented here will be for modes propogating in the <001> and <110> directions and points of high symmetry in the Brillouin zone are shown in figure 5.2 with Kovalevs classification (1965).

Fig. 5·1

UREA (d_4)

PLUTO TRIPLE AXIS SCANS ALONG $<2\xi 0>$



SYMMETRY OF THE BRILLOUIN ZONE

OF UREA

(Kovalev's classifications)

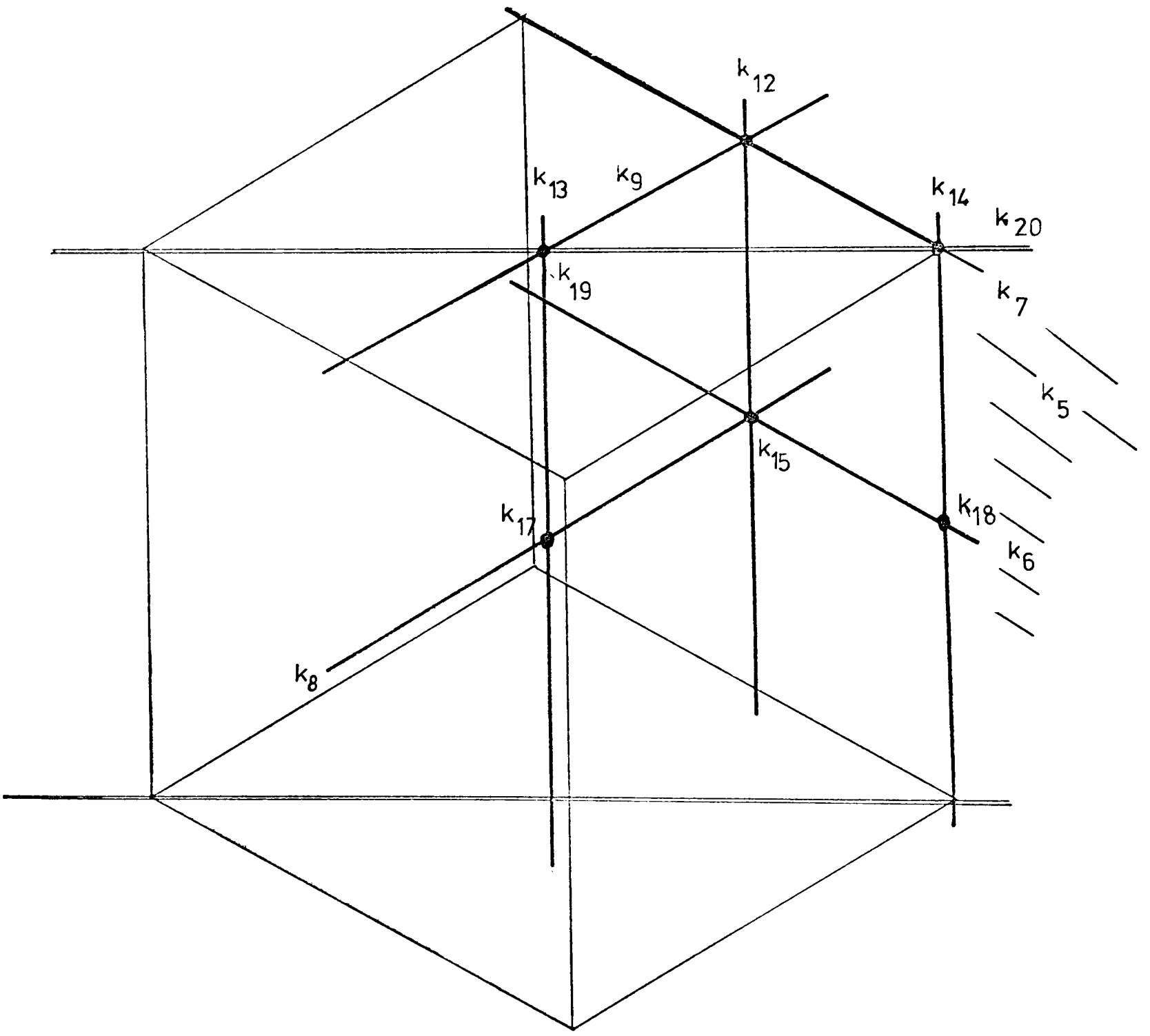


Fig. 5·2

5.2.1 Results in<001>Direction

One hundred and twenty six spectra were recorded in five experiments each lasting about twenty four hours with the (00ξ) reciprocal lattice vectors in the scattering plane of the spectrometer. A good inelastic time-of-flight spectrum is shown as crosses in figure 5.3 after grouping together pairs of time channels. The program FANDS has been used to fit four Gaussian peaks to this spectrum, the sum of these being shown as the curve marked by plus signs. Fitting the curve to the spectrum on a time of flight scale, $\frac{d^2\sigma}{d\Omega d\tau}$ versus τ rather than an energy cross-section $\frac{d^2\sigma}{d\Omega dE}$ versus E introduces some errors, as do the lack of corrections for the energy dependence of the detector efficiencies, but the error in the final peak position is small and is ignored in this approximation. As a subjective indication of reliability peaks are graded 2, 3, or 4 corresponding to well defined, probable and possible, 1 is used for exceptionally sharp peaks which may result from the spectrometer $(\underline{Q},\omega)$ scan cutting the scattering surface in an exceptionally favourable manner to optimise the intensity, and zero is used for dubious peaks occurring in the extrapolations of the well defined peaks, to spectra from other detectors.

Table 5.1 indicates the relationship between the reciprocal lattice and the scattering plane for each of the experiments. To make greater use of the more numerous off-symmetry groups obtained in a time-of-flight experiment, longitudinal modes where $\underline{Q}$ had a major component along the <00ξ> were also utilised, though $\underline{q}$ was still required to be along the 00ξ direction. In these cases (the (113), (112) and (102) zones there is a greater possibility of exciting the transverse modes.

Table 5.1

Relationship of mode polarisations to scattering plane

Run No.	Spectrometer	Scattering plane		Symmetry class for propogation along (00ξ)		Symmetry class for propogation along (ξξ 0)
		x	y	Longitudinal	Transverse	Transverse
4061	4H5	110	001	A_1+A_2	B_1	A'
4062	4H5	110	001	A_1+A_2	B_1	A'
4088	4H5	100	001	A_1+A_2	B_1+B_2	-
4089	4H5	100	001	A_1+A_2	B_1+B_2	-
5	7H	110	001	A_1+A_2	B_1	A'

Experimental Spectrum and Fitted Curve

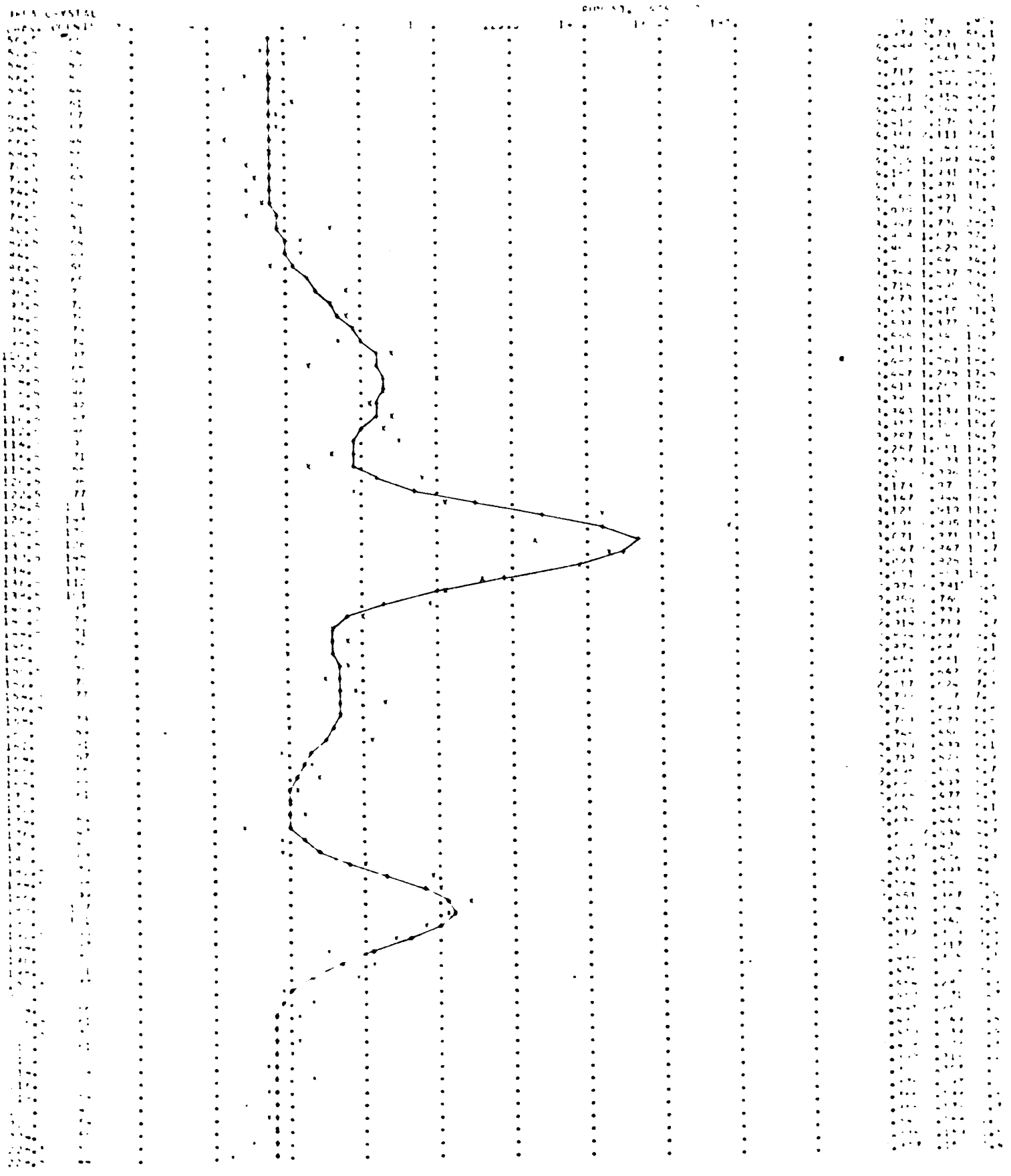


Fig. 5·3

The observed peaks fulfilling these criteria are listed in table 5.2. Positions in (q_x, q_y, Energy) are given and also the momentum transfer is reduced to the first zone to give q_x and q_y. For additional help in defining the reliability of a group position, the peak height above background, and background levels are given, which are used in conjunction with the reliability estimate to distinguish large but broad, hence indeterminately positioned peaks from those that are well defined.

The distinction between longitudinal and transverse modes has been made on the basis of the angles A1 between $\underline{Q}$ and the τ_x axis, A2 between $\underline{\tau}$ and the τ_x axis, and A3 between $\underline{q}$ and the τ_x axis, and these are also tabulated in 5.2. For a longitudinal mode along (00ξ) $\underline{Q}$ and $\underline{q}$ are parallel to τ_{001} for a transverse mode $\underline{Q}$ is perpendicular to $\underline{q}_{00\xi}$. Seventy peaks observed fulfilled neither of the two conditions and are not listed here. Of the remaining groups eighteen were classified as transverse and twelve as longitudinal. In addition a number corresponded to transverse modes propogating along the (ξξ0). Since the momentum resolution of the spectrometers is limited some relaxation has been allowed in the specific direction of $\underline{q}$.

5.2.2 Results in <110> direction

Twenty experiments on 4H5 and 7H with incident and final wavevectors k_o and k_1, in the plane of the τ_{100} and τ_{010} lattice vectors gave five hundred and eighty spectra yielding five hundred and sixty five peaks. In addition some data from the experiments with the τ_{110} and τ_{001} lattice vectors in the scattering plane are also used in this section. One hundred and nine of the former and twelve of the latter were found to have $\underline{Q}$ terminating in a (ξξ0) zone. Since the lattice had been defined in terms of the <100> and <010> as x and y coordinates, |Q|

and $|q|$ were also calculated and used to define the position in the <110> direction.

Figure 5.4 shows the scattering measured in one run in twenty counters. The intensity is plotted against the scattered wavevector k_1. Figure 5.5 shows the relationship between the scattered wavevector and observed peaks. The spectrum versus k_1 for one counter at 83° is shown, and corresponding to it the reciprocal lattice diagram with the peak positions observed in the twelve adjacent counters also marked. For a simple monatomic lattice there would be little to confuse the nature of each branch observed and accurate analysis of $\underline{q}$ and ω may be performed by interpolation to positions of high symmetry. In this more complex case the groups are not necessarily simply related and this method (Squires 1966) was not used.

The peak at $k_1 = 1.56$ Å^{-1} is the incoherent elastic peak, and taking this as an indication of the uncertainty in $\underline{Q}$ the deviation is less than one tenth of the Brillouin zone. The dispersion of the modes is apparent as is the general low symmetry of the wavevectors $\underline{Q}$ and $\underline{q}$. At $k_1 = 2.5$ Å^{-1}, the energy transfer is 60 cm^{-1} which corresponds to a peak in the density of states which appears as a contibution from incoherent scattering. This is dispersionless, the locus lying on a circle about k_1 equal to zero, corresponding to constant energy transfer. These peaks were not included in the analysis. Because the incoherent scattering is isotropic to a first approximation, little is collected in the small aperture counters.

By working with long incident wavelengths the absolute energy resolution reduces problems of incoherent elastic scattering obscuring the low energy phonons. Longer counting periods than the twenty or thirty hour run times used might have revealed

COHERENT SCATTERING IN THE BASAL PLANE OF UREA

AT TWENTY SCATTER ANGLES

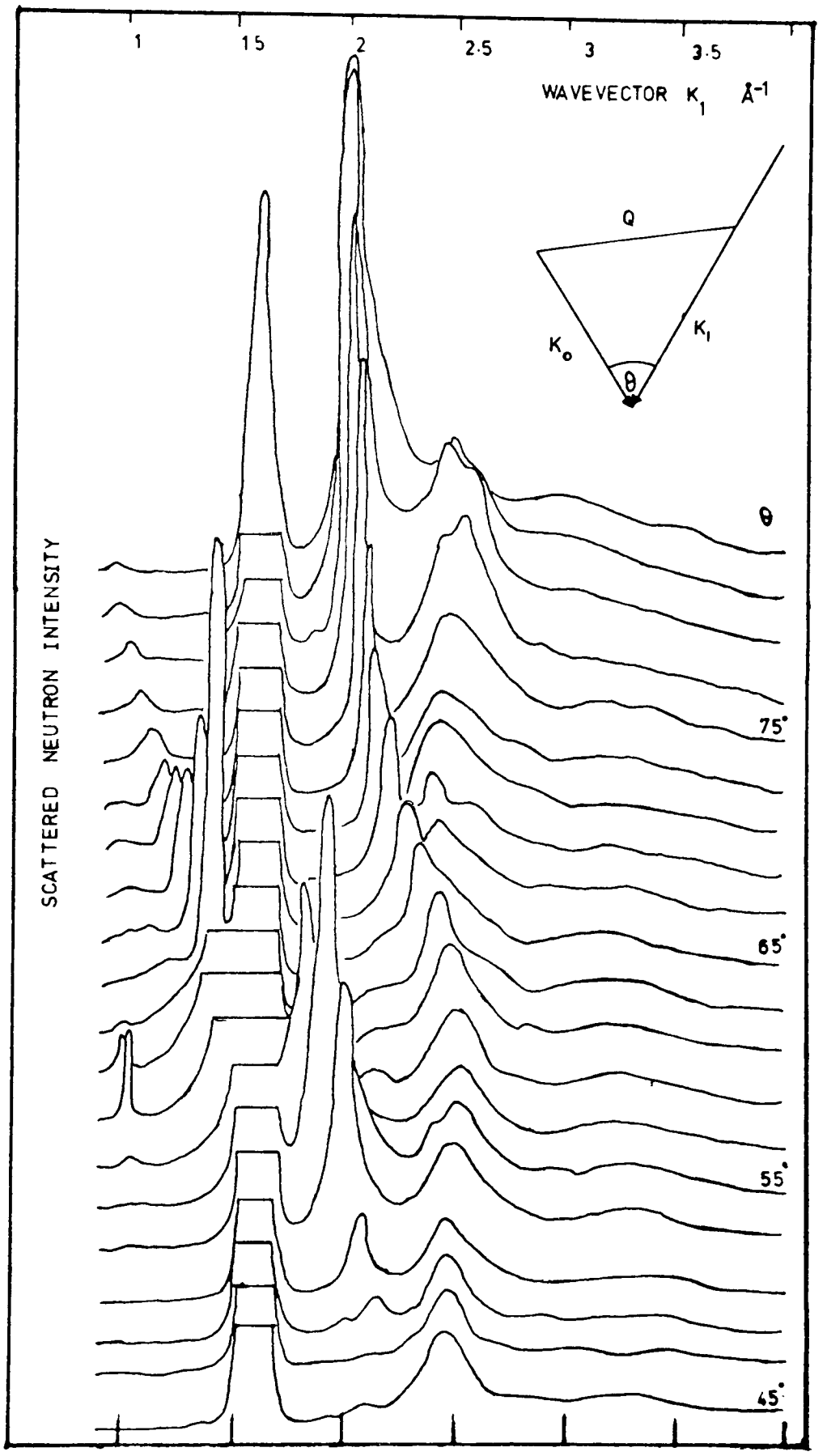
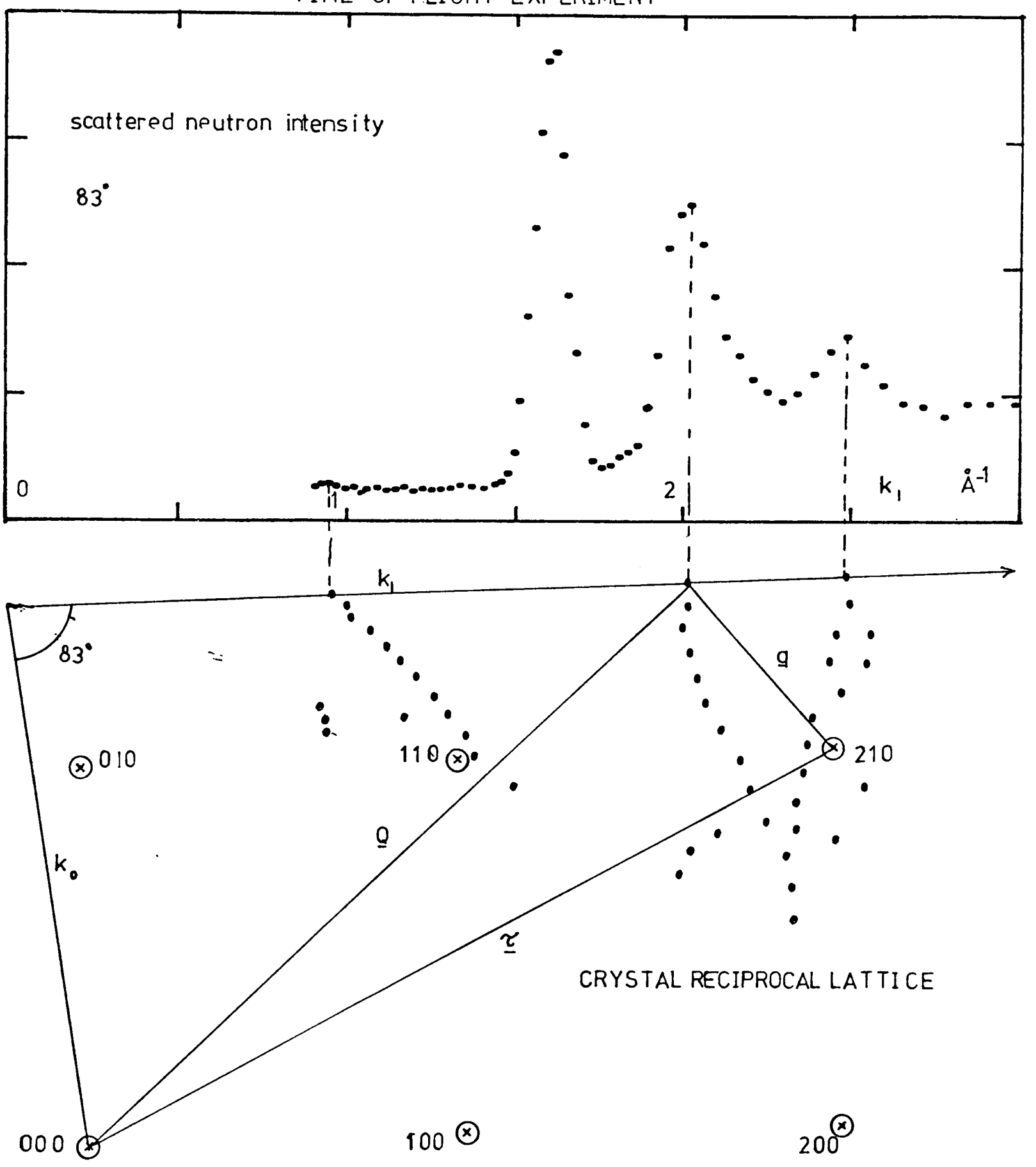


Fig. 5·4

Fig. 5·5

GRAPHICAL ANALYSIS OF THE COHERENT TIME OF FLIGHT EXPERIMENT



more high energy phonons.

Table 5.3 includes results for the longitudinal and transverse modes, with in addition to angle and reliability classification, values of $|Q|$ and $|q|$. Angles are given with reference to τ_{100} as zero. The Qx and Qy values have been given in the first octant of reciprocal space, this being the smallest irreducible zone.

5.3 Assignment of Modes

The assignments given here are based on available optical data and elastic constant measurements for hydrogenous urea, with help from simple group theoretical arguments. The Raman spectrum has been studied by Couture-Mathieu (C-M) (1949), Arnau and Giguere (A-G) (1969), Lefebre and Wallart (L-W) (1970), who observe lattice modes at 58, 102, 135 and 177 cm^{-1} and assign them as indicated in table 5.4. In laser Raman studies with single crystals Meier (1960) and Geddes and Bottger (G-B) (1971) use polarisation analysis to reassign the A_1 mode at the higher value. Also given are the velocities of sound for longitudinal and transverse propogation from elastic constant measurements, (Fischer and Zarembowitch, 1970). A higher value for the A_1, the antiphase 3 axis translation seems physically more reasonable for this lattice. The ratio of the moments of inertia for fully deuterated and hydrogenous urea are:

	$\sqrt{I_D/I_H}$
1-axis	1.034
2-axis	1.067
3-axis	1.099

where the axes are as in fig. 4.7, and frequency shifts on deuteration are as expected correspondingly small.

Eleven eigenvalues of the normal modes are therefore known

TABLE 5.2

<00ξ> LONGITUDINAL PHONONS

Run No.	Q_x	Q_y	Zone	q_x	q_y	E	S	B	R	A1	A2	A3
4061016	0.230	3.250	002	0.147	0.447	25.5	69	319	3	86	90	69
4061017	0.152	3.030	002	0.097	0.282	22.8	43	218	4	87	90	68
4061018	0.066	3.140	002	0.042	0.364	25.5	70	317	3	89	90	82
4061019	0.198	3.033	002	0.126	0.284	25.0	60	289	4	86	90	62
4089002	0.025	3.019	002	0.023	0.273	8.9	29	44	0	90	90	86
4089003	0.087	2.921	002	0.078	0.200	8.3	19	76	4	88	90	72
4089010	1.250	2.952	102	0.127	0.223	18.0	18	88	0	67	67	65
4089006	0.770	3.325	103	-0.306	-0.496	16.1	24	91	0	77	74	63
4089007	0.947	3.231	102	-0.146	0.433	17.6	22	94	0	74	67	-73
4089008	0.979	3.068	102	-0.117	0.310	16.4	23	79	0	72	67	-71
4089009	1.070	2.975	102	-0.035	0.240	16.4	23	117	0	70	67	-82
5020	0.068	4.139	003	0.043	0.117	-3.2	800	200	1	89	90	66

TABLE 5.2

<00ξ> TRANSVERSE PHONONS

Run No.	Q_x	Q_y	Zone	q_x	q_y	E	S	B	R	A1	A2	A3
4061007	1.597	1.565	111	0.019	0.178	3.01	200	266	1	44	40	83
4061008	1.516	1.562	111	-0.033	0.176	3.01	600	200	1	46	40	-77
4062002	3.065	0.865	221	-0.044	-0.349	11.0	94	55	2	16	23	82
4062003	3.037	1.000	221	-0.062	-0.247	11.9	111	98	2	18	23	74
4062006	3.037	1.609	221	-0.062	0.212	17.8	62	112	3	28	23	-70
4062007	3.087	1.930	221	-0.030	0.453	22.0	66	85	3	32	23	-85
4062008	3.128	2.286	222	-0.004	-0.279	27.0	64	87	3	36	40	89
4088005	2.426	0.697	201	0.188	-0.475	5.0	21	44	4	16	31	-71
4088006	2.355	0.761	201	0.124	-0.427	5.0	22	64	3	18	31	-75
4088007	2.302	0.848	201	0.076	-0.361	5.5	25	57	4	20	31	-79
4088008	2.291	0.906	201	0.066	-0.318	5.6	20	52	3	22	31	-79
4088009	2.177	1.004	201	-0.037	-0.244	6.1	22	77	3	25	31	83
4088012	2.347	2.278	202	0.116	-0.285	21.0	14	50	4	44	50	-7)
4088023	0.887	0.724	101	-0.200	-0.455	1.7	18	90	4	39	50	7J
4089018	2.063	2.021	202	-0.140	-0.478	21.4	30	108	4	44	50	76
4089019	2.190	1.903	201	-0.025	0.433	22.7	20	101	4	41	31	-86
4089021	2.169	1.582	201	-0.044	0.191	21.1	21	113	4	36	31	-78
4089020	2.368	1.789	201	0.135	0.347	24.8	24	125	4	37	31	72

Run No.	Q_x	Q_y	|Q|	Zone	q_x	q_y	|q|	E	S	B	R	A1	A2	A3
4002	2.8220	2.8210	3.9902	330	-0.4554	-0.4563	0.6447	54.1	92	56	2	45	45	45
4021	1.1320	1.1680	1.6265	110	0.0532	0.0207	0.0571	-1.21	500	50	12	46	45	69
8013	1.5325	1.3450	2.0390	110	0.3819	0.2128	0.4372	-9.2	25	80	3	41	45	29
8023	2.0620	1.7980	2.7358	220	-0.1407	-0.3787	0.4040	-8.3	80	180	2	41	45	70
8024	1.9970	1.9150	2.7668	220	-0.1993	-0.2732	0.3382	-9.3	60	180	3	44	45	54
8025	1.9610	2.0080	2.8067	220	-0.1894	-0.2317	0.2993	-9.8	70	100	3	46	45	39
8026	1.9390	2.0890	2.8502	220	-0.1163	-0.2516	0.2772	-10.3	30	70	3	47	45	25
9017	2.1150	1.9290	2.8626	220	-0.0929	-0.2606	0.2767	-10.3	70	45	4	42	45	70
9018	2.0820	2.0160	2.8981	220	-0.1226	-0.1821	0.2195	-10.8	125	98	4	44	45	56
9019	2.0090	2.1170	2.9185	220	-0.0911	-0.1885	0.2094	-11.6	110	100	4	46	45	26
9026	2.5910	2.3970	3.5297	220	0.3363	0.1614	0.3730	-8.0	160	90	2	43	45	26
9027	2.5430	2.4780	3.5507	220	0.2931	0.2344	0.3753	-8.5	145	80	3	44	45	39
9028	2.4880	2.5560	3.5670	220	0.3048	0.2435	0.3901	-9.1	144	70	3	46	45	51
9028	2.4720	2.5580	3.5573	220	0.3066	0.2290	0.3827	-4.2	140	80	3	46	45	53
9029	2.4570	2.6270	3.5969	220	0.3688	0.2155	0.4271	-9.4	101	60	3	47	45	60
9030	2.4390	2.6950	3.6348	220	0.4301	0.1993	0.4740	-9.5	140	120	4	48	45	65
4083004	1.7200	1.8120	2.4983	220	-0.3661	-0.4491	0.5794	4.1	30	70	4	46	45	39
4083005	1.6770	1.7220	2.4037	220	-0.4473	-0.4878	0.6618	3.6	90	80	2	46	45	43
4084003	1.6900	1.7230	2.4135	220	-0.4463	-0.4761	0.6526	2.7	79	53	3	46	45	43
4084003	2.1120	1.7730	2.7575	220	-0.0956	-0.4013	0.4125	6.4	34	53	3	40	45	77
4085014	2.1420	2.0890	2.9920	220	-0.0685	-0.1163	0.1350	7.0	44	103	2	44	45	60
4086011	1.5480	1.3580	2.0592	110	0.3959	0.2245	0.4551	3.5	20	40	4	41	45	30
4086002	2.2640	2.3830	3.2870	220	0.1488	0.0415	0.1545	12.3	30	50	3	46	45	74
4086003	2.3590	2.2890	3.2870	220	0.1271	0.0640	0.1423	13.1	400	250	3	44	45	27
4086004	1.9540	2.0570	2.8371	220	-0.1452	-0.2381	0.2789	8.0	360	270	3	46	45	31
4086005	2.0070	1.9640	2.8081	220	-0.1903	-0.2290	0.2977	8.3	168	70	3	44	45	50
4086006	2.0390	1.8580	2.7586	220	-0.1614	-0.3246	0.3625	8.4	70	140	3	42	45	64
4086007	2.0170	1.7490	2.6697	220	-0.1812	-0.4229	0.4601	8.0	540	350	3	41	45	67
4086008	1.6060	1.6120	2.2755	110	0.4536	0.4482	0.6377	4.1	90	140	2	45	45	45
4086009	1.6630	1.5300	2.2597	110	0.4995	0.3796	0.6274	4.5	90	80	2	43	45	37
4087006	1.8790	2.0320	2.7676	220	-0.1677	-0.3057	0.3487	8.5	38	57	4	47	45	29
4087007	2.0760	1.9650	2.8585	220	-0.1280	-0.2281	0.2616	10.5	48	36	4	43	45	61
4087007	1.9080	1.9250	2.7104	220	-0.2642	-0.2795	0.3846	8.6	33	36	2	45	45	43
4087008	1.9130	1.8230	2.6425	220	-0.2750	-0.3562	0.4500	8.4	23	46	3	44	45	52
4087011	1.6210	1.4960	2.2058	110	0.4617	0.3490	0.5788	5.2	28	33	2	43	45	37
4087010	1.5790	1.5850	2.2373	110	0.4292	0.4238	0.6032	4.9	40	50	2	45	45	45
4087015	1.2030	1.1450	1.6608	110	0.0848	0.0325	0.0908	1.9	80	30	2	44	45	21
4177002	1.8260	1.7180	2.5071	220	-0.3535	-0.4509	0.5730	2.8	310	100	3	43	45	52
4177003	1.7400	1.6800	2.4187	220	-0.4310	-0.4851	0.6489	2.4	510	200	3	44	45	48
4177004	1.6680	1.6910	2.3752	220	-0.4752	-0.4959	0.6868	2.5	520	150	3	45	45	44

TABLE 5.3

<ξξ O> IN PLANE TRANSVERSE PHONONS

Run No.	Q_x	Q_y	|Q|	Zone	q_x	q_y	|q|	E	S	B	R	A1	A2	A3
4001	1.2920	0.7650	1.5015	110	0.1650	-0.3102	0.3514	10.8	173	67	4	31	45	-61
4002	1.3560	0.6860	1.5196	110	0.2227	-0.3814	0.4417	10.5	162	56	4	27	45	-59
4003	1.5470	0.7830	1.7339	110	0.3950	-0.2940	0.4924	12.7	129	41	4	27	45	-36
4005	1.6620	0.6600	1.7883	110	0.4986	-0.4049	0.6423	11.9	168	49	3	22	45	-38
4015	1.5270	0.6090	1.6440	110	0.3769	-0.4509	0.5877	2.91	180	54	2	22	45	-49
4016	1.4930	0.7050	1.6511	110	0.3463	-0.3643	0.5026	2.31	306	28	2	25	45	-45
4017	1.4260	0.8110	1.6405	110	0.2858	-0.2687	0.3923	1.51	302	56	2	30	45	-42
4022	1.0820	1.2330	1.6404	110	0.1118	-0.0243	0.1144	-1.6	280	30	2	49	45	-77
4023	1.0310	1.2940	1.6545	110	0.1668	-0.0703	0.1810	-2.0	138	10	2	51	45	-66
4024	0.9980	1.3450	1.6748	110	0.2128	-0.1001	0.2352	-2.2	96	18	2	53	45	-64
4025	0.9460	1.3980	1.6880	110	0.2606	-0.1470	0.2992	-2.5	180	40	2	56	45	-60
4026	0.9030	1.4450	1.7039	110	0.3030	-0.1858	0.3554	-2.7	160	90	3	58	45	-57
4027	0.8570	1.4890	1.7180	110	0.3427	-0.2272	0.4112	-3.0	183	70	3	60	45	-55
8006	1.3650	0.6040	1.4927	110	0.2308	-0.4554	0.5105	-4.3	40	150	3	24	45	-62
8007	1.4665	0.5900	1.5807	110	0.3224	-0.4680	0.5683	-3.7	30	180	4	22	45	-54
8010	1.6390	0.8150	1.8304	110	0.4779	-0.2651	0.5465	-4.8	120	300	2	26	45	-28
8026	2.7440	1.7180	3.2374	220	0.4743	-0.4509	0.6544	-2.0	660	600	2	32	45	-43
8027	2.7150	1.8320	3.2753	220	0.4482	-0.3481	0.5675	-2.8	800	500	2	34	45	-37
8028	2.6960	1.9360	3.3191	220	0.4310	-0.2543	0.5004	-3.4	1200	300	2	36	45	-30
8029	2.6630	2.0410	3.3552	220	0.4013	-0.1596	0.4319	-4.1	1200	300	2	37	45	-21
9020	2.6340	1.9100	3.2536	220	0.3751	-0.2777	0.4667	-6.3	325	120	2	36	45	-36
10018	2.3790	1.6820	2.9135	220	0.1452	-0.4833	0.5046	-10.5	180	150	3	35	45	-72
4085002	2.4660	1.6920	2.9907	220	0.2236	-0.4743	0.5244	8.5	329	142	3	34	45	-64
4086015	1.3040	1.0340	1.6642	110	0.1758	-0.0676	0.1883	2.0	134	110	2	38	45	-20
4086016	1.3890	0.9290	1.6710	110	0.2525	-0.1623	0.3002	2.8	112	121	2	34	45	-32
4086017	1.4440	0.8320	1.6665	110	0.3021	-0.2498	0.3920	3.5	117	200	2	30	45	-39
4087002	1.9050	2.5080	3.1495	220	0.2615	-0.2822	0.3847	10.5	22	40	4	53	45	-42
4087018	1.3370	0.8730	1.5968	110	0.2056	-0.2128	0.2959	3.4	28	64	3	33	45	-45
8005	1.2570	0.6370	1.4092	110	0.1335	-0.4256	0.4460	-5.0	15	120	4	27	45	-72
8009	1.6410	0.6470	1.7639	110	0.4797	-0.4166	0.6353	-3.3	20	270	4	22	45	-40

TABLE 5.3

<ξξO> OUT OF PLANE TRANSVERSE PHONONS

Run No.	Q_x	Q_y	Zone	q_x	q_y	E	S	B	R	A1	A2	A3
4061002	2.298	2.549	112	0.466	-0.081	14.3	53	159	4	48	59	-7
4061003	2.190	2.630	112	0.398	-0.020	15.0	64	215	4	50	59	-1
4061004	1.863	1.342	111	0.189	0.011	1.5	127	173	1	36	40	3
4061020	0.582	1.261	001	0.371	-0.050	2.4	80	368	4	65	90	-6
4061021	0.538	1.185	001	0.343	-0.108	2.0	93	390	3	66	90	-14
4061022	0.639	2.810	002	0.408	0.116	25.4	75	390	4	77	90	14
4061023	0.788	2.744	112	-0.497	0.066	25.9	78	357	3	74	59	-5
4061024	0.896	2.621	112	-0.428	-0.026	25.3	86	345	3	71	59	3
4062009	3.153	2.658	222	0.012	0.002	32.6	93	98	2	40	40	6
4062013	1.949	1.366	111	0.244	0.029	8.9	50	152	4	35	40	6
4062013	2.400	2.630	222	-0.468	-0.020	26.9	42	152	3	48	40	2
5030	1.253	3.999	113	-0.200	0.011	-14.8	388	340	4	73	69	-2

Table 5.4

Raman Frequencies (cm^{-1}) and Assignments

for Urea and Urea (d_4)

Assignments	C-M, A-G, L-W	Leier	G-B	
	$CO(NH_2)_2$	$CO(NH_2)_2$	$CO(NH_2)_2$	$CO(ND_2)_2$
A_1	58	144	135	-
B_1	58	59	58	56
E	102	102	104	100
E	135	134	137	133
E	177	177	175	167
(B_2)	0	0	0	0
(E)	0	0	0	0

Velocities of Sound

Propagation direction	Transverse direction	Value. $cm.sec^{-1}$
Longitudinal 2-axis	-	4.05×10^5
Longitudinal 3-axis	-	6.28×10^5
Transverse 3-axis	2-axis	2.18×10^5
Transverse 2-axis	1-axis	5.83×10^4

Table 5.5

Factor Group Analysis for Urea - Two Molecules per Unit Cell

D_{2d}^3	E	$2\delta_4$	C_2	$2C_2'$	$2\sigma_d$	n_i	T	T'	R'	n_i'	Raman	IR
A_1	1	1	1	1	1	7	-	1		6	R	-
A_2	1	1	1	-1	-1	4	-	-	1	3	-	-
B_1	1	-1	1	1	-1	4	-	-	1	3	R	-
B_2	1	-1	1	-1	1	7	1	-		6	R	IR
E	1	0	-2	0	0	13	1	1	2	9	R	IR

n_i total number of vibrations

T translations of unit cell (acoustic)

T' translations of unit cell (optic)

R' librational lattice modes

n_i' intramolecular modes

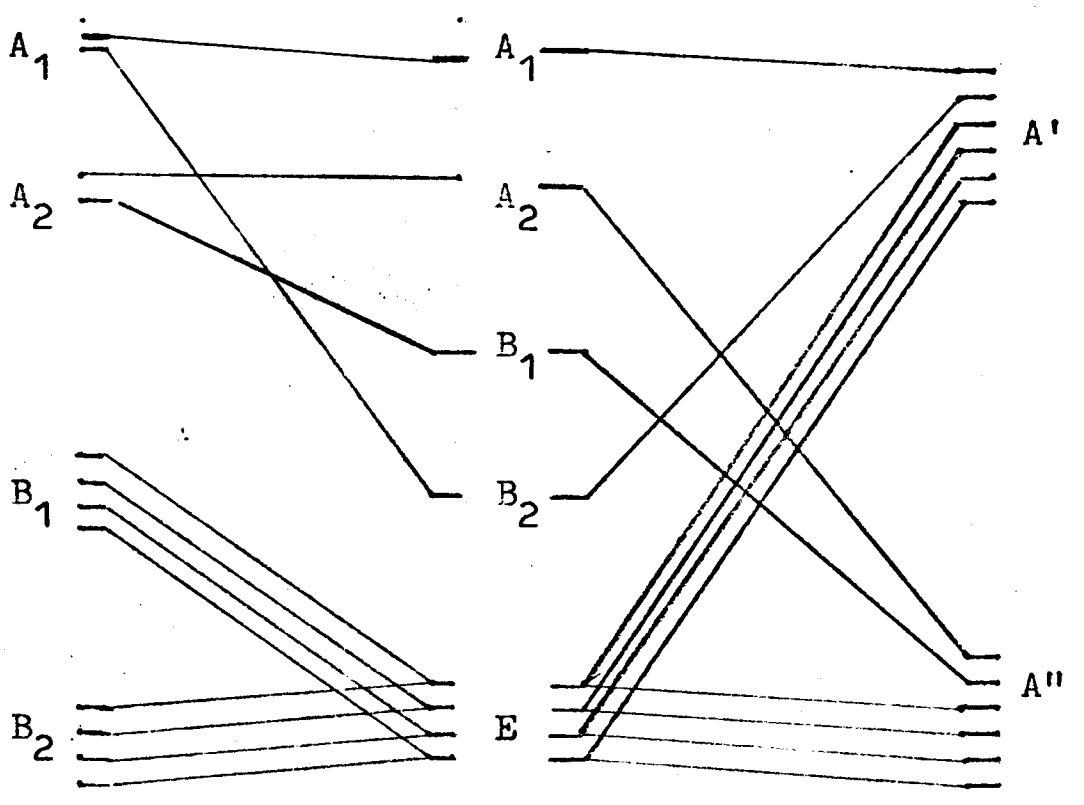
Intermolecular Modes

Translational	Librational
A_1	A_2
B_2	B_1
2 E	2 E

Table 5.6

Correlation Table for Lattice Vibration Normal Modes

q <001>	q=0	q <110>
$C_{2V}:K_{13}$	$D^3_{2d}:K_{17}$	$C_s:K_5$



at $\underline{q} = 0$, (including three zero acoustic modes) leaving only the A_2 mode undetermined. The factor group is isomorphous with the point group of $\underline{q}$, $G_o(\underline{q})$ when q equals zero and the analysis is given in table 5.5.

In general the space group transformations involve rotations and translations (combinations including screw axes and glide planes). Restriction of $\underline{q}$ to the first Brillouin zone enables the classification to be performed using the small group of rotations only. The non-symmorphic (non- centrosymmetric unit cells) space groups may be treated in this manner except when $\underline{q}$ lies on a Brillouin zone boundary, though even then the representation of $G_o(\underline{q})$ need not differ from the simple representation (Maradudin and Vosko, 1968).

The point group of the wavevector $G_o(\underline{q})$ along the <001> direction is C_{2V}, and C_s in the <110> mirror plane indicated in fig. 5.2 by the two sets of double lines, groups k_{13} and k_5 in Kovalevs system.

The correlation table 5.6 with each line representing one mode. With two molecules, in a general direction there are twelve non-degenerate branches to the dispersion relations.

5.3.1 <001> Direction

Longitudinal modes with both $\underline{Q}$ and $\underline{q}$ along the <001> direction transform in group C_{2V} only as class A_1. From the correlation table 5.6 only two modes should be seen, corresponding to both molecules in the unit cell translating in phase (acoustic, B_2), and out of phase (optic, A_1) when the classification in brackets indicates the zone centre classes. The observed points have been associated with the two curves i and 1 in figure 5.6. The A_2 modes are not observable. They correspond to in- and out-of-phase librations about the 3-axis (A_2, B_1)

at $\underline{q} = 0$, (including three zero acoustic modes) leaving only the A_2 mode undetermined. The factor group is isomorphous with the point group of $\underline{q}$, $G_o(\underline{q})$ when q equals zero and the analysis is given in table 5.5.

In general the space group transformations involve rotations and translations (combinations including screw axes and glide planes). Restriction of $\underline{q}$ to the first Brillouin zone enables the classification to be performed using the small group of rotations only. The non-symmorphic (non- centrosymmetric unit cells) space groups may be treated in this manner except when $\underline{q}$ lies on a Brillouin zone boundary, though even then the representation of $G_o(\underline{q})$ need not differ from the simple representation (Maradudin and Vosko, 1968).

The point group of the wavevector $G_o(\underline{q})$ along the <001> direction is C_{2V}, and C_s in the <110> mirror plane indicated in fig. 5.2 by the two sets of dquble lines, groups k_{13} and k_5 in Kovalevs system.

The correlation table 5.6 with each line representing one mode. With two molecules, in a general direction there are twelve non-degenerate branches to the dispersion relations.

5.3.1 <001> Direction

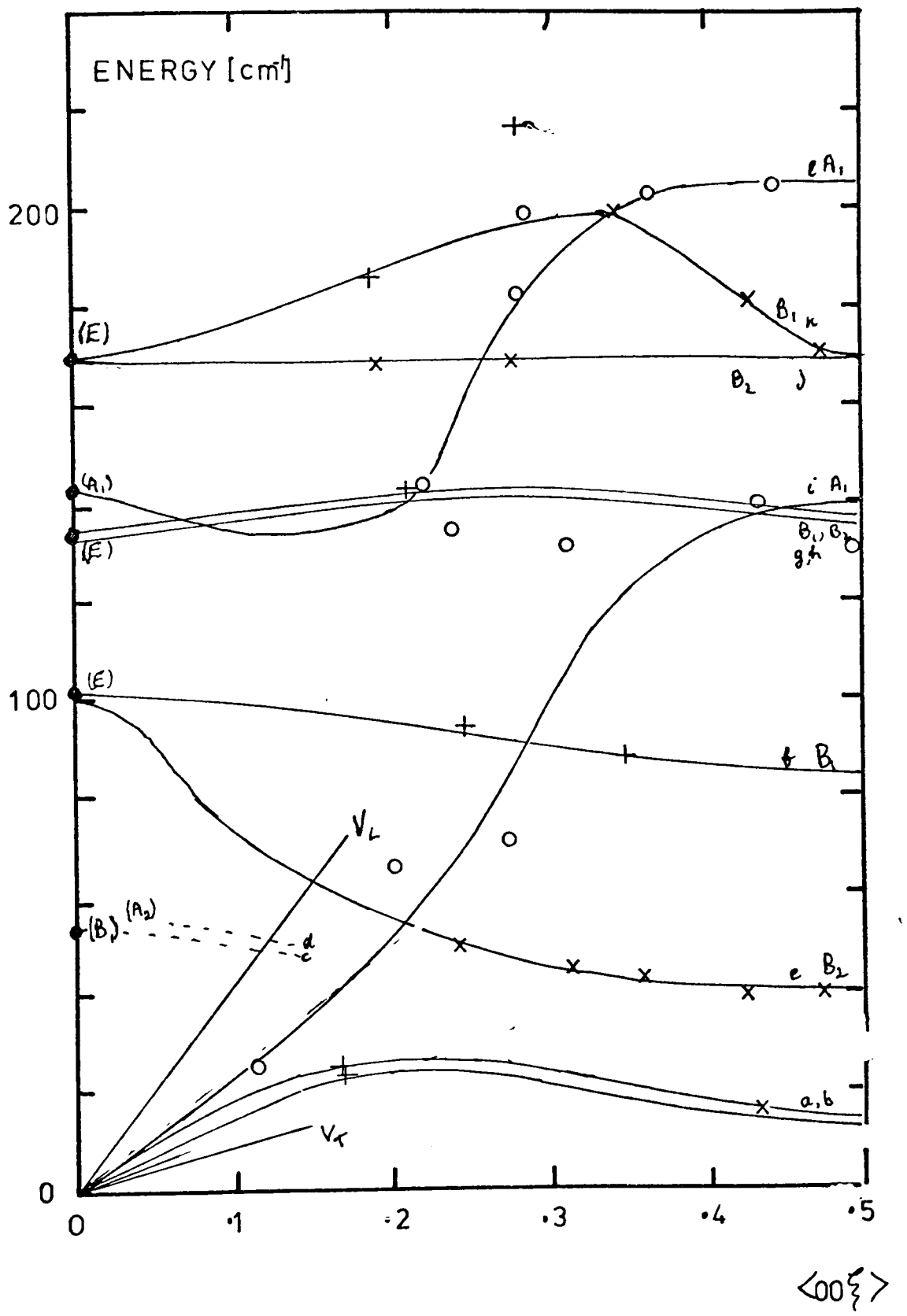
Longitudinal modes with both $\underline{Q}$ and $\underline{q}$ along the <001> direction transform in group C_{2V} only as class A_1. From the correlation table 5.6 only two modes should be seen, corresponding to both molecules in the unit cell translating in phase (acoustic, B_2), and out of phase (optic, A_1) when the classification in brackets indicates the zone centre classes. The observed points have been associated with the two curves i and l in figure 5.6. The A_2 modes are not observable. They correspond to in- and out-of-phase librations about the 3-axis (A_2,B_1)

UREA (d_4)

EXPERIMENTAL DISPERSION

CURVES

< 0 0 ξ >



longitudinal o

transverse × $B_1 + B_2$

\+ B_1 only.

fig. 5.6

which cannot interact with the longitudinal polarisation of the wavevector $\underline{Q}$, class A_1, despite any possible large displacement amplitudes.

The degeneracy of the zero wavevector transverse branches is lost when $\underline{q}$ is greater than zero, since the polarisation vectors have to satisfy the mirror plane operations of the group C_{2V}. The four (E) modes are each split to give one B_1 and one B_2 mode. When the <110> was in the scattering plane, only the B_1 modes can interact with the wavevector, the B_2 modes being orthogonal, but with the <100> in the scattering plane both may be excited. With insufficient data to distinguish the B_1 and B_2 modes, branches a,b and h,g are drawn assuming the splitting is negligible, correspondingly to isotropic propogation. The other points are constructed into branches from the remaining (E) zone centre modes.

The appropriate velocities of sound are indicated as a limiting slope for the acoustic modes as q tends to zero. A description of the type of motion represented by each branch is given in table 5.7 assuming that there is no mixing of translation and libration of the molecules, though there are specifically no grounds for assuming this not to happen; and it seems favourable to have one molecule librating while the other in the unit cell translates: only detailed calculation would indicate the contributions to the displacement eigenvectors. The nature of the dispersion curves will be further discussed in the comparison with the density of states distributions in section 7.5.

5.3.2 <110> Direction

The only symmetry operation in C_s is reflection in the plane, modes being classed A' if not inverted and A" if inverted

Table 5.7

Modes (fig. 5.6)	Class	Type
a b	B_1 B_2	IOP translations normal to 001
c d	A_2	IOP libration about 001
e f	B_1 B_2	IOP libration normal to 001
g h	B_1 B_2	IOP libration normal to 001
i	A_1	IP translation along 001
j k	B_1 B_2	IOP libration normal to 001
l	A_1	OP translation along 001

Table 5.8

Modes (fig. 5.7)	Class	Type
a	A"	IP translations in basal plane
b c	A"	IOP libration about 001
d	A'	OP libration
e	A'	OP libration
f	A'	IP translation out of plane
g	A'	IP translation along 001
h	A'	OP translation along 001
i	A"	IP libration
j	A"	IP libration
k	A'	OP translation out of plane
l	A"	IP translation in plane

IOP in and out of phase

IP in phase

OP out of phase

UREA (d_4)

EXRERIMENTAL DISPERSION CURVES

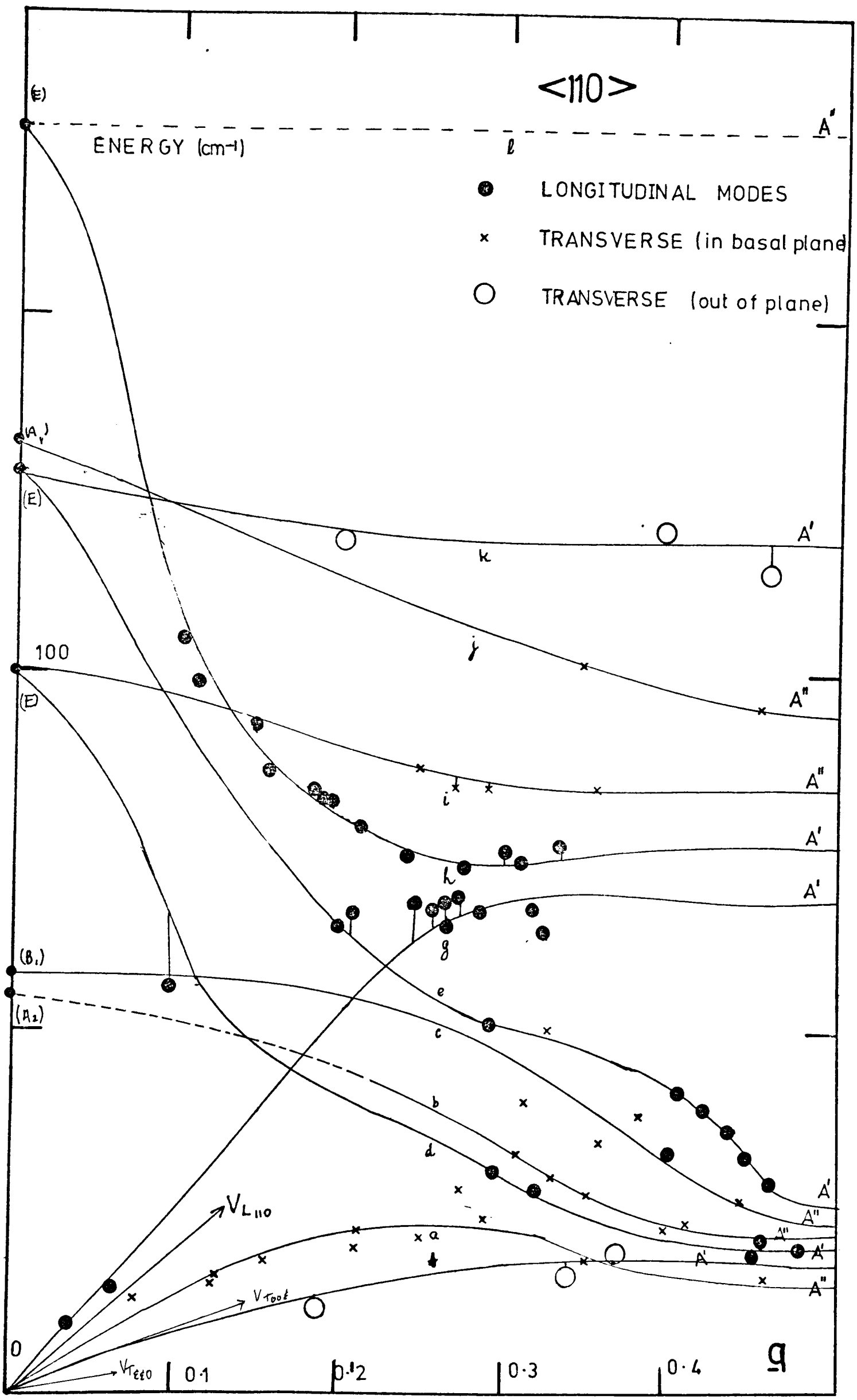


FIG. 5.7

by this operation. All longitudinal modes and also transverse modes where the polarisation is in the mirror plane are classed A'.

The velocity of sound is a guide in placing the longitudinal acoustic mode g from the (E) mode. Branch h is the associated antiphase translation of the two molecules along the <110> direction. Being of the same symmetry and nature the two branches do not cross and proceed parallel to the zone boundary. This leaves two other strongly dispersing longitudinal branches each originating from the remaining two (E) modes, and correspond to the librations of the two molecules. At the zone boundary it is necessary for the gradient to fall to zero to maintain the translational symmetry, and again repulsion of the two like modes is invoked to prevent them crossing.

The two modes, f and k, transverse to the basal plane originate from the (B_2) and (A_1) points. These groups were measured when the τ_{110} and τ_{001} were in the scattering plane. The transverse velocity of sound is also marked.

Distinction of the A" transverse modes is more difficult with the distribution of points, though many of the peaks observed are intense. To avoid unintentional selection of longitudinal modes only those peaks where $\underline{Q}$ lies along the 110 direction have been used. The acoustic mode (E) is first placed in the lowest set of points a. The other two transverse modes b and c would explain the high density of measured groups if they dropped from 58 cm^{-1}, and caused a repulsion of the acoustic mode a. Further evidence of there being a high number density of transverse modes at this part of the zone come from measurements on polycrystalline urea (d_4), section 7.4 . They correspond to the rotations of the two molecules about their 3-axis, and the in phase rotations about the other two axes (branches d and e)

which definitely show strong dispersion.

There are few points to place the two upper transverse branches. The positioning of branches will be discussed with the measured density of states spectra in section 7.5. A possible description of the modes is given in table 5.8.

5.4 Discussion of Coherent Scattering experiments

Additional information concerning the dynamics of urea is gained in incoherent studies described in chapter seven and conclusions from these coherent experiments will be presented in that section, comments here being restricted mainly to the generality of the techniques, and the accuracy of the measurements.

The specificity of triple axis measurements has an overwhelming advantage in refining measurements but, even after model calculations identification of observed branches in molecular systems is not necessarily straightforward (Pawley and Yeats, 1969a). The MARX-1 spectrometer used by Reynolds has shown its value in measuring very low energy modes: the highest frequency in β phase p-dichlorobenzene was 90 cm^{-1}. Using conventional triple axis formulism the resolution function is readily calculated and scans optimised.

This leaves the time of flight spectrometer with a sole advantage of covering a very large region in $(Q\omega)$ space and, unless used in a wasteful point by point fashion using one or possibly two counters, considerable analysis is required of the results. Because of the continuous nature of the branches observed (fig. 5.4) some degree of extrapolation is allowable in identifying weak peaks.

Figures 4.2 and 4.3 indicate that within the range of energies encountered in these experiments, the energy resolution

of between 5 and 10% has been adequate but the $\underline{Q}$ resolution is rather poor on both 7H and 4H5; the limit is in the wavelength spread in the incident beam set by both the type and number of rotors used. The only satisfactory combination is two multi-slotted rotors used at long wavelengths, as for example on 4H5. Despite the low resolution, certain branches, especially the longitudinal modes in the <110> direction are satisfactorily constructed from the results of a number of different experiments. The very strong dispersion of these longitudinal branches explains the difficulty found in using a triple-axis spectrometer with constant $\underline{Q}$ scans on another crystal of deutero-urea (B.M. Powell, private communication). Both crystal spectrometry and time of flight spectrometry would be difficult to use on crystals with real lattices very much greater than this crystal ($a = b = 5.66$ Å, $c = 4.73$ Å) because of the lack of resolution in $\underline{Q}$ when reduced to the first Brillouin zone.

CHAPTER 6

Scattering by Polycrystalline Solids and Experimental Methods

6. Scattering by Polycrystalline Solids

If a spectrometer is set to measure neutrons suffering an energy transfer $\hbar\omega$, and momentum transfer $\underline{Q}$, and a polycrystalline sample is introduced as a scatterer, the coherent scattering will come from the crystallites when the conservation requirements are fulfilled for a certain mode.

When $\underline{Q}$ is very large the assumption is made that the interference effects are reduced, especially where a large number of Brillouin zones is sampled by Q. Without the rapid variation with change of Q the cross-section resembles an incoherent cross-section and merely reflects the frequency distribution $G(\omega)$. At small $\underline{Q}$ values the averaging of transverse and longitudinal modes is very different (fig. 6.1). The former are observed when $Q \sim \tau$, whereas the longitudinal modes occur when $Q \sim \tau \pm q$. Egelstaff (1962) showed for a simple cubic Bravais lattice with three dispersion curves

$$S(Q,\omega) = S_s(Q\omega)_L \cdot Z_L \cos^2\theta_L + S_s(Q,\omega)_T \cdot Z_T(1-\cos^2\theta_T) \qquad 6.1$$

with

$$S_s(Q,\omega) = \frac{h}{2M} \cdot Q^2 \cdot e^{-2w} \cdot \frac{G(\omega)}{\omega \sinh(\hbar\omega/2kT)}$$

and

$$Z = \frac{\pi}{2Qq} \quad \frac{F(\tau)}{\tau}$$

with

$$\cos^2\theta_{LT} = \frac{\tau^2 - Q^2 - q^2}{2Qq_{LT}}$$

As shown in the fig. 6.1 as $|Q|$ is rotated about the reciprocal lattice sharp cuts-off are observed for the longitudinal mode when $Q = \tau \pm q$ but the transverse term varies as a sine wave peaked at $Q \sim \tau$. In simple systems measurement

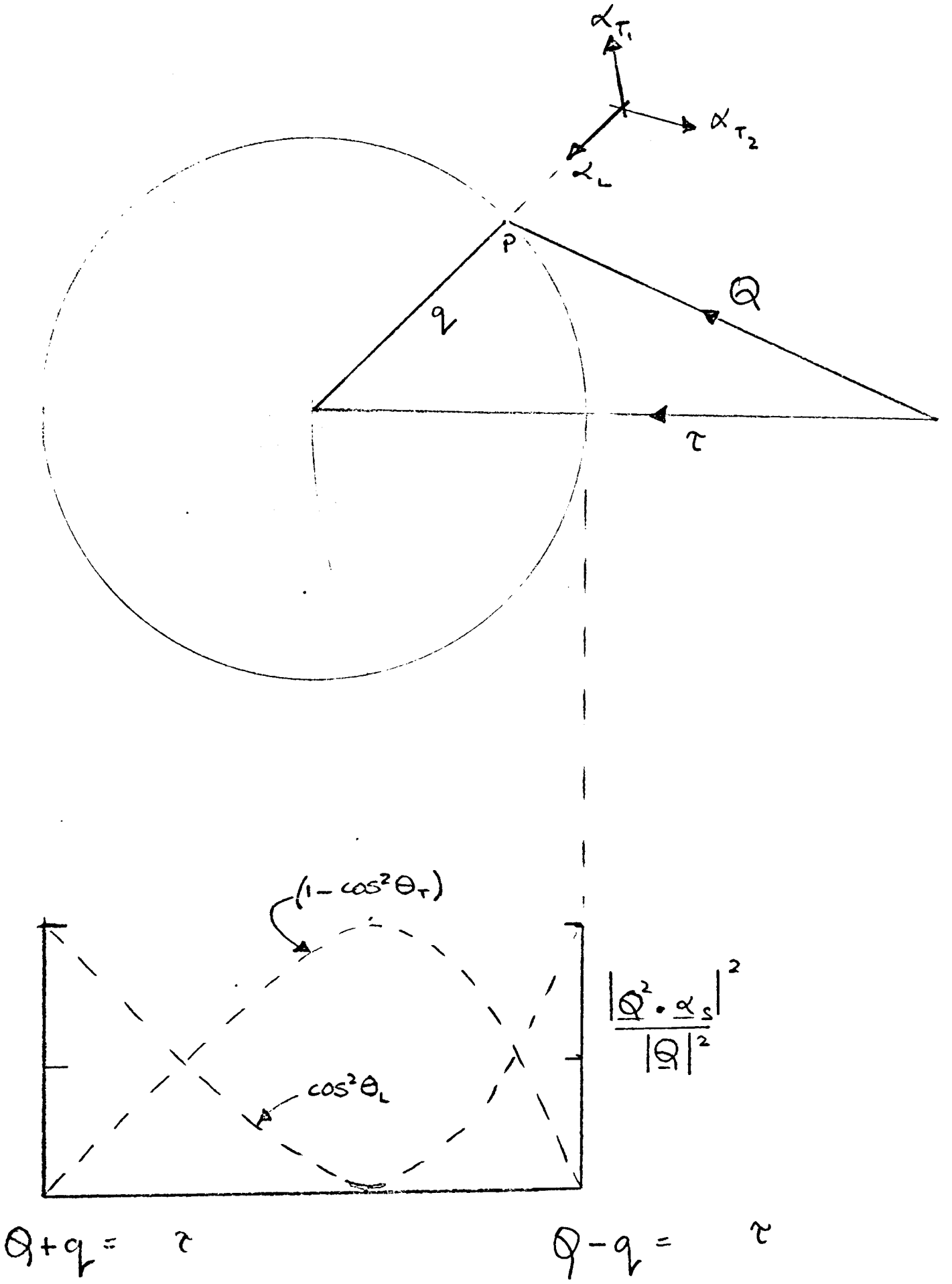

α_{T_1}
α_{T_2}
α_L
P
Q
q
τ
$(1-\cos^2\theta_T)$
$\cos^2\theta_L$
$\frac{|Q^2 \cdot \alpha_s|^2}{|Q|^2}$
$Q+q = \tau$
$Q-q = \tau$

Fig. 6·1

of the cut-off may be used to estimate the dispersion of the longitudinal modes, (Twisleton and White, 1972) using long wavelength neutrons: with shorter incident wavelengths many zones are sampled and the overlapping peaks are not resolvable.

Multiphonon scattering occurs when the conservation laws are satisfied by the sum of several processes.

$$k_1 - k_o + \Sigma \underline{Q}_i = 0, \quad E + \Sigma \hbar\omega_i = 0 \qquad 6.2$$

These conditions are less restrictive than for one phonon scattering and the spectrum is continuous, and with other cross-section factors equal the multiphonon contribution can be treated as incoherent scattering.

6.1 The Frequency Distribution.

The n phonon differential cross-section may be written in terms of n^{th} convolution of $f(\omega)$

$$f(\omega) = \frac{n<|\underline{Q}.\underline{U}|>^2}{\hbar\omega(1-e^{-\hbar\omega/kT})} \; G(\omega)$$

$$fn(\omega) = \int_{-\infty}^{\infty} G_1(\omega_1)d\omega_1 \int \cdots \int G_n(\omega_n)\, d\omega_n \qquad 6.3$$

and the corresponding cross-section is

$$\frac{d^2\sigma}{d\Omega dE} = \sum_n \frac{d^2\sigma_n}{d\Omega dE} = \sum_n \frac{k_1}{k_o} 3nNb^2 \exp(-2W)(|\underline{Q}.\underline{U}|^2)^n \frac{fn(\omega)}{n!} \qquad 6.4$$

Because of the large incoherent cross-section, low mass, and position on the outsides of molecules, hydrogen atoms in molecular solids usually have large vibration amplitudes and dominate the incoherent spectrum and it is only necessary to sum the expression 3.1 over the hydrogen nuclei. Thus the elastic scattering, given by the zero phonon cross-section is

$$\frac{d\sigma}{d\Omega dE} = \sum_i b^2_i \exp(-2w^o_i)\,\delta\varepsilon \qquad 6.5$$

and

$$w^o_i = \frac{1}{4M_{HL}} \sum_j \frac{h(Q.U^H(ij))^2}{w^2_j} \coth \hbar\omega/2kT$$

The one phonon cross-section is:

$$\frac{d\sigma}{d\Omega dE} = \frac{k}{k_o} \frac{|Q^2|}{4M\,w} \sum_j b^2_{inc} \frac{\exp -2W^1}{(\exp(\hbar\omega/kT)-1)} G^{inc}(\omega) \qquad 6.6$$

where

$$G^{inc}(\omega) = \frac{M}{M_H} \frac{a}{2\pi} \sum_j \frac{1}{\omega} \int dq \left|U^H_j(q)\right|^2 \delta(\omega-\omega_j(q))$$

where M is the mass of one unit cell. $G^{inc}(\omega)$ is $G(\omega)$ multiplied by the square of the normal mode displacement vector $U_j(q)$. Then approximation assumes that the average overall orientations can be written as the product of the averages of the Debye Waller factor and the weighting in $G^{inc}(\omega)$. More rigorous treatment involves the average to be performed for each mode separately as in (3.3). Thus the resultant inelastic Debye Waller factor derived experimentally is not a direct measure of the proton amplitude in mode j (Longster and White 1969).

From the observed differential cross-section, by dividing by Q^2 and extrapolating this function to $Q^2 = 0$ elimination of multiphonon terms in $[Q^2]^n$ occurs leaving the one phonon frequency distribution as the intercept value. Because of the translational symmetry in crystals the dispersion surfaces cut the Brillouin zone boundary with a zero group velocity, $d\omega/dQ = 0$: consequently singularities are always present in the frequency distribution (van Hove, 1954) and hence edges in the incoherent spectrum; though the widths and shapes depend on the nature of the surface, only the intensity is dependent on $|Q|$. As described in section 6 the incoherent spectrum may be modified

with extra singularities from the coherent scattering by the longitudinal modes but these show dispersion at different $|\alpha|$ values. An additional advantage of the extrapolation procedure to obtain the frequency distribution is that averaging is performed eliminating most of these coherent effects. Even in the case of the purely coherent scatterer graphite, Page (1968) was able to obtain frequency spectra, a refinement being the iterative recalculation of the spectrum by the methods of Egelstaff and Schofield (1962) incorporated in the program LEAP (McLatchie, R.C.F. unpublished). In a polynuclear coherent scatterer the magnitude of the mass-weighted amplitude of vibration is also an intensity determining factor.

An analogous extrapolation may be used to obtain the frequency distribution $\rho(\beta)$ in dimensionless units; this function being the same for systems with similar dynamical situations and ratios of actual temperature to Debye temperature, with different mass scatterers.

$$\rho(\beta) = 2\beta \sinh(\beta/2) \underset{\alpha \to 0}{Lt} \frac{S(\alpha\beta)}{\alpha}$$

and

$$\rho(\beta) = \frac{kT}{\hbar} G(\omega)$$

$\rho(\beta)$ is temperature dependent. Defining this velocity autocorrelation function. Egelstaff and Schofield showed it could be related as above to the scattering law without having to perform the fourier transform.

6.2 Relationship between the Frequency Distribution and Optical Measurements

Gordon (1965) considers optical spectra in terms of the Heisenberg representation which, as in equation 1.29 focusses the attention on the time development of the system rather than

its quantum states. This leads to consideration of the spectrum as the fourier transform of an appropriate time correlation function. In the case of infra-red spectra, the intensity $I(\omega)$ is a function of the transition dipole moment associated with the displacements of electrons in bonds: for the mode j.

$$I(\omega) = \frac{1}{2\pi}\int_{-\infty}^{\infty} \exp(-i\omega t) \langle \underline{e}.m_j(0).\underline{e}.m_j(t)_T\rangle dt$$

where $\underline{e}$ is the unit electric field vector of the incident radiation. For an isotropic solid or liquid

$$I(\omega) = \frac{1}{2\pi}\int_{-\infty}^{\infty} \exp(-i\omega t) \langle m_j(0).m_j(t)\rangle_T dt$$

For incoherent neutron scattering

$$G(\omega) = \frac{2M}{\pi KT}\cdot\int_{0}^{\infty} dt\ \cos\omega t\ \mathrm{Re}[\tfrac{1}{3}\langle v(0).v(t)\rangle]$$

and the frequency distribution of the nuclear velocity-velocity (or for a harmonic oscillator - displacement - displacement) correlation is the same as $I(\omega)$ for the optically active modes.

6.3 Experimental Methods

Because only knowledge of the magnitude of Q is required in the determination of $S(Q,\omega)$ for polycrystals or liquids advantage may be taken to increase the counter area; for any one scatter angle the counters may lie on a cone about the beam axis. For this reason conventional triple-axis spectrometry is rarely used in these studies and time-of-flight spectrometers with multiple detector arrays enable data to be acquired rapidly.

Both the time of flight spectrometers used in this work (the cold neutron spectrometer (4H5), and the long wavelength spectrometer (6H) on DIDO reactor) have rotor systems designed

to produce long wavelength monochromatic pulsed neutron beams and experiments usually involved neutron energy gain from the sample. Because of the small thermal populations in samples at energies greater than 4kT, and the low resolution fig. (4.2) experiments are limited to the investigation of low energy motions at accessible temperatures.

These spectra may be complemented by the use of a variable crystal monochromator to select high energy neutrons, and to analyse the scattered neutrons using a cooled polycrystalline beryllium block between sample and detectors. This acts as a low energy (< 40 cm^{-1}) neutron pass-filter. The differential cross-section is measured by changing the incident energy and recording the relative flux of neutrons which have lost sufficient energy to be beyond the Bragg cut-off for the poly-crystalline filter (3.96 Å, 42 cm^{-1}). This type of detector has a larger acceptance angle (15°) than the conventional triple-axis analyser giving much greater count rates.

6.4 The Cold Neutron Spectrometer 4H5, and Long Wavelength Spectrometer 6H.

The usual counter bank used with the twin rotor mono-chromator is an extended array of 2 atmosphere, 1" diameter BF_3 detectors covering 13 scattering angles between 13° and 90°, fig. 4.1. The flight path varies between 1.8 m at 13° and 1.3 m at 90° being restricted by the floor level. Harris et al (1961) describe the spectrometer with a smaller detector box. The most usual operating wavelength is 4.8 Å which is the peak in the cold neutron flux, though usable flux is available up to 10 Å, the limit set by the rotor drive system. With the continuous nature of the spectra and the shorter flight paths the problem of frame overlap is reduced. Counts

from the detectors at the same scatter angle are collected together, encoded, and then sent to the CASSANDRA computer system for accumulation and final recording onto DEC tape.

The 6H spectrometer fig. 6.2 (Bunce, Harris, and Stirling 1970) offers a similar scope for experiments as 4H5, though lacking a cold source incident wavelengths greater than 6 Å are rarely used because of the low flux. All sample to detector distances are 1.2 m at nine angles (18° - 90°), and though there is a loss in $|Q|$ resolution a large solid angle is subtended by the counters at the sample. Again the output from the detectors is collected and encoded before being time analysed and stored by CASSANDRA. Sample preparation and mounting and data handling and reduction are similar for the two instruments.

6.5 Sample Preparation and Mounting

The beam size is 5 cm x 2.5 cms vertical. Samples are usually placed as a uniform thin layer at 45° to the beam and over an area of 7 x 5 cms. All samples used were of A.R. grade and dried thoroughly before use. The quantities required to scatter 8% of the incident beam were calculated, then mounted between aluminium foils of 0.25 and 0.05 mm thickness which has an exceptionally small cross-section. The specimen is attached to a sample changer which is used to cycle three samples sequentially into the beam for chosen periods controlled by CASSANDRA. In one sample position is mounted a 1 mm thick vanadium plate for calibration; the third may hold a comparison specimen or an empty can. The periodic cycling allows for instrumental fluctuations (the BF_3 counters not having the very high stability of the scintillators) as well as background effects since intensity measurements as well as peak positions

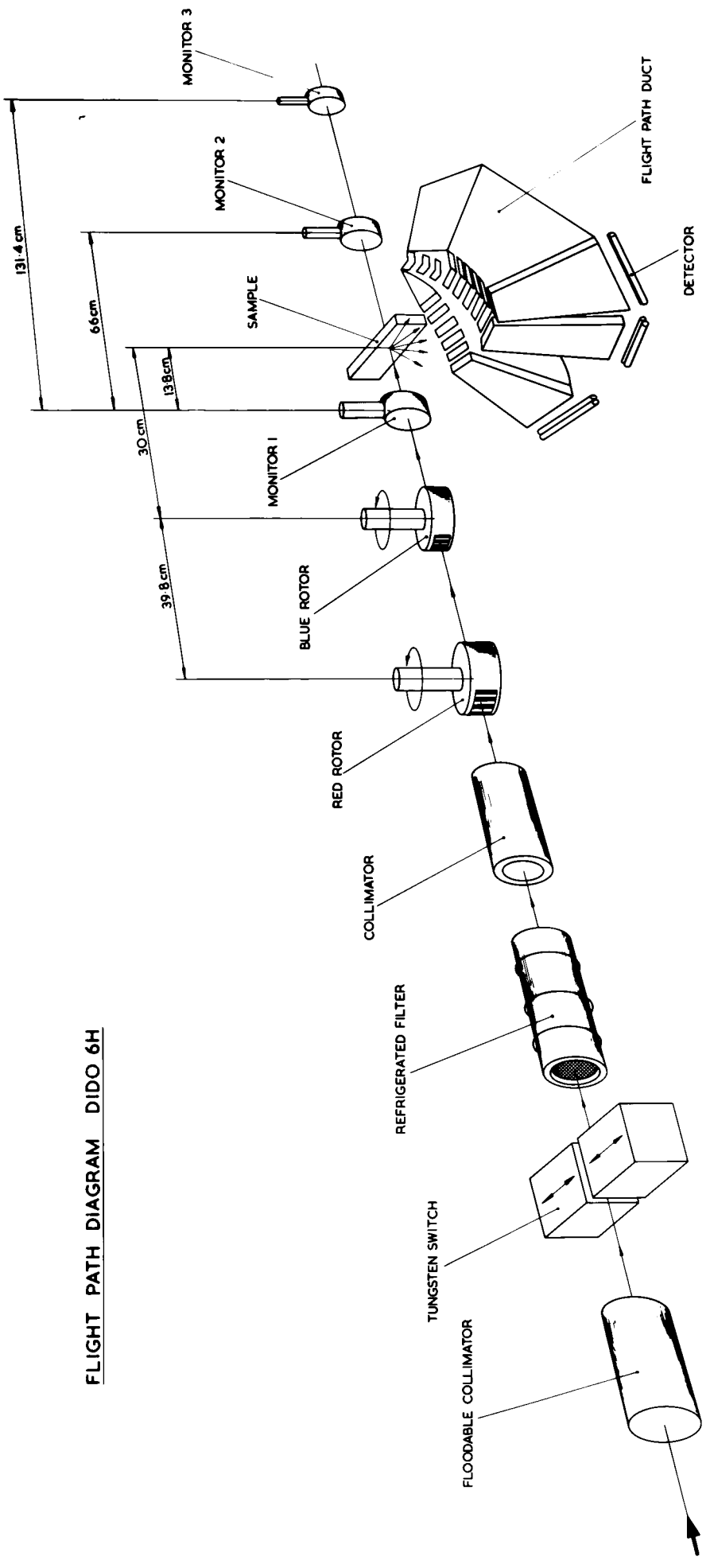

FLIGHT PATH DIAGRAM DIDO 6H
MONITOR 3
MONITOR 2
SAMPLE
MONITOR 1
BLUE ROTOR
RED ROTOR
COLLIMATOR
REFRIGERATED FILTER
TUNGSTEN SWITCH
FLOODABLE COLLIMATOR
FLIGHT PATH DUCT
DETECTOR
131.4 cm
66 cm
138 cm
30 cm
39.8 cm

fig. 6_2

are required. The changer is mounted in an evacuable tube (or helium gas may be used for flushing out the unwanted air), with thin aluminium windows to transmit incident and scattered neutrons. Facilities exist on both 4H5 and 6H for heating (electrically) or cooling (liquid nitrogen loop) the sample mounting block. Control is effected by microswitches on a servo-pen recorder connected to thermocouples on the sample block. Fig. 6.3 shows the 4H5 sample changer with the empty sample block and vanadium standard. It is necessary to vacuum insulate when cooling to prevent condensation on the thin windows.

6.6 Data Reduction

The incident velocity and counter distances are derived as in section 4.6 . Intensities are normalised using the integrated vanadium elastic peak counts, and corrections are made for counter efficiency (a function of neutron energy), background, and absorption, by the program CIRCA (Cocking, Wignall 1967). The corrected data is finally plotted as the differential cross-section $\frac{d^2\sigma}{d\Omega d\tau}$ where τ is the time of flight of the scattered neutron in microseconds per metre.

$$\frac{d^2\sigma}{d\Omega d\tau} = \frac{\sigma_b}{4\pi} \cdot \frac{e\tau_o}{e_\tau} \cdot \frac{A_1(C_s-B_s)}{V_s} - \frac{A_2(C_B-B_B)}{V_B} \cdot \frac{1}{\Delta\tau} \cdot \frac{1}{A_3} \cdot \frac{(N\sigma_b)_{vanadium}}{(N\sigma_b)_{sample}}$$

where e_τ, $e_{\tau o}$ are counter efficiencies at neutron reciprocal velocities τ and τ_o

$A_1 A_2 A_3$ are variables to allow for the different total irradiation times

C_s C_B sample counts, blank can counts

B_s B_B constant background counts for sample and blank

V_s V_B number of vanadium counts during sample and blank can runs.

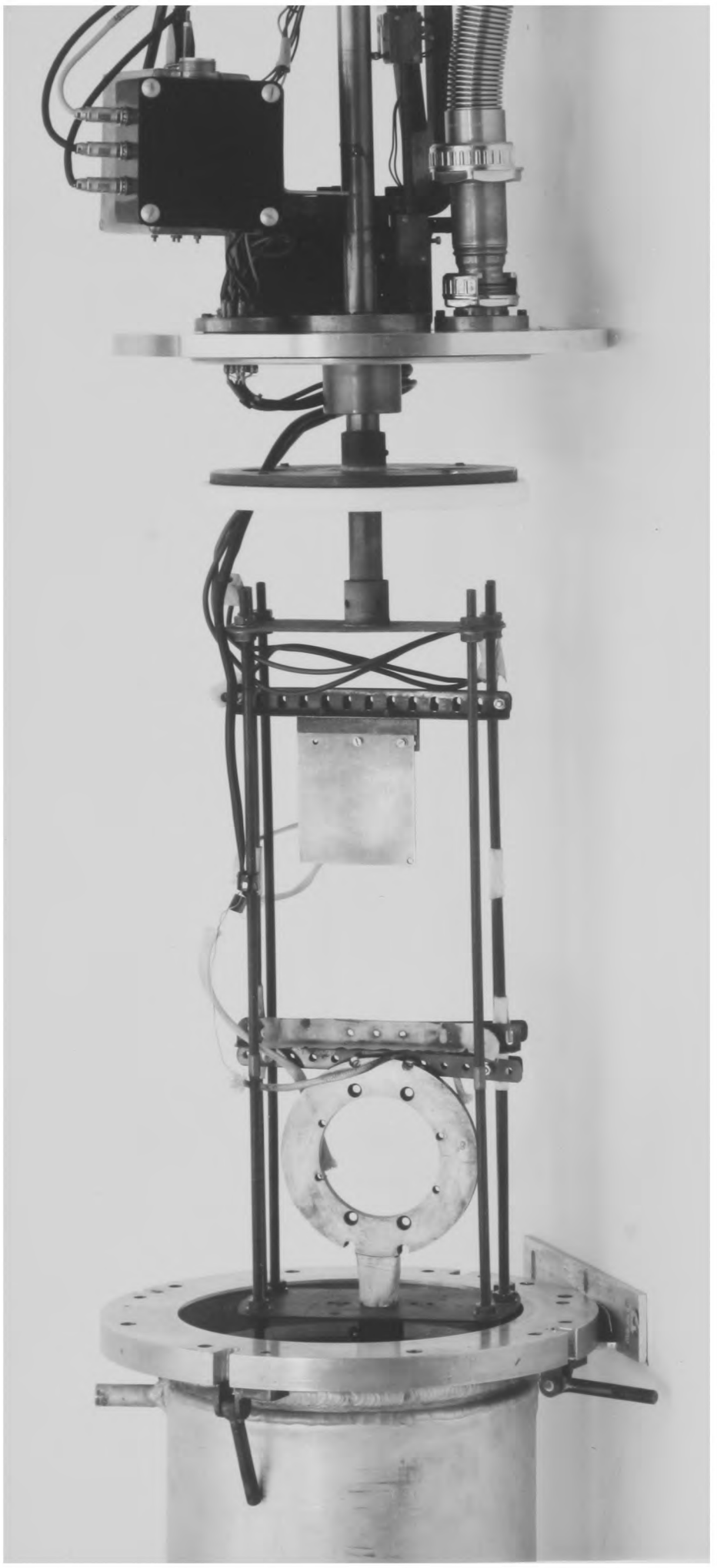


Fig. 6.3 The 4H5 Sample Changer

$$\frac{d^2\sigma}{d\Omega dE} = \frac{\tau^3}{m} \cdot \frac{d\sigma}{d\Omega d\tau}$$

and

$$S(\alpha\beta) = \frac{\tau^4}{m\tau_o} \cdot e^{\beta/2} \cdot kT \cdot \frac{4\pi}{\sigma_b} \cdot \frac{d^2\sigma}{d\Omega d\tau}$$

Measurements of peak positions should use the energy cross-section but this is heavily weighted at long times of flight and it is convenient to display the cross-section in terms of reciprocal velocity (wavelength) where as in the original raw data points are uniformly displayed. These calculations are performed for the spectrum at each angle, and facilities exist in the program for writing the spectral parameters onto magnetic tape or disk for subsequent processing. (Aldred, 1969, Ghosh, 1971).

The Frequency Distribution Function. A program FLORENCE was written (Ghosh 1971) to process further the cross-section data calculated in the CIRCA routine. The data from a number of counters is analysed into sets of $S(\alpha\beta)$ values at constant β, and the intercept of $\log_e S(\alpha\beta)/\alpha$ at $\alpha = 0$ obtained using a least squares straight line.

Three processes occur to cause the data points to deviate, apart from statistical error. Multiple scattering tends to peak in the forward direction (small α) and is always present in finite samples. Multiphonon scattering is a much smaller effect and is likely at high momentum transfers (equation 3.3). Both processes systematically yield a result higher than the normal one phonon process. The interference term $S_d(\alpha\beta)$ affects the intensity but not in a systematic fashion and to a first approximation is treated as statistical error. An iterative routine in the least-squares fit reduces the effects of the systematic deviation, results being judged by a facility to plot

out points and fitted lines. Ideally the frequency function could be used to calculate back the $S(\alpha\beta)$ and further refinement tried (Egelstaff and Schofield, 1962) but only the principal features, together with the averaging so performed is required in these studies. One problem inherent in the region of $(\alpha\beta)$ space experimentally available is the necessity to extrapolate over disproportionately smaller ranges of α as α and β increases. This renders the procedure unreliable for data in the region above 500 cm^{-1}.

6.7 The Beryllium Filter Detector

This detector utilises the monochromator drum and sample table of the PLUTO triple-axis spectrometer (fig. 6.4). In this mode of operation energy transfers from 200 to 1200 cm^{-1} may be studied though the resolution is limited at lower energies principally by the finite window of the detector ($\pm$ 20 cm^{-1}) and at higher energies by the monochromator collimation in addition. The upper energy limit is set by the thermal flux distribution of the reactor.

Monochromator table and main-arm angle settings have been calculated to enable the instrument to step sequentially at 10 cm^{-1} energy intervals, controlled by paper tape. Equal angle increments results in many points being measured at low energy transfers and few at the higher energy end. A fission chamber monitor in the incident beam limits the counting after a set flux has passed (though this monitor shows the usual $(\text{energy})^{-\frac{1}{2}}$ efficiency relationship).

Measuring an energy loss process samples may be cooled to reduce effects of anharmonicity and sharpen peaks. Calibration and background measurements with a vanadium standard are not possible since appreciable excitation occurs; the backgrounds

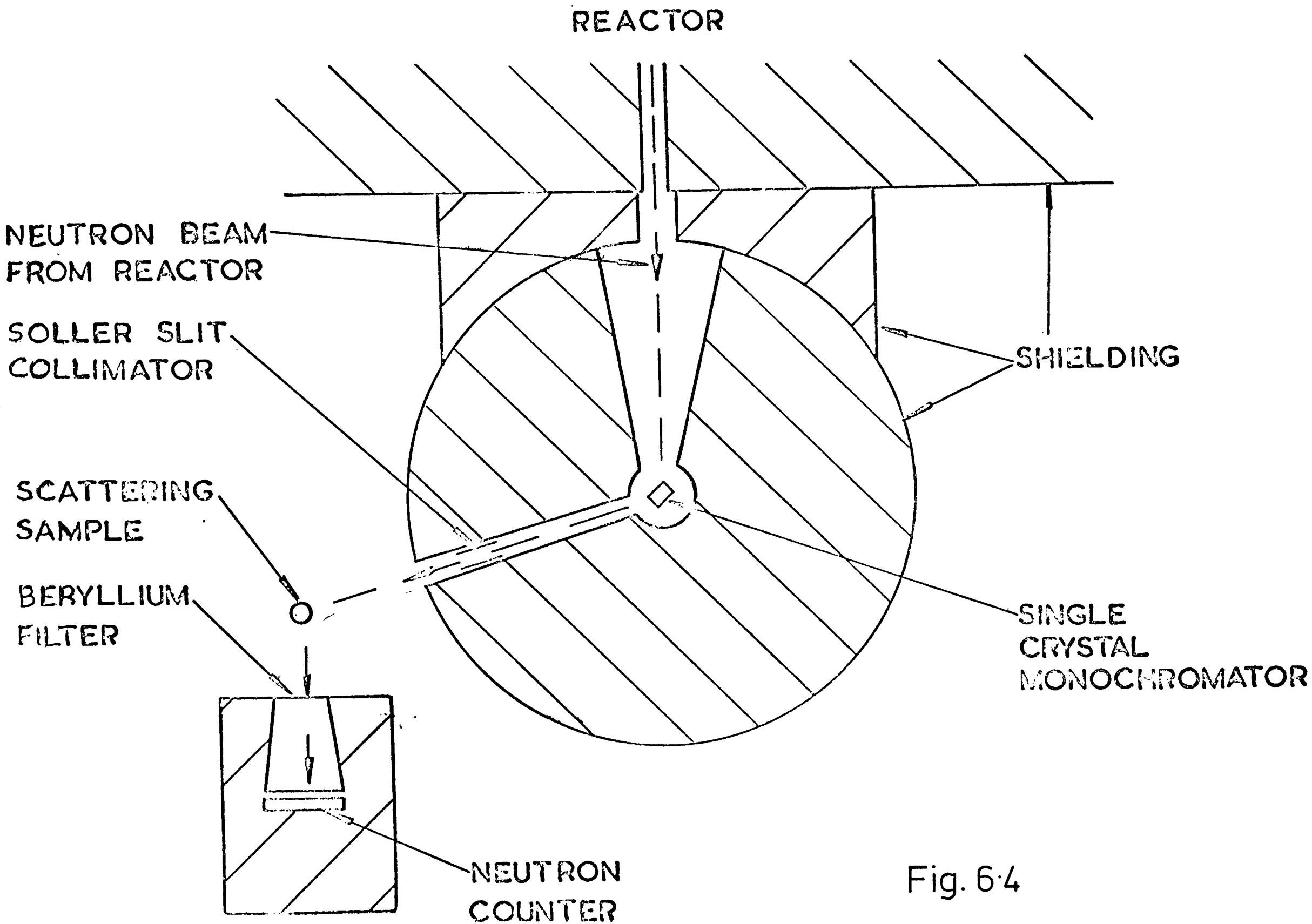

REACTOR
NEUTRON BEAM FROM REACTOR
SOLLER SLIT COLLIMATOR
SCATTERING SAMPLE
BERYLLIUM FILTER
SHIELDING
SINGLE CRYSTAL MONOCHROMATOR
NEUTRON COUNTER

Fig. 6·4

too are sample dependent and also vary with the position of the sample table and detector, being high when these are close to the reactor walls. In view of the rather qualitative results obtained, multiple scattering is ignored and samples scattering up to 20% of the beam are used.

Use of high order planes (311, 511, 711) eliminates the possibility of order contamination, and allows high monochromator take-off angles, optimising the resolution at the expense of flux. Because the energy spread dE content of the monochromated beam varies with the monochromator angle θ, this geometrical factor of $\cot\theta/\sin^2\theta$ has been used to correct the observed results in a simple approximation.

CHAPTER 7

Measurement of Intermolecular Modes from Polycrystals

7. Measurement of intermolecular modes from polycrystals

The inelastic scattering spectra from hexamine and naphthalene are compared with model results. Results of experiments on urea, thiourea and oxamide are compared with these as a basis for interpretation of the dynamics of the lattice modes.

7.1 Hexamethylenetetramine (HMT)

The spectrum of $C_6H_{12}N_4$ has been measured at 295K at nine scatter angles on 6H. The scattering is predominantly incoherent and the lattice modes readily distinguished from the lowest internal mode at 320 cm^{-1}. The experimentally derived $G^{inc}(\omega)$ is shown in figure 7.1. The resolution has been calculated following Roystons method (1962) and the deviations at three energies are indicated in figure 7.1.

In the Debye approximation $G(\omega)$ is proportional to ω^2 and the Debye temperature θ_D corresponds to the energy ω_D when

$$\int_0^{\omega_D} G(\omega)d\omega = 1. \quad , \quad \frac{\hbar\omega_D}{k} = \theta_D \qquad 7.1$$

At low energies where only the acoustic modes contribute to $G^{inc}(\omega)$ and these may be considered as being linear then $G^{inc}(\omega)$ should show a relationship similar to $G(\omega)$. Deviations occur with dispersion, and additional optic modes contributing to $G(\omega)$, so the energy at which this deviation becomes noticeable is a parameter related to the average over the dispersion surfaces. This has been measured together with the Debye temperature and is given in Table 7.1.

HEXAMINE

DENSITY OF STATES

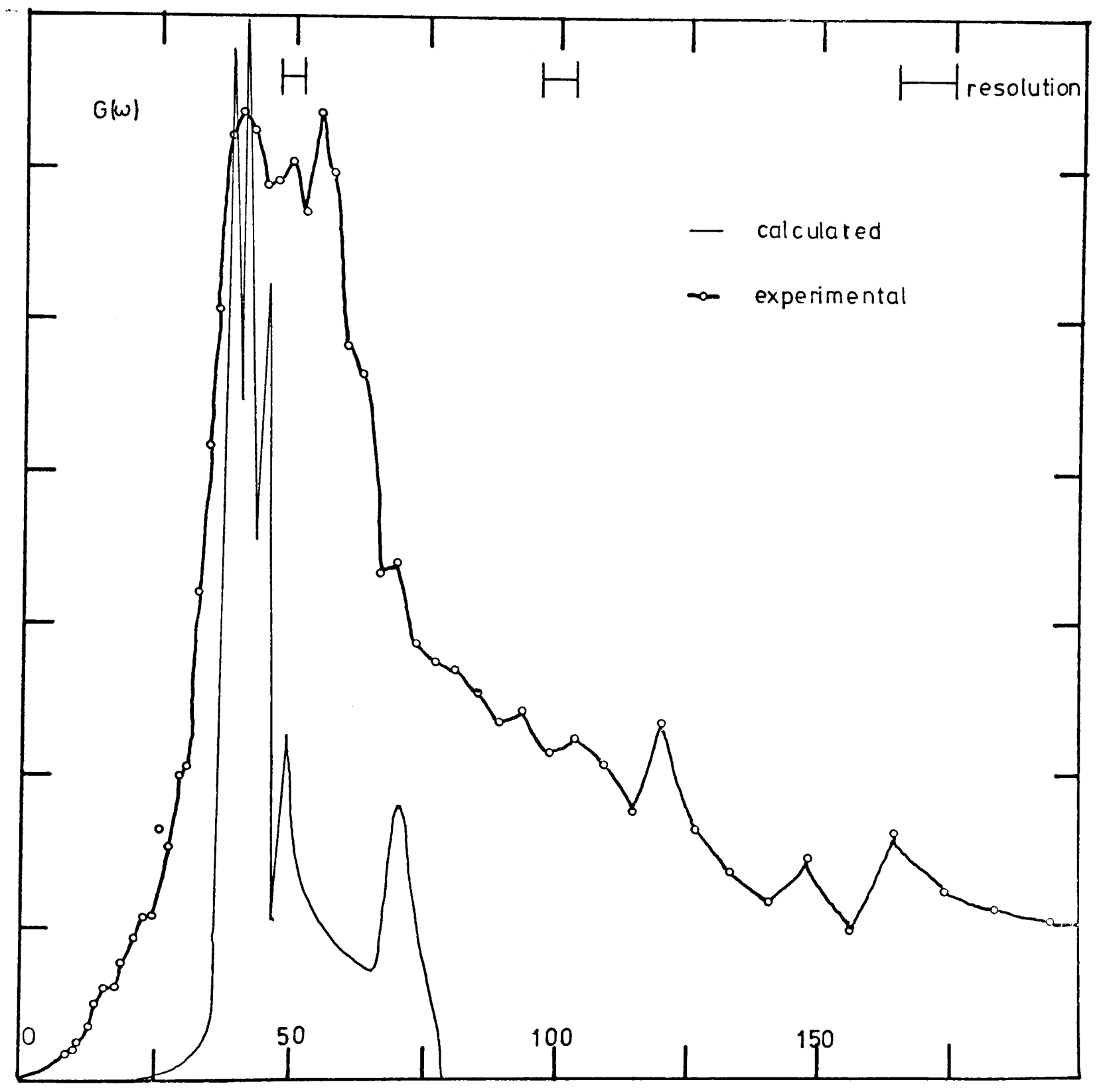


Fig. 7·1

Table 7.1

Results for Incoherent Scattering from Hexamine 298 K

Peaks observed in experimental $G^{inc}(\omega)$	Infra-red Measurements (Cheutin and Mathieu, 1956)
Lattice Modes	
cm^{-1}	cm^{-1}
40	40
48	
54	
Internal Modes	
335	320 ν_6
410 (sh)	-
477	465 ν_3

Experimental Debye temperature 138 K

Deviation from simple Debye behaviour 33 cm^{-1}

Extra detail is revealed in the librational peak in $G^{inc}(\omega)$ not resolved in the single counter experiment of Becka (1962), three characteristic peaks being resolved in the libration band at 40 cm^{-1}.

HMT crystallises in the cubic space group $I\bar{4}3m$ with cell edges a = 7.021 Å. This highly symmetrical molecule is of a globular nature, explaining the ready packing into the body-centred cubic lattice, and has been subject to a number of structure refinements, (Becka and Cruickshank 1963, Duckworth Willis and Pawley 1969), where attempts have been made to fit simple models to improve the structural fit. The lowest internal mode frequency is at 320 cm^{-1}. The melting point is 536 K, and there is no evidence from n.m.r. measurements of any free rotation at room temperatures, an estimate of a barrier of 18 kcals $mole^{-1}$ (equal to the enthalpy of sublimation) being set at a linewidth transition at 375°K by Smith, (1962), the entropy of fusion being correspondingly small. With such a

large separation between the internal and external modes, the molecule was treated as a simple rigid body to explain the thermal motions, the r.m.s. librations and translations being 6.57° and 0.165 Å from the room temperature X-ray measurements.

Hexamine was treated as centro-symmetric by Cochran and Pawley (1964) when making the first detailed calculation of the lattice dynamics of a molecular solid (independently to Hahn and Beim, 1963) and compared results with X-ray thermal diffuse scattering. Refinement of the model followed the measurement of the dispersion relations in a single crystal of deuterated HMT (Powell, 1968), using a triple axis neutron spectrometer.

The frequency distribution calculated for DHMT by Powell scaled appropriately for the hydrogenous material is shown on the experimental frequency distribution. The characteristic three librational peaks are resolved, but only a calculation of $G^{inc}(\omega)$ would test the model well. A very simple model of Rafizadeh and Yip (1970) using an extended point mass to represent the rigid molecule also fits the measured dispersion curves well, but showing no detailed comparison with $G^{inc}(\omega)$; this suggests that calculation of $G^{inc}(\omega)$ would be a more sensitive model test since the eigenvectors as well as eigenvalues must be calculated correctly.

With such a large spherical molecule the contributions from the libration amplitudes do not dominate the translational modes, because of the large moment of inertia, and high torsional barrier. The Debye temperature (Becka and Cruickshank, 1963) has been estimated at 116 K at 298°K, and the acoustic branches measured by Powell deviate from being linear at about 26 cm^{-1}. Little dispersion is shown by the librational modes, all being within a 13 cm^{-1} band along symmetry directions though few of

these points were reliably measured in this triple axis experiment, because of the unfavourable structure factors.

7.2 Naphthalene

The incoherent scattering spectra from $C_{10}H_8$ were measured on the 6H spectrometer at 295 K and 150 K. The data were corrected and then in each case the frequency distribution $\rho(\beta)$ obtained using the program FLORENCE. No coherent effects could be detected in either the time-of-flight spectra or the extrapolations. The final density of states spectra are shown in figure 7.2. Since $\rho(\beta)$ is proportional to the absolute temperature the ratio of the areas should be 1:0.508. The observed ratio (assessed by planimeter) is 1:0.511. At such low energies no modes have been lost completely and the good agreement of these ratios is indicative of the lack of coherent scattering which often affects the normalisation procedure. This may use sample total transmission or total scattering in comparison with the standard vanadium sample. Where strong Bragg scattering occurs from the polycrystals it is necessary to assess the incoherent scattering in low angle counters when the momentum transfer is too small for direct coherent effects, though multiple Bragg scattering peaks strongly in the forward direction and may cause complications with strong coherent scatterers.

Naphthalene crystallises in the space group $P2_1/a, (C_{2h}^5)$, with two molecules per unit cell. The structure has been determined using X-rays by Cruickshank (1957). At sufficiently high temperatures, Cruickshank (1956) analyses the square of the librational amplitude ϕ^2 in classical terms, being proportional to temperature when the temperature is greater than the Debye temperature.

$$\phi^2 = \frac{kT}{4\pi^2 I \nu^2} \qquad 7.2$$

NAPHTHALENE

DENSITY OF STATES $\rho(\beta)$

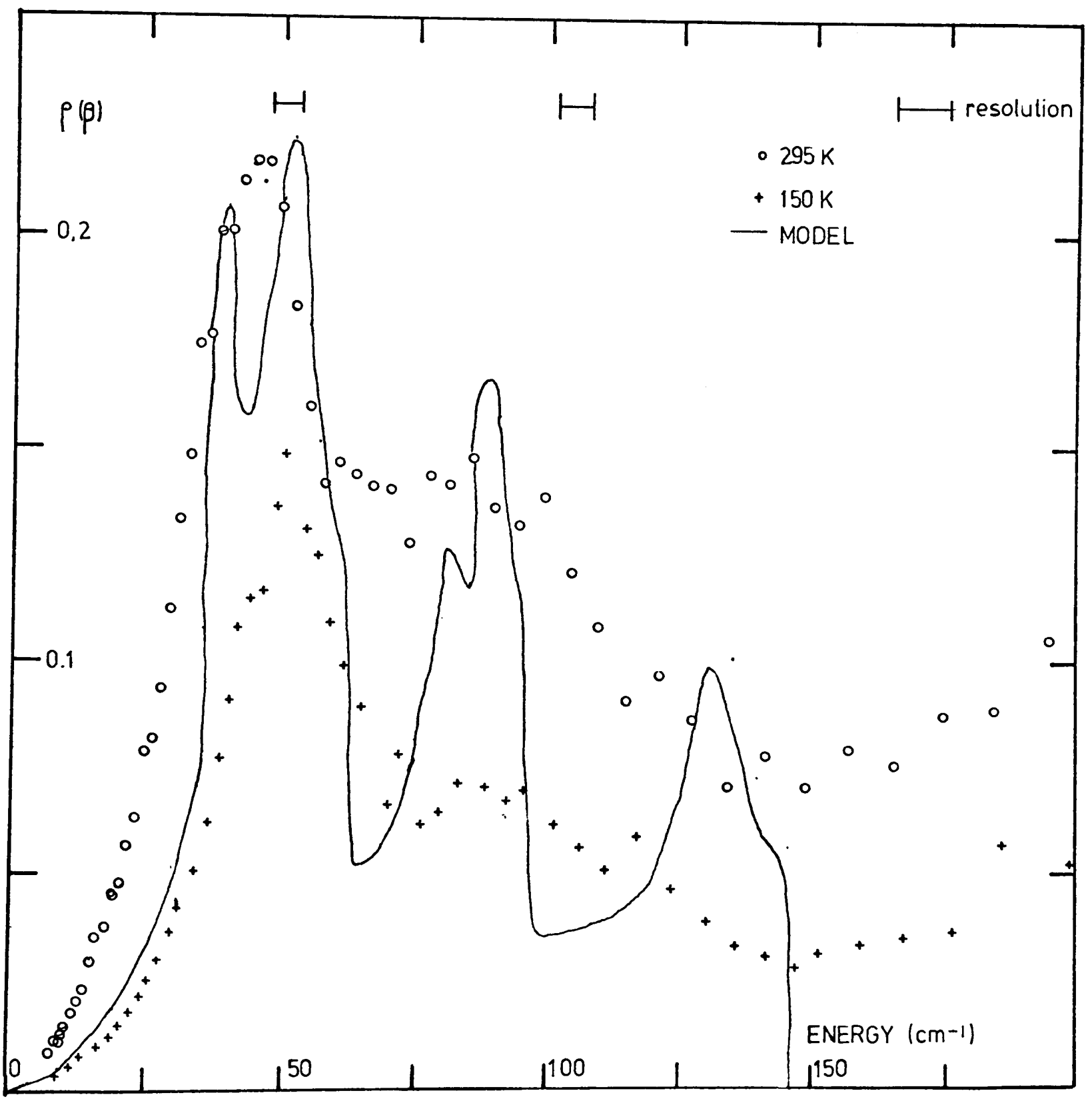


Fig. 7·2

where ν is the torsional frequency. Since the unit cell has a centre of symmetry the librational modes are Raman active, the optic translations being infra-red active. Measurements of the Raman spectrum at a number of temperatures enabled a value of ϕ^2 to be calculated for each of the principal axes in the molecule, assigning the bands to these librations (Ito, Suzuke and Yokoyama, 1968), and showing the close correlations between the X-ray data and those calculated amplitudes. The r.m.s. angular oscillations are 3.3°, 2.2° and 4.1° at room temperature. The corresponding root mean square displacement of a hydrogen furthest from the centre in a rigid system would be about 0.25 Å, compared with 0.2 Å for the mean molecular translation contribution, suggesting that there will not be marked differences in the two contributions to $G^{inc}(\omega)$.

The infra-red measurements of Hadni (1968) are in agreement with the observations and calculations of Harada and Shimanouchi (1967) who use hydrogen-hydrogen repulsions for the dominant intermolecular interaction.

Pawley (1967) used a 6-exp Buckingham potential between non-bonded atoms in a model calculation for the lattice dynamics of naphthalene, and derived the dispersion curves along the one axis of symmetry in addition to the zone centre modes. Eigenvectors of the displacements indicated that the librations of the antisymmetric modes were not about the principal axes of the molecule. Using the same model potential and method of setting up and diagonalising the dynamical matrix, Pawley, Reynolds, Kjems and White (1971) calculated $G(\omega)$ and the hydrogen amplitude weighted $G^{inc}(\omega)$ for naphthalene, and showed that the two had the same singularities.

Comparison of calculated $G^{inc}(\omega)$ with the dispersion curves

shows that since the rotational modes do not disperse greatly there is some similarity with the Raman optical data, however, with only one symmetry direction and a highly anisotropic crystal, further correlations are difficult. The principal test of the model is to compare the calculated $G^{inc}(\omega)$ with the experimental $G^{inc}_{exp}(\omega)$, where the calculated hydrogen displacement eigenvectors for all directions in the crystal are severely tested.

The model curve in figure 7.2 for $\rho(\beta)$ at 295 K is derived from the above calculation. There is some correlation between the measured and model curves though the experimental resolution is certainly adequate to distinguish the several features of the calculations. Deviations might be attributed to anharmonic effects (since the model is evaluated in the harmonic approximation) but this is unlikely since there is little change in the spectrum on cooling, though as in the optical measurements small frequency shifts are observed. A comparison of these spectra is given in table 7.2. The frequency distributions too are so well ratioed that the amplitude weighting is also a linear function of temperature, indicating harmonic behaviour.

The lowest intramolecular frequency is 200 cm^{-1} and deviations from rigid body behaviour are the probable cause of the deficiencies in the model. By repeating the calculation for all thirty six atoms in the unit cell, incorporating an internal force field of Cyvin's, Pawley and Cyvin (1970) derived the dispersion curves for the deformable molecules. The general effect was to lower the dispersion branches by between 4 and 8 cm^{-1}, but without any great change in their disposition. Increased dispersion in other directions in the reciprocal lattice could account for the rather featureless density of states which is observed but calculation of a $G^{inc}(\omega)$ solving the general

108 x 108 matrix hundreds of times is a prohibitive task. Ito infers from the optical data that the amplitude of oscillation about an axis normal to the plane of the molecule increases rapidly with temperature but no reorientation has been measured. In p-dichlorobenzene with a similar structure a nuclear magnetic resonance experiment (Buyle-Bodin, 1957) showed that reorientation was taking place, and the Raman lattice modes are also broadened at 300 K.

Table 7.2

Intermolecular Modes of $C_{10}H_8$

Peaks observed in Density of States			Optically Active Modes		
295 K	150 K	Model	290 K	77 K	Assignments
47	42	38	46	56	Bg
56	51	48	51	67	Ag
78	72	56	71	83	Bg
98	85	77	74	88	Ag
122	95	85	109	121	Ag
	116	128	125	141	Bg
				46	Au
				56	Bu
				89	

	295 K	150 K	Model
Experimental Debye temperature k.	128	113	78
Deviation from Debye behaviour cm^{-1}	39	33	30

7.3 Perdeutero-Naphthalene

Inelastic scattering experiments were performed on a sample of $C_{10}D_8$ at 295 K and 170 K. The results were treated in the same manner as for conventional incoherent scatterers. The specimen was obtained from Dr. G.S. Pawley, and diffraction measurements

indicated that there was 2% hydrogen present. The incoherent cross-section of $C_{10}D_8$ is very small since both carbon and deuterum have the same scattering lengths (0.66, 0.67 x 10^{-12}cm respectively), and despite the small proportion of residual hydrogen the major scattering process observed was coherent. The frequency distributions obtained are shown in figure 7.3. Extrapolations at low energies showed many systematic deviations from straight lines at small momentum transfers (for energy transfers less than 20 cm^{-1} in the case of the 295 K experiment, though this was not evident at the lower temperatures). The principal peak positions in the density of states is given in table 7.3.

The structure of $C_{10}D_8$ has been determined by Pawley and Yeats (1969b) and shown to have a slightly different unit cell size and atom positions to naphthalene. In a rigid body refinement the r.m.s. librations were 4.3, 4.4 and 5.7°, rather larger than the $C_{10}H_8$. The r.m.s. translation was found to be 0.32 Å. Ito, Suzuke and Yokoyama (1968) have measured the Raman spectrum at 4° and 77°K, and these data are included in table 7.3.

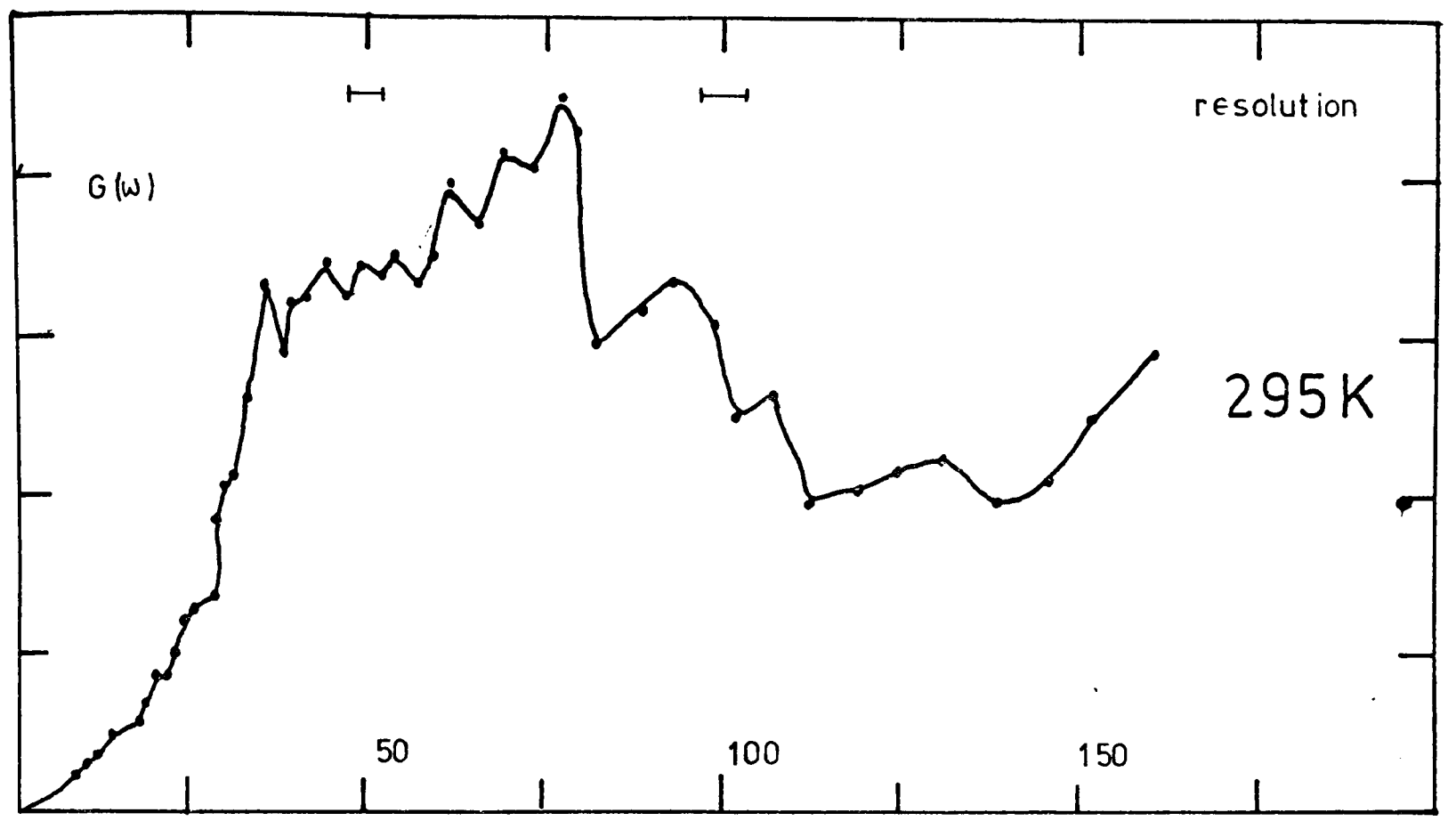
Table 7.3

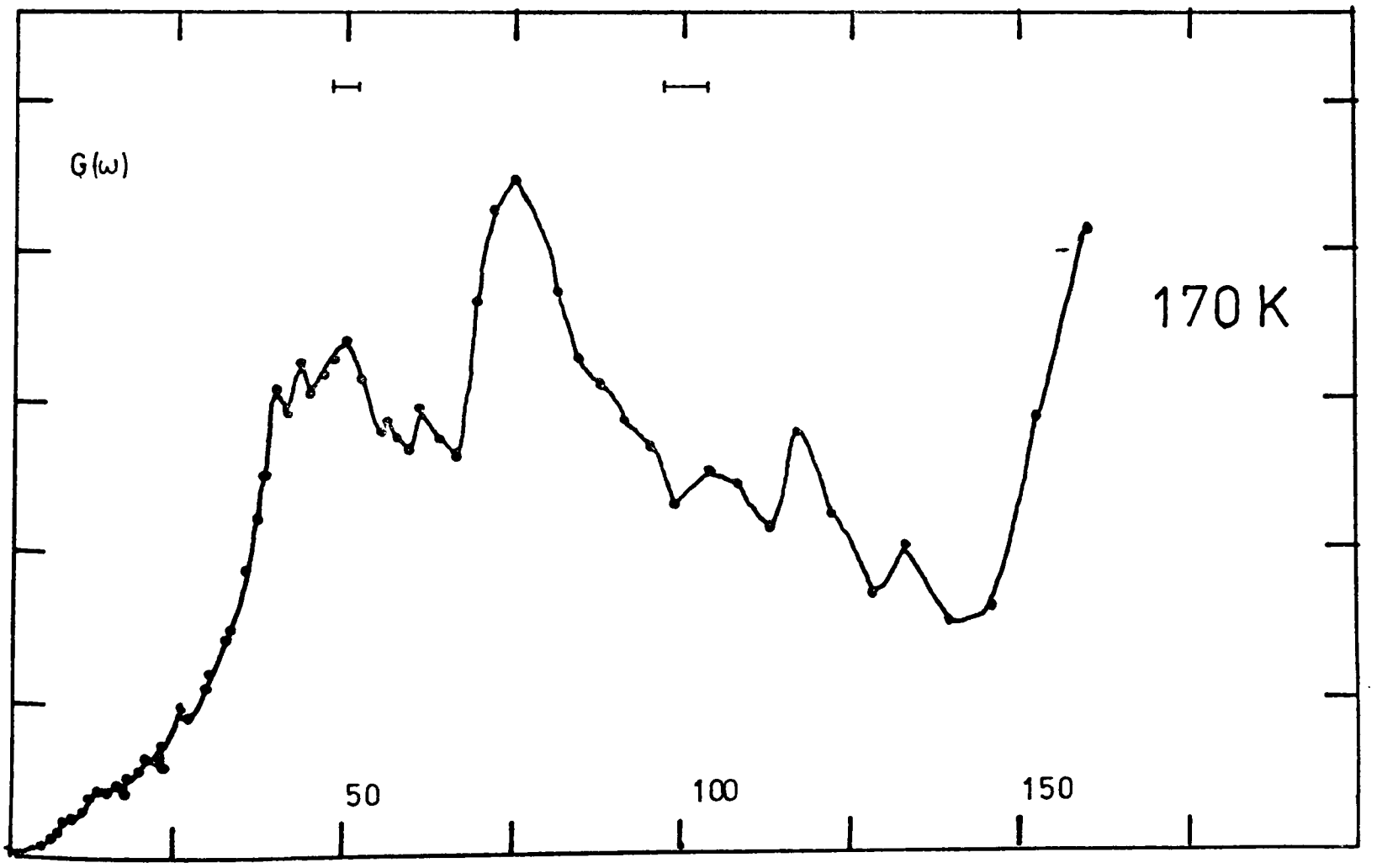
Intramolecular Modes of $C_{10}D_8$

Peaks observed in Density of States (cm^{-1})		Raman active modes (cm^{-1})			
295 K	170 K	290 K	77 K	4 K	Assignments
35	42	42	53	54	Bg
	50	49	62	64	Ag
	62	66	78	79	Bg
78	75	69	82	84	Ag
93	90 sh	102	110	112	Ag
107	105	118	128	130	Bg
130	118				

PER-DEUTERO-NAPHTHALENE

DENSITY OF STATES





ENERGY (cm^{-1})

Fig. 7·3

	295 K	170 K
Experimental Debye Temperature K.	145	85
Deviation from Debye behaviour cm^{-1}	27	36

As well as calculating $G^{inc}(\omega)$ for naphthalene Pawley and Reynolds estimated a $G^{coh}(|Q|\omega)$ for the polycrystalline deuteronaphthalene using a sampling technique which involved evaluating the eigenvectors at a value Q which is then allowed to uniformly sample a sphere about the origin in reciprocal space. The interference terms may be ignored as in the incoherent approximation if Q is sufficiently large. This was calculated for two values of Q, 2.0 and 2.5 $\AA^{-1}$. The results are shown in figure 7.4 with the experimental results taken at 170 K for comparison. Again on resolution grounds more detail should be observable. Further cooling is not necessarily going to yield a better result, since the Raman spectra indicate that the major shifts occur between 290 and 77 K (table 7.3).

The experimental Q range includes 2.5 $\AA^{-1}$ as an upper limit, but measurements on a time of flight spectrometer are not performed under constant Q conditions, and an average of the results for Q = 2 and 2.5 $\AA^{-1}$ show a closer comparison with the more diffuse experimental results. Calculation for additional Q values and averaging would offer an even more sensitive model test. The input data of $S(\alpha\beta)$ included terms where Q was less than 2 $\AA^{-1}$ but two thirds of the data came between 2 and 2.5 $\AA^{-1}$ momentum transfer, with extra weighting of the high Q terms; the experimental results should strongly reflect this region of momentum space.

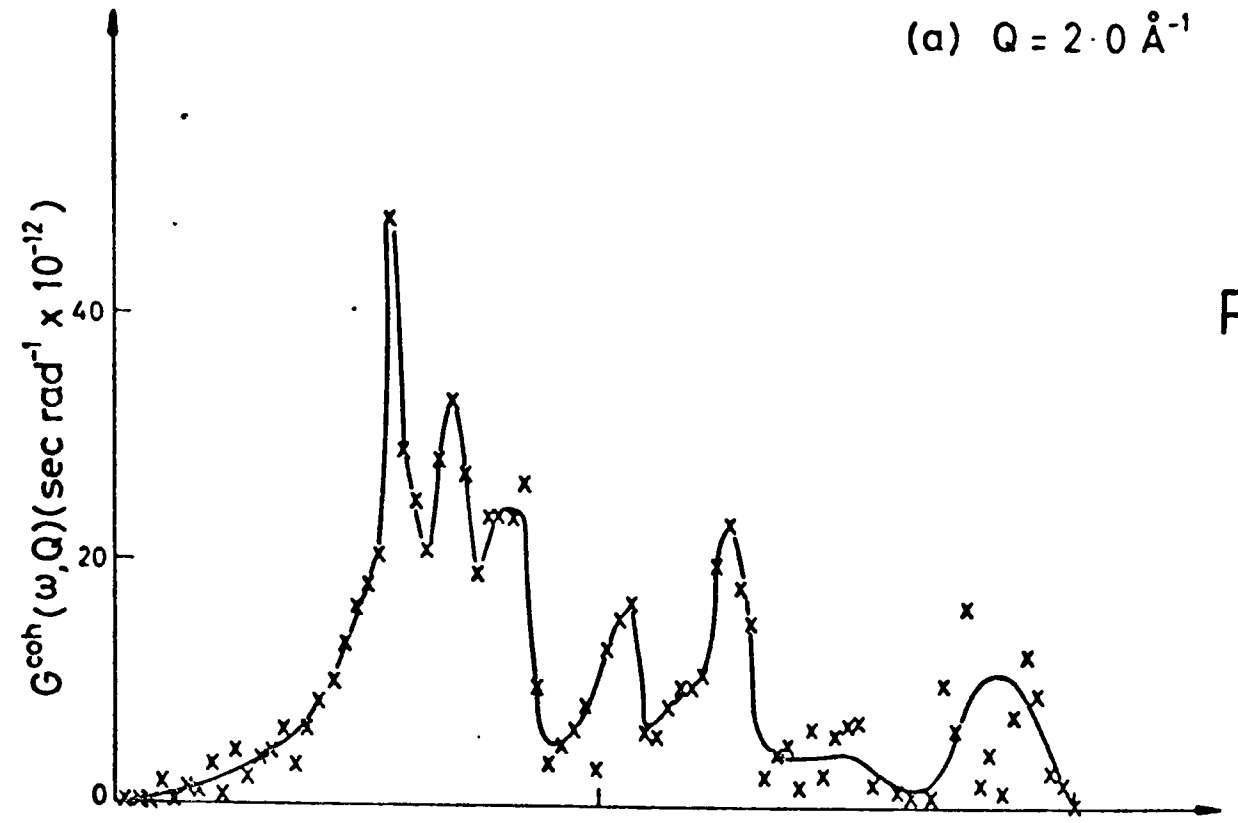
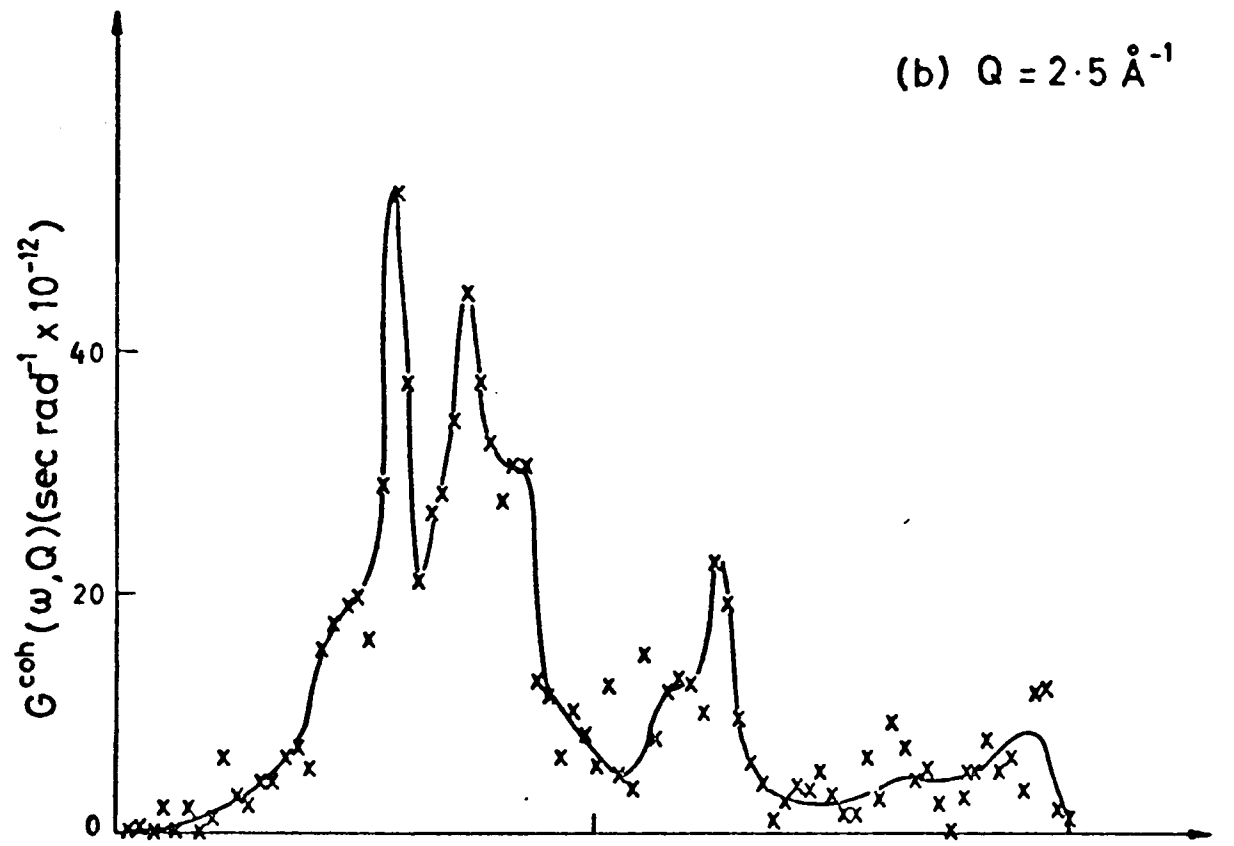
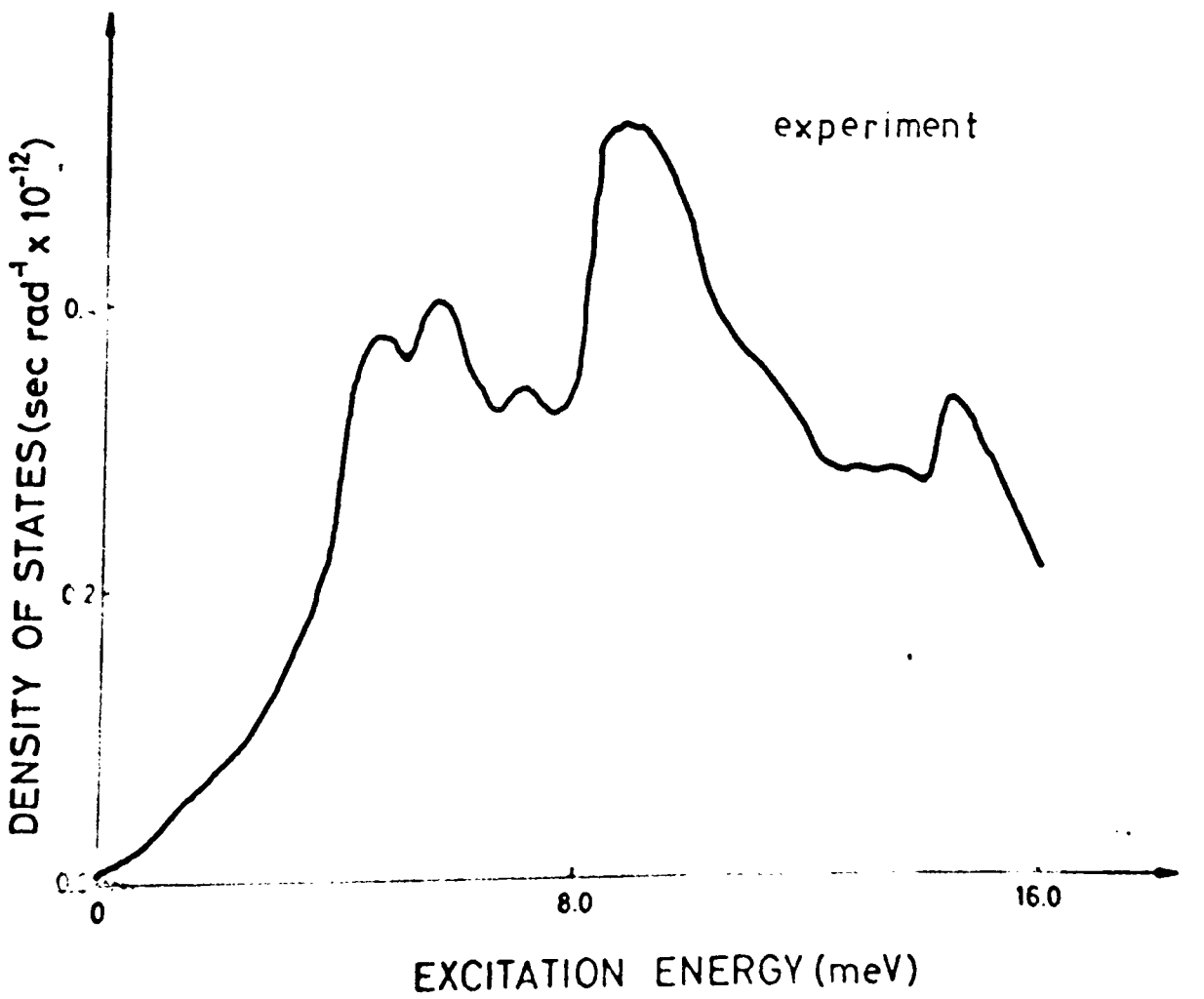

(a) Q = 2·0 Å^{-1}
$G^{coh}(\omega,Q)$(sec rad^{-1} x 10^{-12})
40
20
0

Fig. 7·4


(b) Q = 2·5 Å^{-1}
$G^{coh}(\omega,Q)$(sec rad^{-1} x 10^{-12})
40
20
0


experiment
DENSITY OF STATES (sec rad^{-1} x 10^{-12})
0.2
0
8.0
16.0
EXCITATION ENERGY (meV)

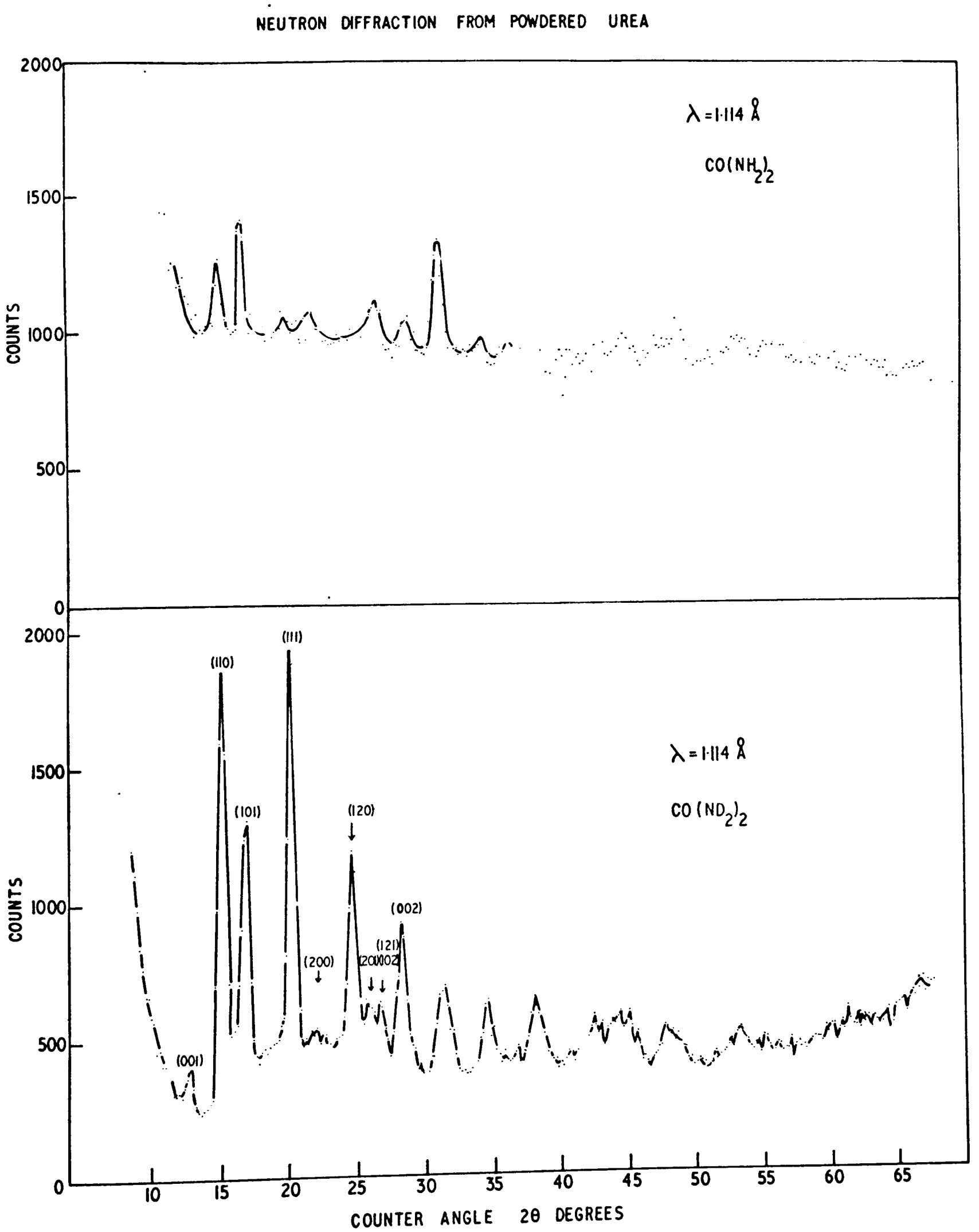
7.4 Urea

Unlike $C_{10}H_8$ and $C_{10}D_8$ which are almost completely incoherent and coherent scatterers respectively, the ratio of these two cross-sections for $CO(NH_2)_2$ is 10:1 and $CO(ND_2)_2$ is 1:50. The two compounds will be referred to as UH and UD. Neutron diffraction spectra from powdered specimens were obtained using the DIDO Badger diffractometer, and are shown in figure 7.5. The Bragg peaks have a considerable intensity in the case of UH, while the isotropic incoherent scattering from UD appears as a high background level in the lower spectrum. The presence of incoherent inelastic scattering has also been seen in figure 5.4.

1. Elastic Scattering

The variation of the intensity of elastic scattering with increasing momentum transfer is an exponential function of the Debye Waller factor, 2W (e.q. 3.8) and reflects the thermal clouds of the nuclei; though the average observed is not easily related to specific modes or atoms it does indicate in a qualitative way, the magnitude of the mean displacements. At peak flux wavelengths (used when the principal interest lies in the less intense inelastic scattering) the coherent scattering in UH prevented the usual analysis of plotting $\log_e$ (elastic peak intensity) versus Q^2. Using the 7H spectrometer at 3.8 Å on a polycrystalline sample showed that between 11° and 19° scatter angle air scattering and multiple Bragg scattering were important: above 45° the first Bragg peak interfered. The actual Debye Waller factor determined in the range between is small, and with very large corrections for absorption in the vanadium standard (2mm) the error may be underestimated. The use of long wavelength neutrons on 4H5 where few Bragg

Fig. 7·5


NEUTRON DIFFRACTION FROM POWDERED UREA
λ = 1·114 Å
CO(NH2)2
λ = 1·114 Å
CO(ND2)2
COUNTS
2000
1500
1000
500
0
(001)
(110)
(111)
(101)
(200)
(120)
(121)
(20Ī02)
(002)
10
15
20
25
30
35
40
45
50
55
60
65
COUNTER ANGLE 2θ DEGREES

peaks contribute to the scattering was successful in yielding straight line plots, though the vanadium (1 mm thick) absorption corrections were again large since the absorption cross-section is proportional to wavelength. The values obtained were:

Wavelength Å	2W ($Å^2$)	Number of Bragg peaks contributing to total scattering
10	0.015 ± 0.0004	0
7	0.050 ± 0.0005	3
3.8	0.037 ± 0.0005	10

The 100 reflection is absent because of the screw axis of symmetry. Because of absorption and the statistical error in the fewer counts collected at 10 Å the most reliable figure is that of the 7 Å measurement.

2. Inelastic Scattering

Spectra at 90, 170, 295, 390 and 413 K were obtained using 4H5 and 6H spectrometers. The experiment at 90°K was performed on 4H5 when the moderator chamber was empty and the statistics are consequently poor. The run at 413 K, eight degrees above the melting point lasted only 6 hours to reduce possibility of sample decomposition. The remaining runs lasted between 20 and 30 hours, cycling the sample periodically with the vanadium and blank.

At 90 K the population of the torsional internal mode at 520 cm^{-1} is very small and it is hardly visible at τ = 300 μsec/m (figure 7.6). The spectra at 170 K (fig. 7.6) are well defined statistically and clearly show five peaks at 62, 76, 142, 175 and 470 cm^{-1}.

Two runs were performed at different wavelengths for the room temperature experiment so that the momentum and energy space

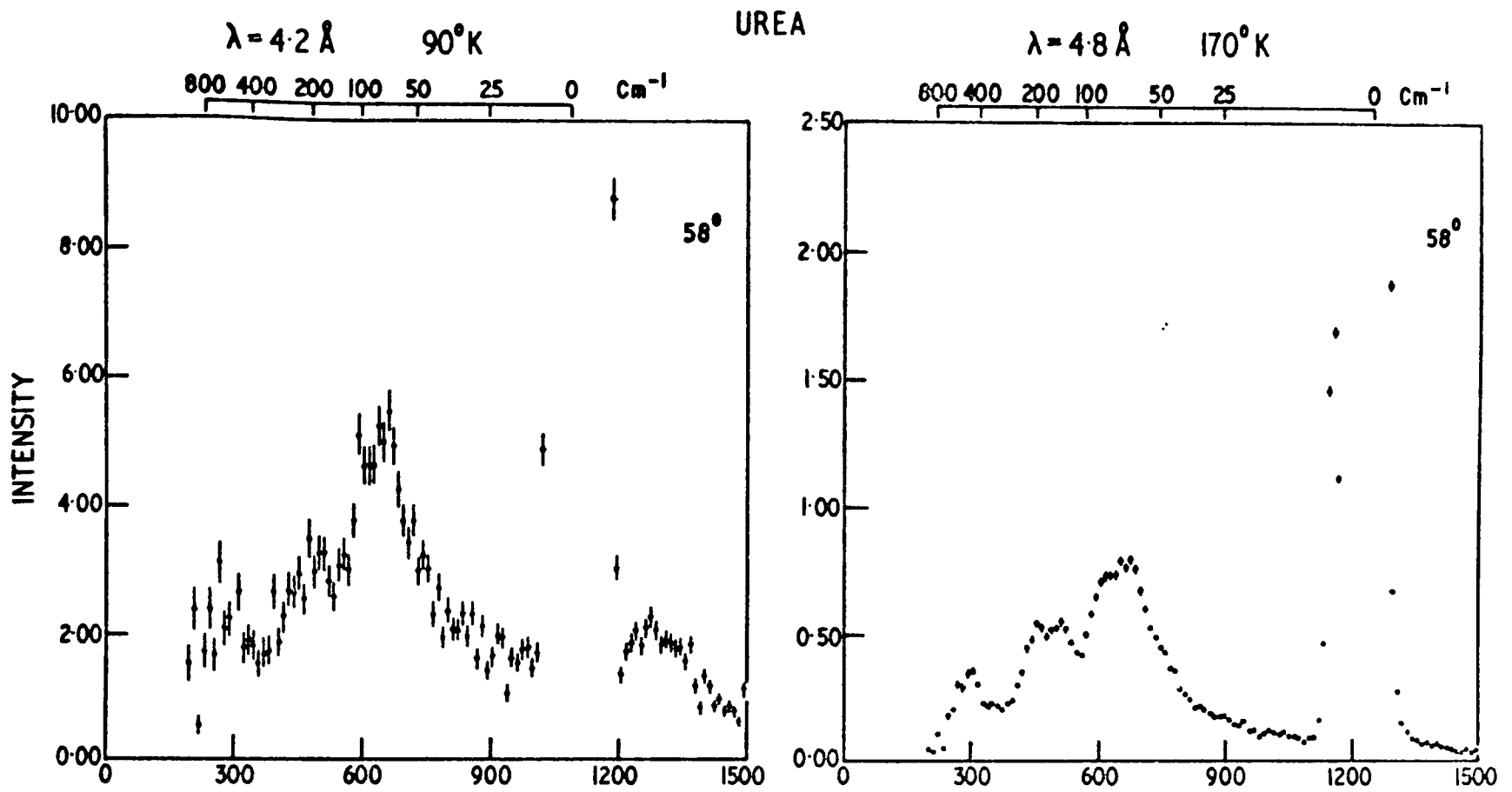

UREA
λ = 4·2 Å
90°K
800 400 200 100 50 25 0 Cm⁻¹
10·00
8·00
6·00
4·00
2·00
0·00
INTENSITY
58°
0 300 600 900 1200 1500
λ = 4·8 Å
170° K
600 400 200 100 50 25 0 Cm⁻¹
2·50
2·00
1·50
1·00
0·50
0·00
58°
0 300 600 900 1200 1500
800 400 200 100 50 25 0 Cm⁻¹
10·00
8·00
6·00
4·00
2·00
0·00
INTENSITY
90°
0 300 600 900 1200 1500
TIME OF FLIGHT (μ sec/metre)
800 400 200 100 50 25 0 Cm⁻¹
2·50
2·00
1·50
1·00
0·50
0·00
90°
0 300 600 900 1200 1500
TIME OF FLIGHT (u sec/metre)

Fig. 7·6

sampled might be extended; the normalised differential cross-section is shown in fig. 7.7 at six scatter angles for 4.2 Å and 5.1 Å incident neutrons. At 72° scatter and 72 cm^{-1} energy transfer, the surface area of the sphere in reciprocal space swept out by the Q vector is 18% larger with 4.2 Å incident neutrons than with 5.1 Å. This averaging effect reduces the very sharp coherent features seen in the longer wavelength experiment between 50 and 200 cm^{-1} and the spectrum at 4.2 Å begins to resemble the frequency distribution. The two runs were normalised together making available eighteen data points in $S(\alpha\beta)$ at constant β for averaging and extrapolation of which fifteen could be used by FLORENCE. The detectors on 6H at 18°, 27° and 36° subtend one third the solid angle of each of the rest (figure 6.2) accounting for the poorer statistics in these spectra.

The sample was contained in a machined 'dural' can for the runs at elevated temperatures, sealed with an aluminium gasket. To prevent the pressure of ammonia distorting the thin windows during the run with molten urea, the seal was not completed at the top of the can, and during the subsequent run the changer was not cycled. Sample spectra at 390 and 413 K are shown in figure 7.8. Almost all the low energy structure seen at lower temperatures has collapsed leaving a broad featureless region of lattice modes. There is a possibility in the case of the solid of Bragg scattering at 54° from the (001) planes. In the case of the liquid the elastic peak area has fallen considerably and there are signs of the quasi-elastic broadening characteristic of liquids. Frequency distributions were derived for the four runs between 170 and 413 K, and are shown in figure 7.9. A summary list of peak positions in the density of states spectra is given in table 7.4. Errors in the estimated cross-

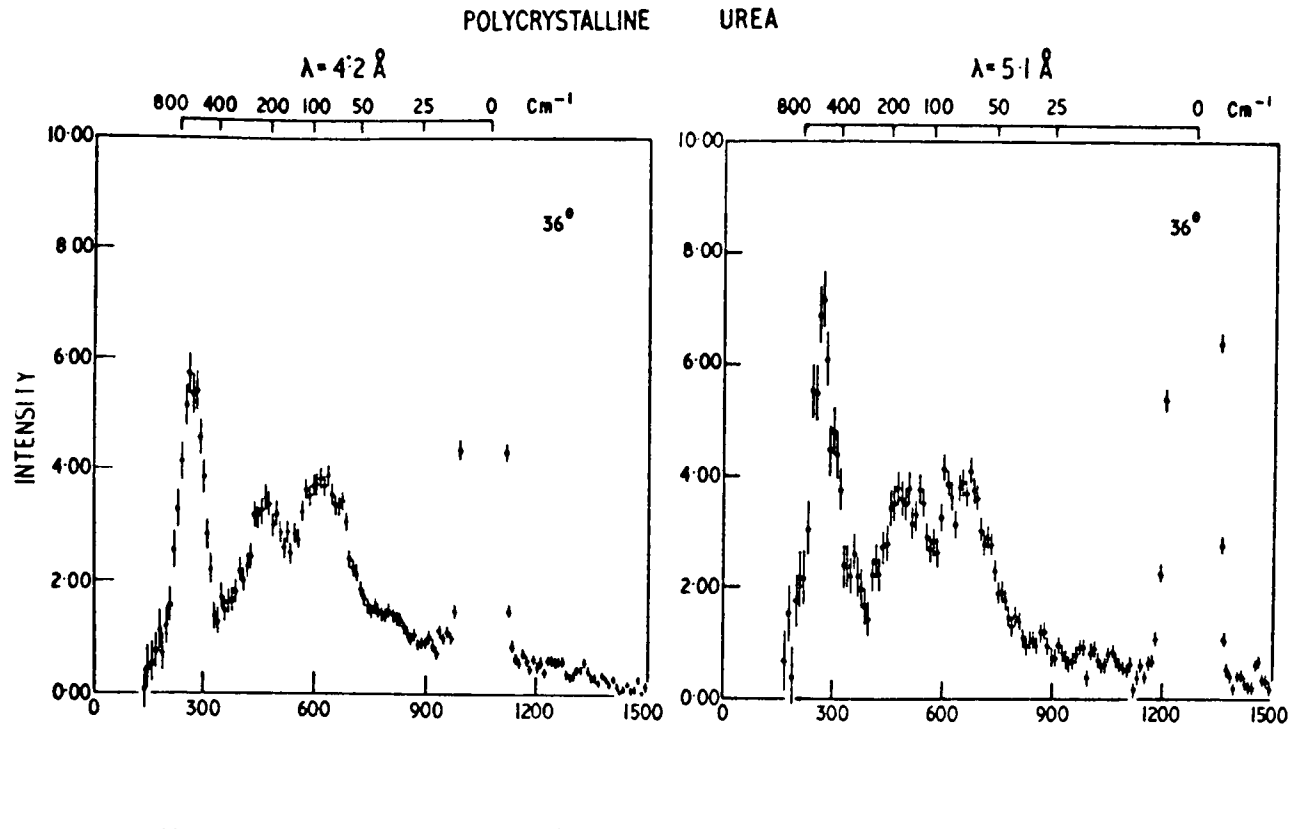

POLYCRYSTALLINE UREA
λ = 4·2 Å
λ = 5·1 Å
800 400 200 100 50 25 0 Cm⁻¹
36°
72°
90°
INTENSITY
TIME OF FLIGHT (μ sec/metre)
0·00
2·00
4·00
6·00
8·00
10·00
0
300
600
900
1200
1500

Fig. 7·7

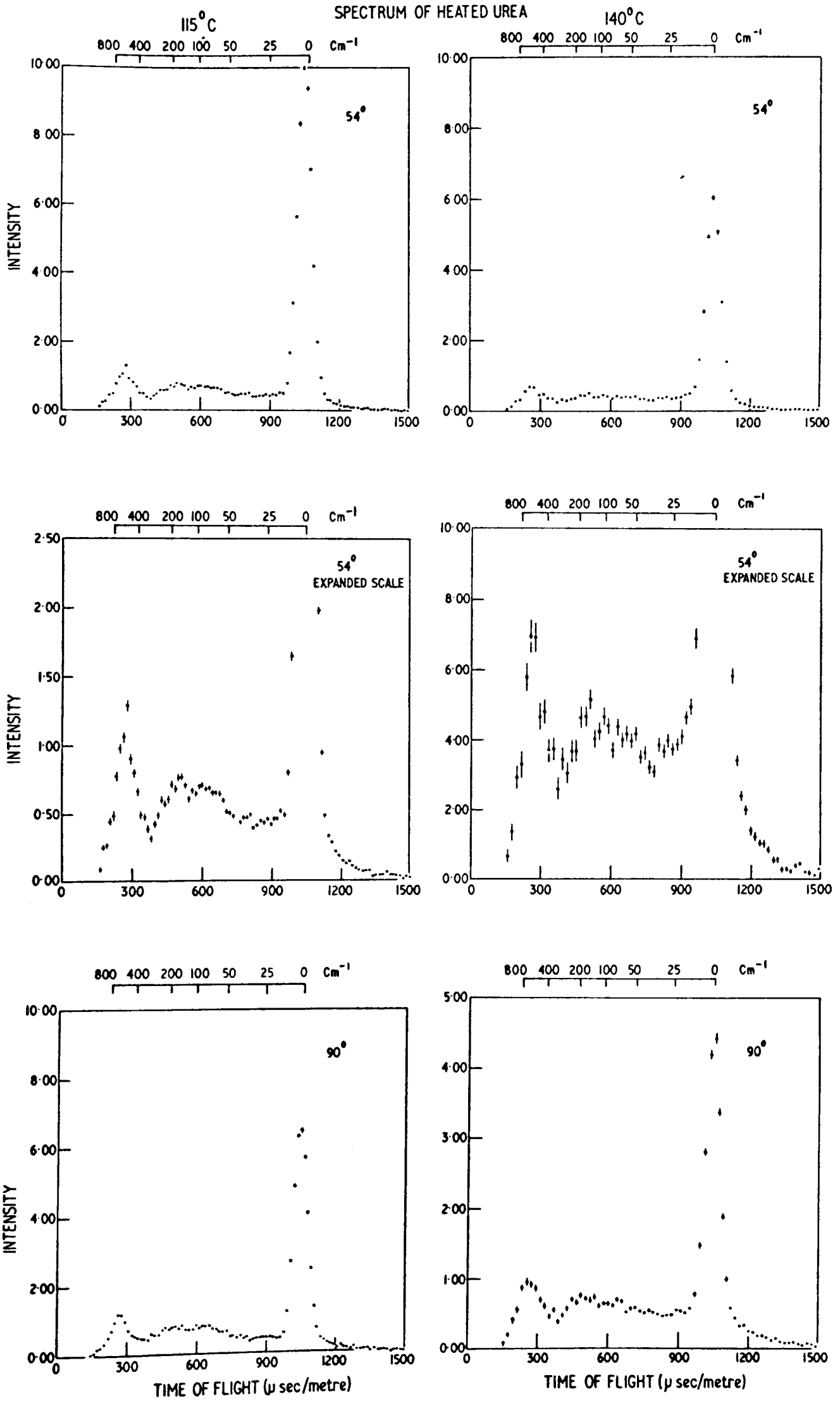

SPECTRUM OF HEATED UREA
115°C
140°C
800 400 200 100 50 25 0 Cm⁻¹
54°
EXPANDED SCALE
90°
INTENSITY
TIME OF FLIGHT (μ sec/metre)
0 300 600 900 1200 1500

Fig. 7·8

UREA

DENSITY OF STATES $G^{INC}_{EXP}(\omega)$

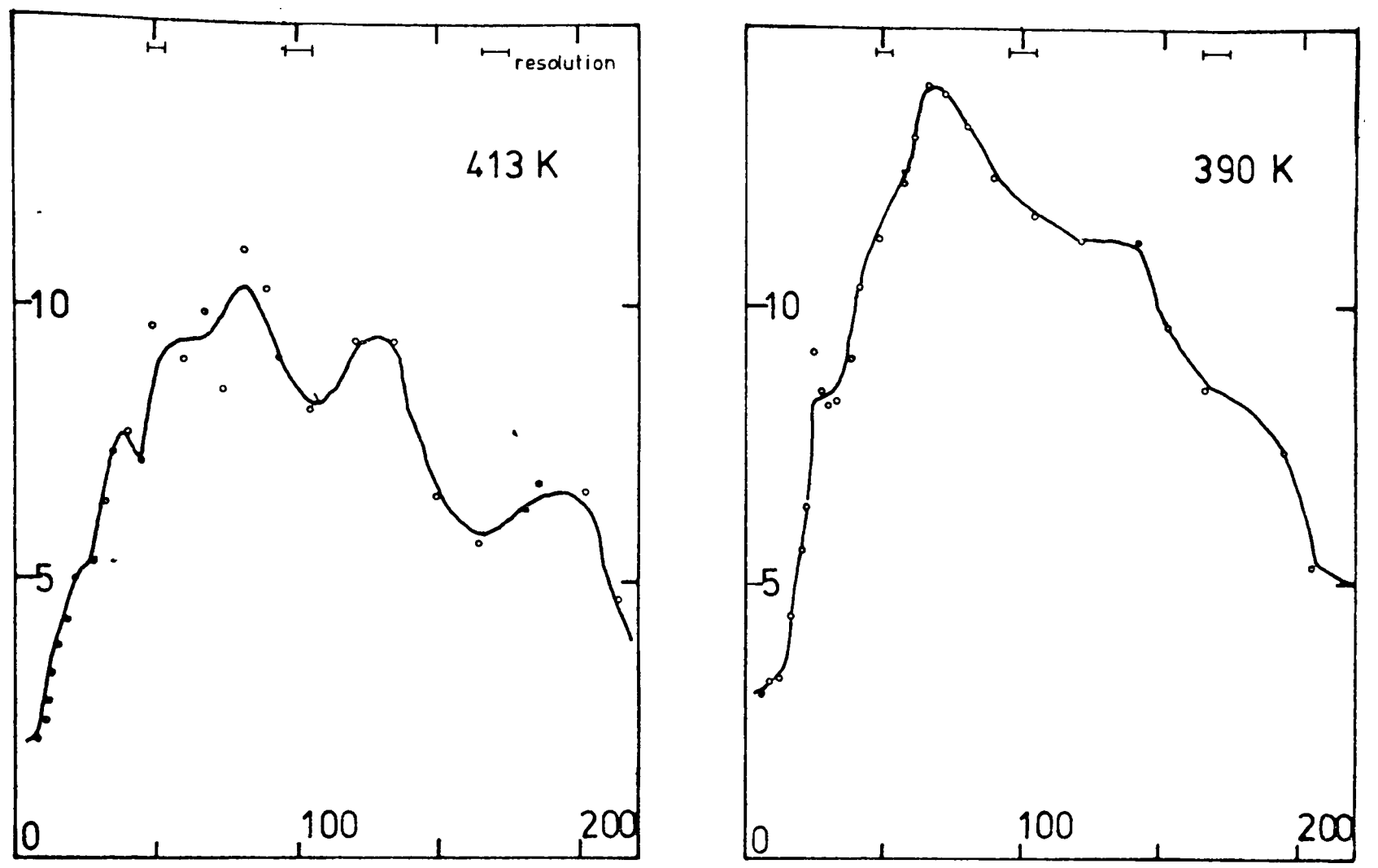


Fig. 7·9

section account for the differences in the absolute scaling.

Table 7.4

Intermolecular Modes of $CO(NH_2)_2$

Peaks observed in the Density of States				Optical Data	
170 K	295 K	388 K	413K	295 K	Assignment
		26			
		43 sh	40		
66	55	66		58	B_1
76	75				
82			80		
104	102			104	E
120	112			135	A_1
	132	132	130	137	E
150	153				
180	172	190 sh	190	175	E
Debye Temperature K					
164	156	139	-		
Deviation from Debye behaviour (cm^{-1})					
63	20	20	-		

Results from Urea (d_4)

The time of flight spectra of UD were obtained at 190 K and at room temperature. There is much less detail to be seen in the spectrum at 190 K fig. 7.10 than for UH at 170 K fig. 7.6, though for UD at both 58° and 90° the usual parabolic shape of the density of states is distorted by low energy modes. The internal mode of the amide group is seen to have fallen to about 400 cm^{-1} showing the effect of isotopic substitution of the heavier deuterium. The room temperature measurements were again performed with one run at 4.2, and the others at 5.1 Å and results of six angles are shown in fig. 7.11. Several coherent features are clearly evident with an neutron energy loss peak at 36°, 4.2 Å, and a broad energy gain peak emerging

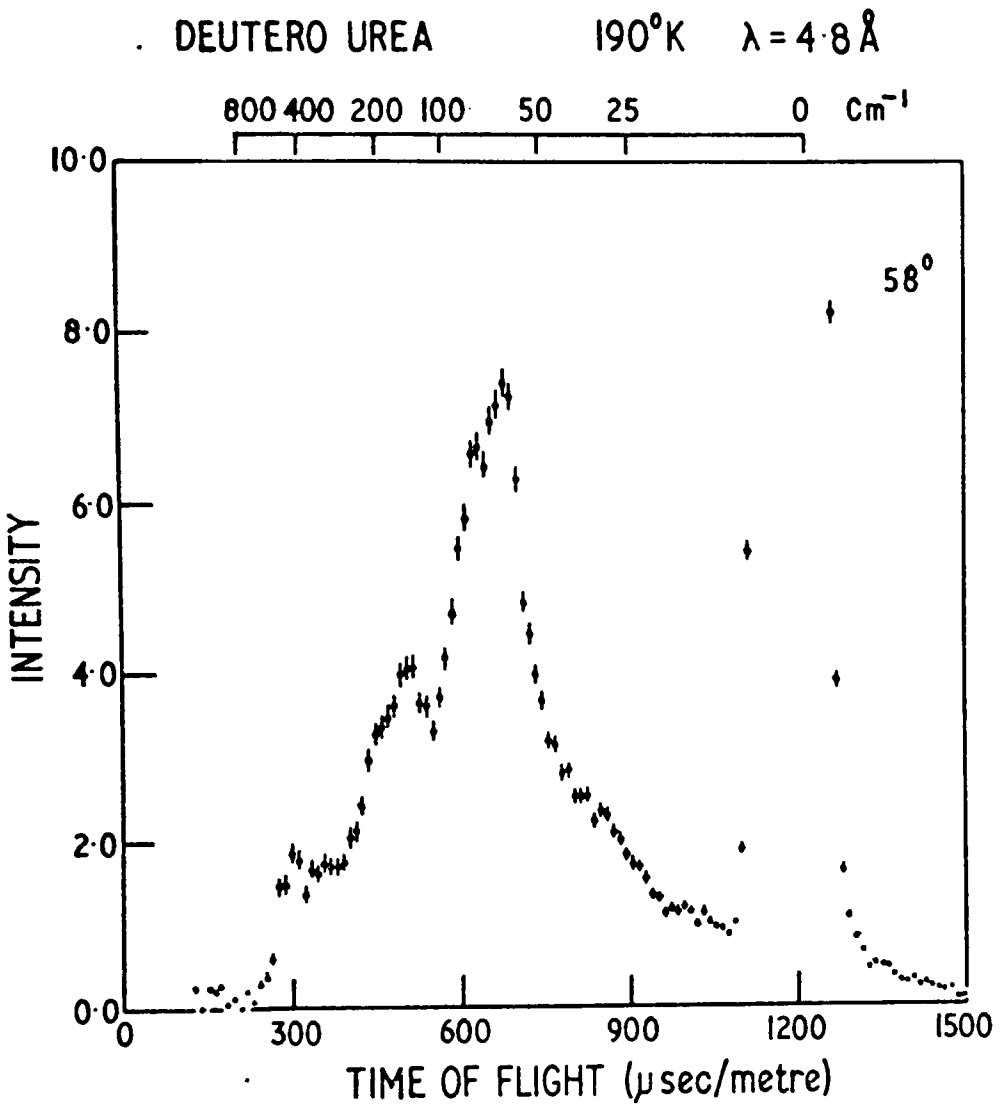
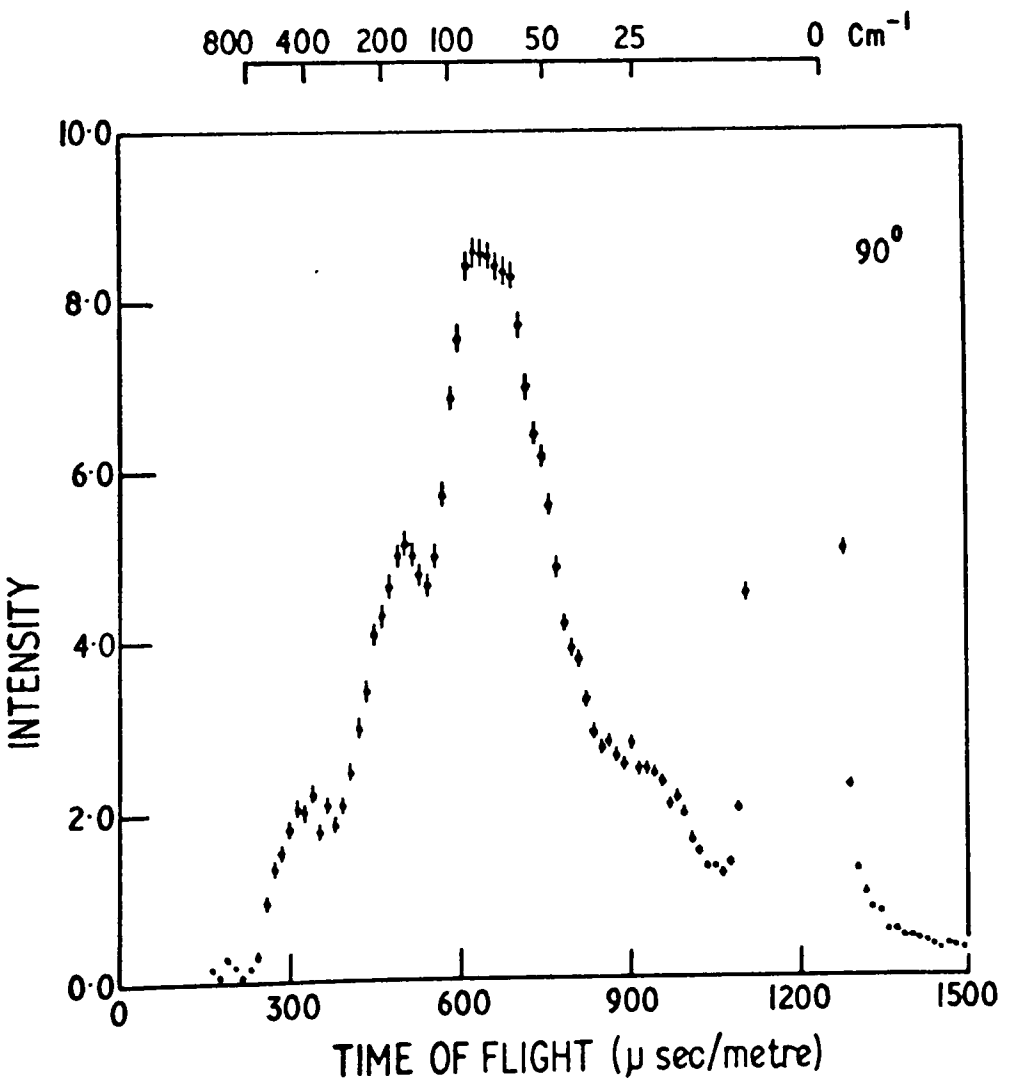

DEUTERO UREA
190°K
λ = 4·8 Å
800 400 200 100 50 25 0 Cm⁻¹
10·0
8·0
6·0
4·0
2·0
0·0
58°
INTENSITY
0
300
600
900
1200
1500
TIME OF FLIGHT (μsec/metre)

Fig. 7·10


800 400 200 100 50 25 0 Cm⁻¹
10·0
8·0
6·0
4·0
2·0
0·0
90°
INTENSITY
0
300
600
900
1200
1500
TIME OF FLIGHT (μ sec/metre)

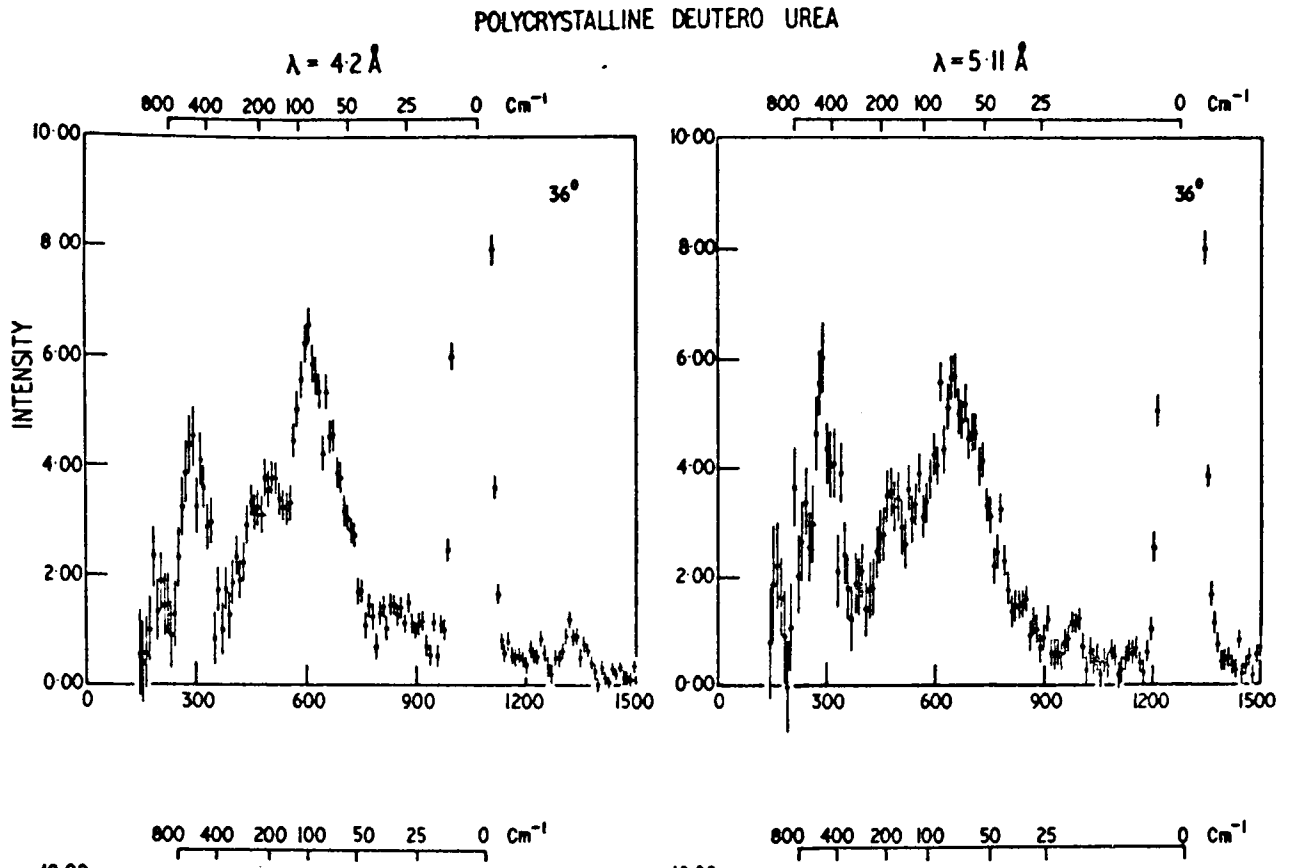

POLYCRYSTALLINE DEUTERO UREA
λ = 4·2 Å
λ = 5·11 Å
800 400 200 100 50 25 0 Cm⁻¹
36°
72°
90°
INTENSITY
10·00
8·00
6·00
4·00
2·00
0·00
0 300 600 900 1200 1500
TIME OF FLIGHT (μsec/metre)

Fig. 7·11

from the elastic peak at 72°, 5.1 Å. With the arguments of section 7, this corresponds to an envelope of transverse modes, being broad and symmetrical; the centre corresponds to $|Q|$ = 1.599, and ω = 10.7 cm^{-1}. The reduced q is 0.39 taking it to be a 110 transverse mode, or 0.38 taking the (101) as the terminal Brillouin zone. A coherent feature at 36°, 4.2 Å for UH at 35 cm^{-1} is not observed in the comparable spectrum of UD suggesting that there are differences in the low energy dynamics of the two systems. Again this coherent scatterer was treated in the incoherent approximation, and frequency distributions obtained for both temperatures (fig. 7.12). Fig. 7.13 indicates the effect of coherent scattering in the extrapolation: if the 110 plane is considered as being dominant these peaks in $S(\alpha\beta)$ correspond in order of increasing Q to a longitudinal, a transverse, and longitudinal mode at 16 cm^{-1}, all close to the zone boundary of the (110) zone.

Table 7.5

Intermolecular modes of $CO(ND_2)_2$

Peaks in Density of States cm^{-1}		Optically active modes cm^{-1}		
190 K	293 K	Infrared	Raman	Assignments
		-	-	A_1
62	59	-	56	B_1
77	73	99	100	E
90sh	104	135	133	E
120sh	128	174	167	E
136	170			
178	210sh			
200sh				

UREA (d_4)

DENSITY OF STATES

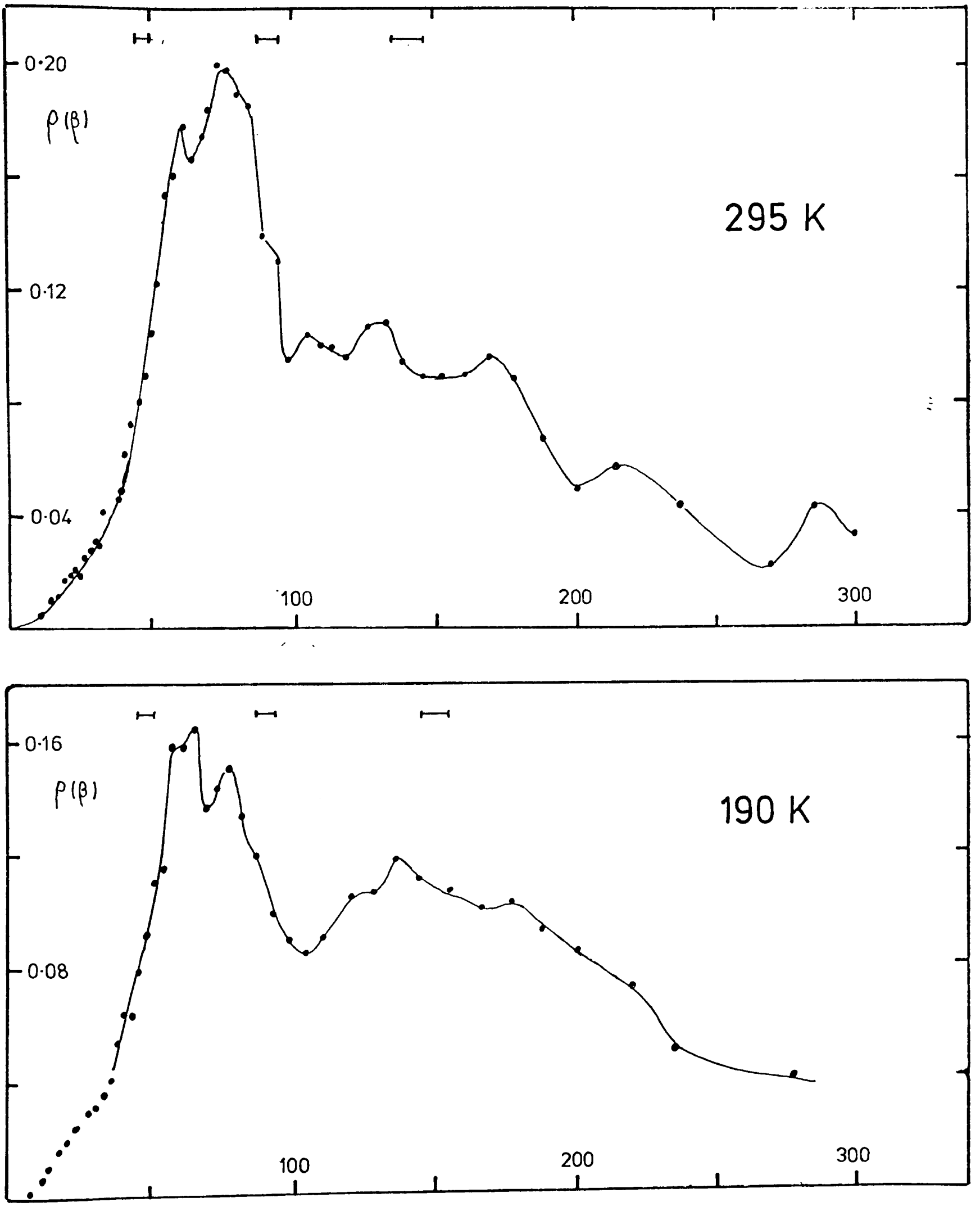
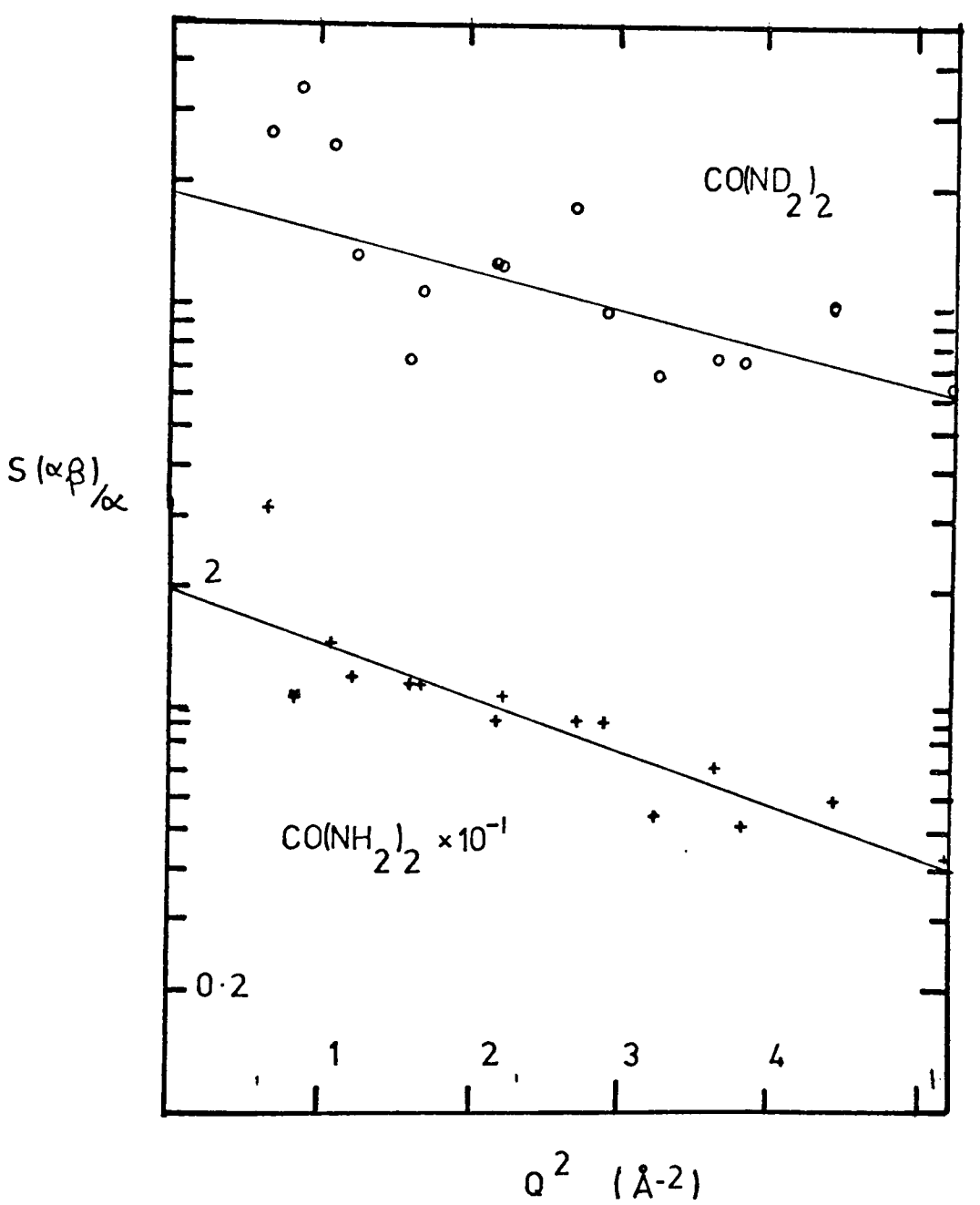


Fig. 7·12

EXTRAPOLATION PLOTS FOR UREA AND UREA (d_4)



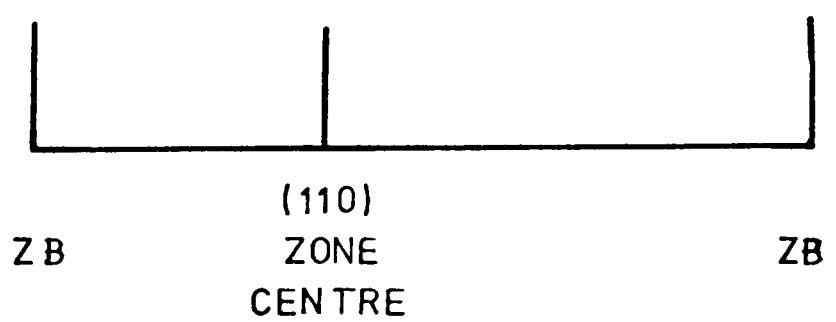


Fig. 7·13

	190 K	293 K
Experimental Debye Temperature K	195	187
Deviation from Debye behaviour cm^{-1}	27.6	20

Egelstaff shows that $S(Q\omega)$ may be written as three terms,

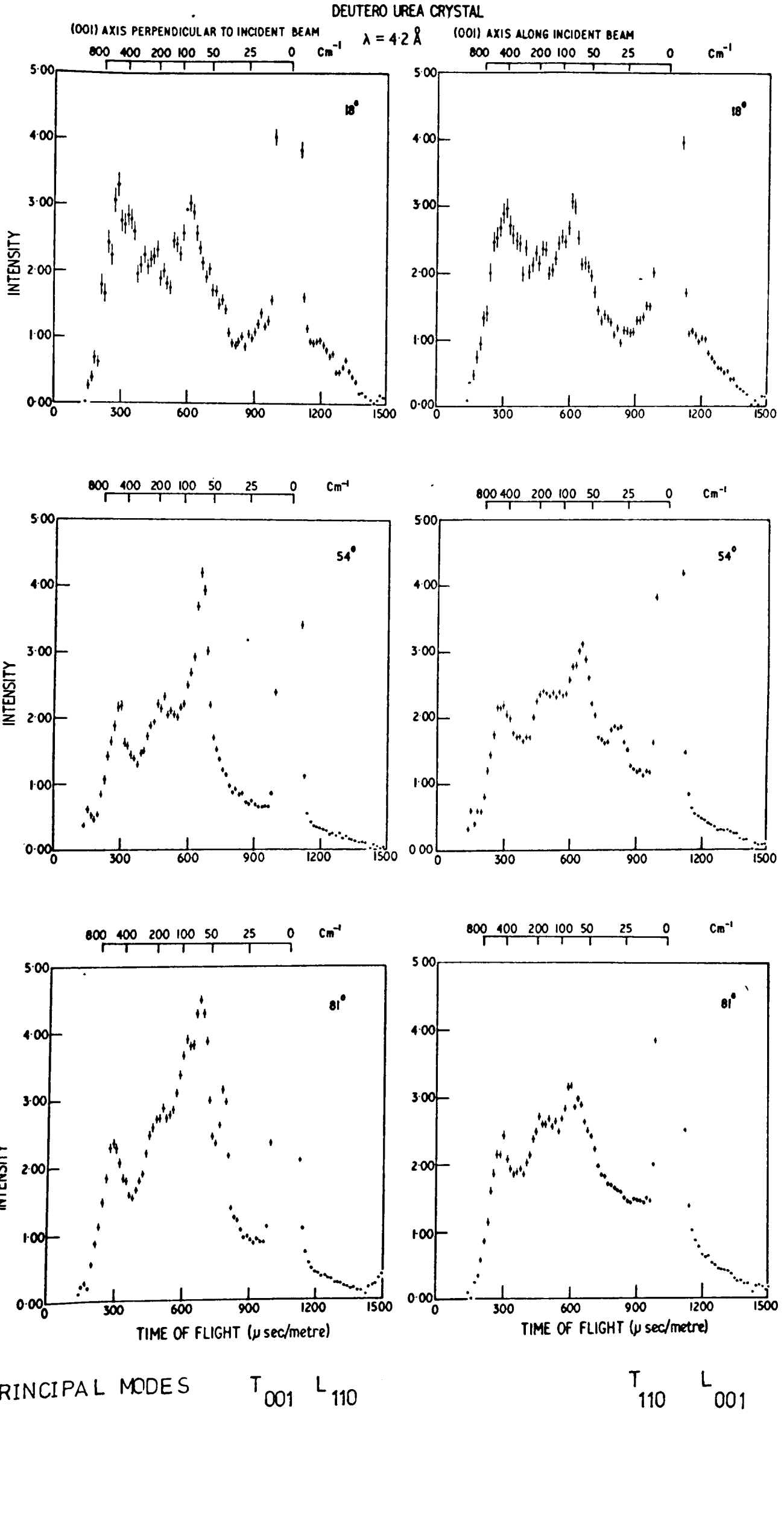
$$e^{-2W_o}\ \delta(\omega) + \frac{h\sigma^2}{2mkT}\left[e^{-2W_z}\ V_z(\omega) + e^{-2W_{xy}}\ V_{xy}(\omega)\right] \qquad 7.3$$

The first term is elastic scattering; the other two terms correspond to the frequency spectrum associated with vibration in the z plane, and xy plane respectively. (Downes, Egelstaff and White, 1967). Time of flight spectra of two crystals were measured on 6H oriented about the incident wavevector so that Q for small energy transfers would be first perpendicular to τ_{001} (and k_o perpendicular to <001>) and then parallel to τ_{001}, and the resulting spectra are shown in fig. 7.14. As expected there are a large number of phonons visible, but the most pronounced differences are the peaks which may be attributed to the $^{L}110$ and $^{T}001$ phonons at 33 cm^{-1} where L and T denote longitudinal and transverse polarisations with the direction of propogation as a subscript. The frequency distributions succeed in averaging out the major coherent contribution and are shown in fig. 7.15. The coherent Bragg scattering in these experiments did not enter any detectors, consequently it was possible to derive Debye Waller factor for the motions along the c axis as 2W = 0.097 and transverse as 2W = 0.094 from the residual incoherent scattering.

7.5 Discussion of Urea Results

For a compound of molecular weight = 60, the compound has an abnormally high melting point of 132°, this being attributed

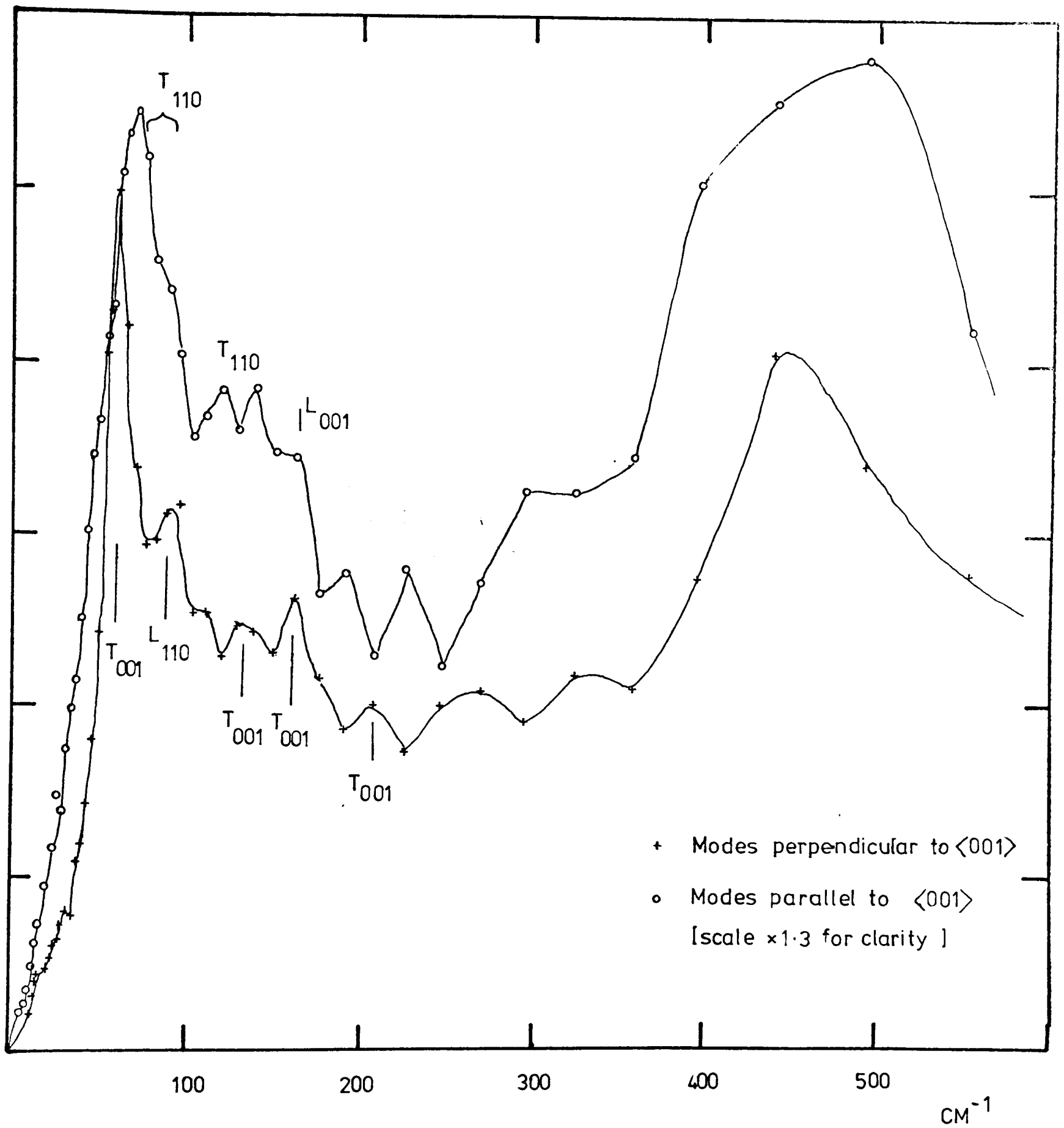
FIG. 7.14



PRINCIPAL MODES T_{001} L_{110} T_{110} L_{001}

UREA (d_4) CRYSTAL

DENSITY OF STATES



ENERGY

Fig. 7·15

to the hydrogen bond forming a three dimensional net in the lattice. The crystal is easily cleaved along the 110 faces and this is reflected in the very low shear elastic moduli. Because of the simple molecular structure and crystal structure with only five atoms in the basic asymetric unit many structure determinations have been performed with increasing detail in the refinements. Caron and Donohue (C-D), 1964, reanalyse the X-ray data of Vaughan and Donohue (1952); neutron diffraction studies have been performed by Worsham, Levy and Peterson, 1957 and comprehensively by Prior and Sanger, 1970 (P-S). Sklar, Senko and Post, 1961, determine the decrease in lattice parameters with decreasing temperature, showing how much more marked it is in the case of the <100> than the <001>. Analysis in terms of rigid body motions indicate r.m.s. librations about the 1, 2, and 3-axis as 4^{o}, 5.5^{o} and 11^{o} (P-S). Similar values are obtained by C-D. The other results of P-S may be summarised: The hydrogen deviate considerably from rigid body behaviour, both vibrating more in the 3 than the 12 directions, while the horizontally bound hydrogen vibrates 30% less in the 12 plane than required by a rigid molecule, and deviations from this behaviour, though slight, are seen for the CCNN skeleton. In a refinement for anharmonic parameters no improvement was produced, and the conclusion was drawn that the principal motions were harmonic. The thermal factors for the translations along the 1,2 and 3 axes are 0.0447, 0.0304, and 0.174 $\mathring{A}^2$.

The optical data on UH and UD has been summarised in Table 7.5. Cooling to $77^{o}K$ results in the A_1 mode increasing from 138 to 149 cm^{-1} for UH, (G-B).

Measurements of the heat capacity of urea have suggested transitions between -6 and $5^{o}C$, and 25 to 37^{o} (Sokolov, 1940)

but Ruehrwein and Huffman, 1946, observe no discontinuities attributable to phase transition between 19 and 320 K.

Direct observation of the molecular dynamics comes in nuclear magnetic resonance measurements on the solid (Richards, 1967): broad proton resonance lines are observed due to contributions to the local field from adjacent protons (van Vleck, 1948). When the relative proton motions are at a greater rate than $(T_2)^{-1}$, the spin-spin relaxation rate, then only the average is reflected in the width of the resonance frequency. By using a single crystal, the local field may be examined using the line-broadenings as a function of crystal orientation, and results compared with calculations based on the geometry of the neighbours. This enables an axis of reorientation to be identified, and the magnitude may be compared with different models for the mechanism. Measurement of nuclear quadrupole resonance of the ^{14}N also gives insight into the reorientation since this averages the local electric field gradients. If these fluctuations are sufficiently rapid the protons may be decoupled and a line-narrowing due to reduction in T_2 observed.

In the case of urea there is some decrease of the second moment at 298° from values at 273K, (Emsley and Smith, 1961) which is shown to correlate closely with molecular orientation about the C = O axis. Rotation of the $-NH_2$ group is eliminated by estimating the linewidth changes, and on simple energetic grounds of the high torsion frequency of 500 cm^{-1}. The activation energy for the C = O reorientation is 9 Kcals $mole^{-1}$. Even invoking decoupling of the protons from the nitrogen nuclei by the reorientational process fails to account for all the narrowing observed. Kromhout and Moulton (1955) place a linewidth transition at 323 K.

One model lattice dynamical calculation has been attempted for urea by McKenzie and Prior, 1971, using a valence force field approach to the hydrogen bonds linking rigid molecules, the two types of bonds present being indicated by solid and chain lines in fig. 4.7. The dispersion curve calculated along the 001 is soluble as a real eigenvector problem and is shown in figure 7.16. By taking the optical data of Arnau and Giguere as well as elastic constant measurements, no satisfactory set of force constants would yield a reasonable fit. The modes are labelled with the zone centre labels, and the E modes remain degenerate in the model. The only qualitative similarity is the proposed rise of the longitudinal optic mode A_1.

Comparison with HMT and naphthalene shows that the urea has generally more distinctive features than either, and that the temperature dependence of the spectra is very marked in the case of UH; though $C_{10}H_8$ and $C_{10}D_8$ do show systematic shifts.

The neutron data for the hydrogenous urea show a collapse of the strong lattice modes by 388 K, and a great similarity to the liquid phase.

At room temperature, the principal peaks do correspond to the librational modes observed at the zone centre, though considerable dispersion is evident. Cooling to 170 K distinguishes the librational modes quite clearly, though there are frequency shifts compared with the room temperature optical data.

A feature of the neutron data for UD is the small overall change caused by lowering the temperature, though this reflects $G(\omega)$ rather than the heavily hydrogen weighted $G^{inc}(\omega)$ of UH, and the only modes showing great changes are the librational modes, of large amplitude.

The frequency distributions measured for the two sets of

UREA

CALCULATED DISPERSION CURVES

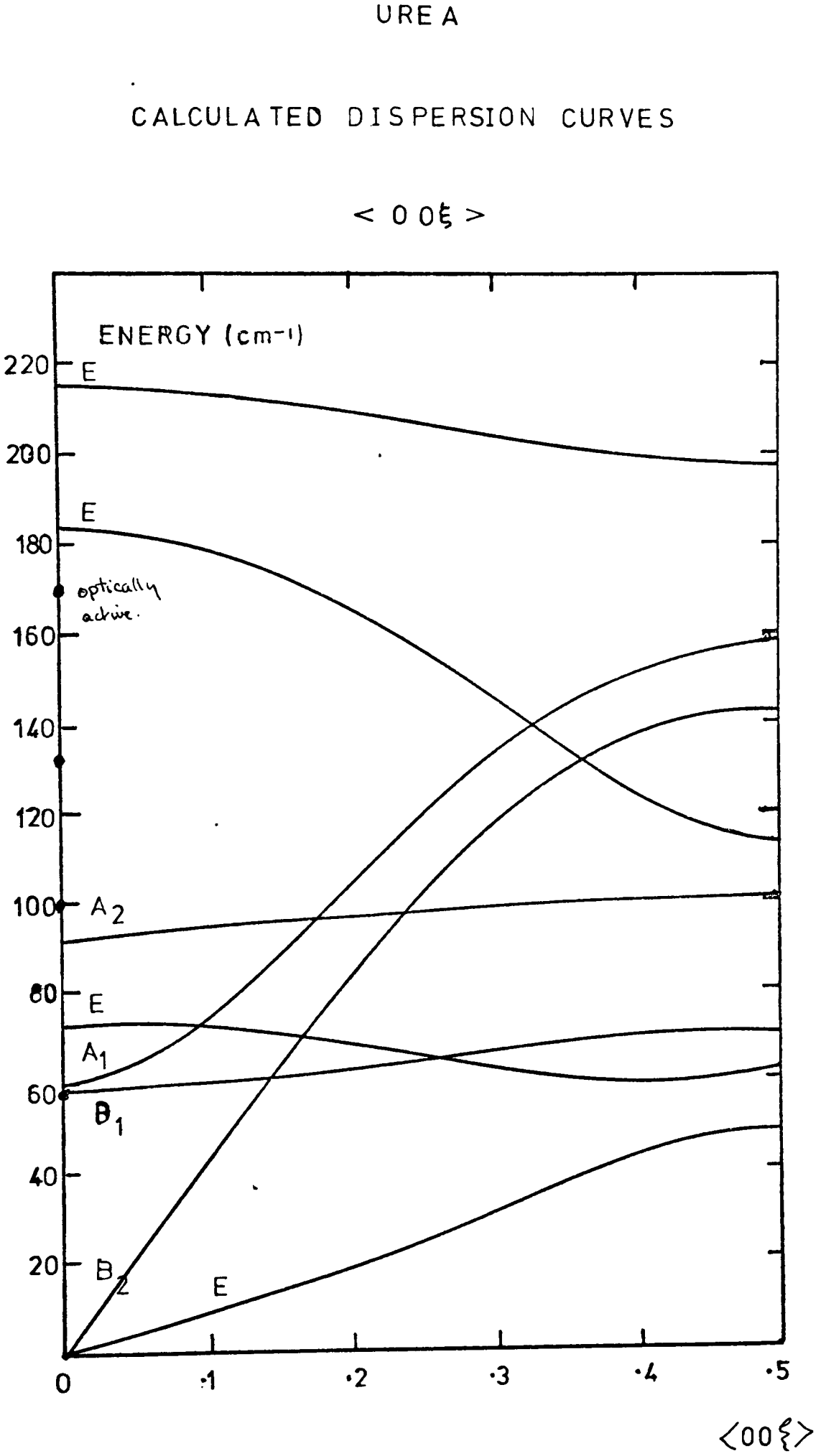


fig. 7.16

mode polarisations, (T_{110}, L_{001}), and (L_{110}, T_{001}) corresponding to the two crystal orientations may be qualitatively compared with the dispersion curves for the two directions, and there is considerable agreement. Marked on fig. 7.15 are the assignments of the singularities from the comparison,

The interpretation to be placed on the <001> branches is that at ambient temperatures the coupling between the molecules along the (001) axis is fairly strong. Asymmetry of the force field for the translation along the axis would cause the rather sharp rise in the mode j. Both the librational branches c and i show considerable dispersion. The modes along the <110> directions are dominated by the rapid fall of the librational modes. This appears to be analogous to displacive ferroelectrics. Cochran 1960, shows that an optic mode may become imaginary in the harmonic approximation, and the lattice becomes unstable with respect to this mode leading to a ferroelectric phase transition. Here these librations are the modes which will become the free rotations of the molecules, this finally occurring when the mode falls to zero energy. A considerable amount of evidence exists on the n.m.r. time-scale for this reorientation about the C = O initially. Considering the <001> direction and the small dispersion at 295 K, the mechanism is probably one of chains of molecules rotating together about the 3-axis, and only at the linewidth transition at higher temperatures do the cooperative motions of the linked chains break down. The effect of the modes falling slowly with temperature would account for the second order transition, in addition correlated motion in chains would reduce the energy barrier to rotation, retaining the zone centre optic mode at 58 cm^{-1}. Detail differences may exist between UH and UD due to differences

in the hydrogen and deuterium bond strengths which govern the reorientation process.

7.6 Oxamide and Thiourea

The neutron scattering spectrum of oxamide was measured at room temperature and the density of states is shown in figure 7.17.

The unit cell contains only one molecule per unit cell, and consequently there are only six branches to the dispersion relations, of which three are acoustic. The molecule is planar, with the two carbonyl groups in a transposition Ayerst and Duke, 1954; the formation of these into sheets is one reason for the high melting point (decomposes at 420°C), and small thermal motions. The crystal is triclinic, with space group $P\bar{1}$; the site symmetry is centrosymmetric so the three A_u modes corresponding to the acoustic modes are inactive in the infrared, and the three A_g modes of the librations are only active in the Raman spectrum, and have been measured at 106, 134 and 157 cm^{-1}. (Durig Brown and Hannum, 1971). There is a low energy CCN torsion observed at 165 cm^{-1} in the optical spectrum, though this is mixed with the lattice modes, and broadens to encompass the adjacent libration at 157 cm^{-1}. The remaining librational modes are readily distinguished. The Debye temperature is very high as expected of such a rigid lattice.

Table 7.6

Intermolecular modes of $(CONH_2)_2$

Density of States cm^{-1}	Optical measurements cm^{-1}	Assignments
107	106	Ag
117 sh		
136	134	Ag
164 sh	157	Ag
	(165)	(Au-CCN torsion)

OXAMIDE

DENSITY OF STATES

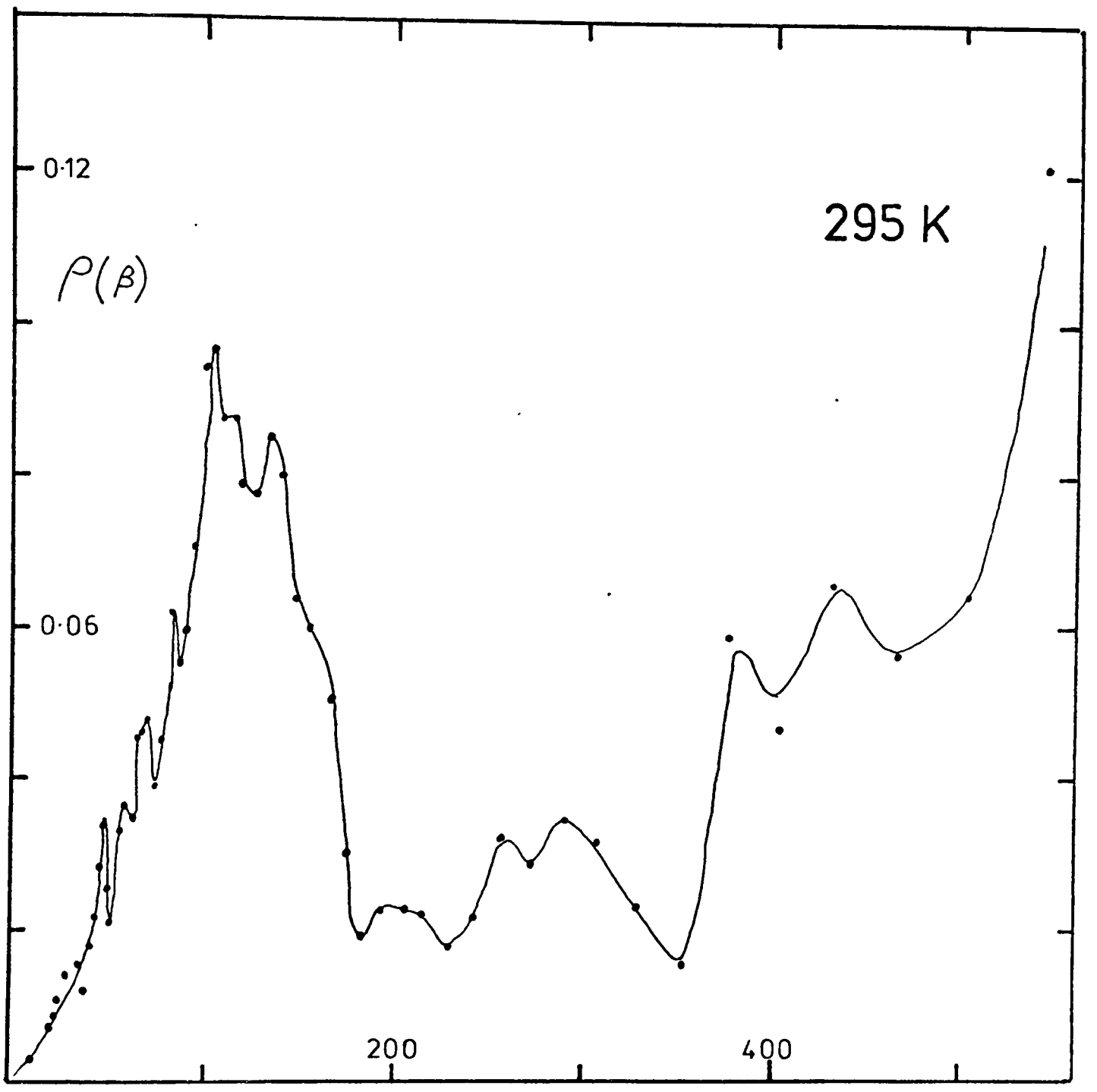


Fig. 7·17

Debye Temperature K 282

Deviation from Debye behaviour 42 cm^{-1}

The density of states of thiourea, from spectra measured on 6H are shown in figure 7.18, which show some extra details to the spectra of Rush, 1967. The structure at 293 K is orthorhombic, with four atoms per unit cell, space group Pnma. At low temperatures the complex balance of intermolecular forces is reflected by the existence of at least five phases, two of which are ferroelectric, in the neighbourhood of 170 K. The room temperature structure has been measured by X-rays, by Truter, 1967, and a neutron study by Elcombe and Taylor, 1968, who determine the librations about the three axes as being $\pm 4^{\circ}$, $\pm 11^{\circ}$ and $\pm 7^{\circ}$ about the axes 1, 2, 3 corresponding to the axes of urea. The rigid body hypothesis does not hold well at these temperatures, and this is invoked to explain deficiencies in a rigid body calculation of the optically active modes by Takahashi, Schrader, Meier and Gottlieb, 1967, (table 7.7), lattice modes are observed which should be forbidden on strict symmetry grounds; The positions of calculated bands are marked on the fig. 7.18. Emsley and Smith (1961) show that a reorientational motion similar to that in urea is observed, about the C-S axis. The linewidth transition occurs at 230 K, and no further change is observed by room temperature.

The density of states though reflecting some of the librational (Gerade) modes shows little structure as might be expected if the same mechanism was occurring as for urea, with the associated massive dispersion.

THIOUREA

DENSITY OF STATES

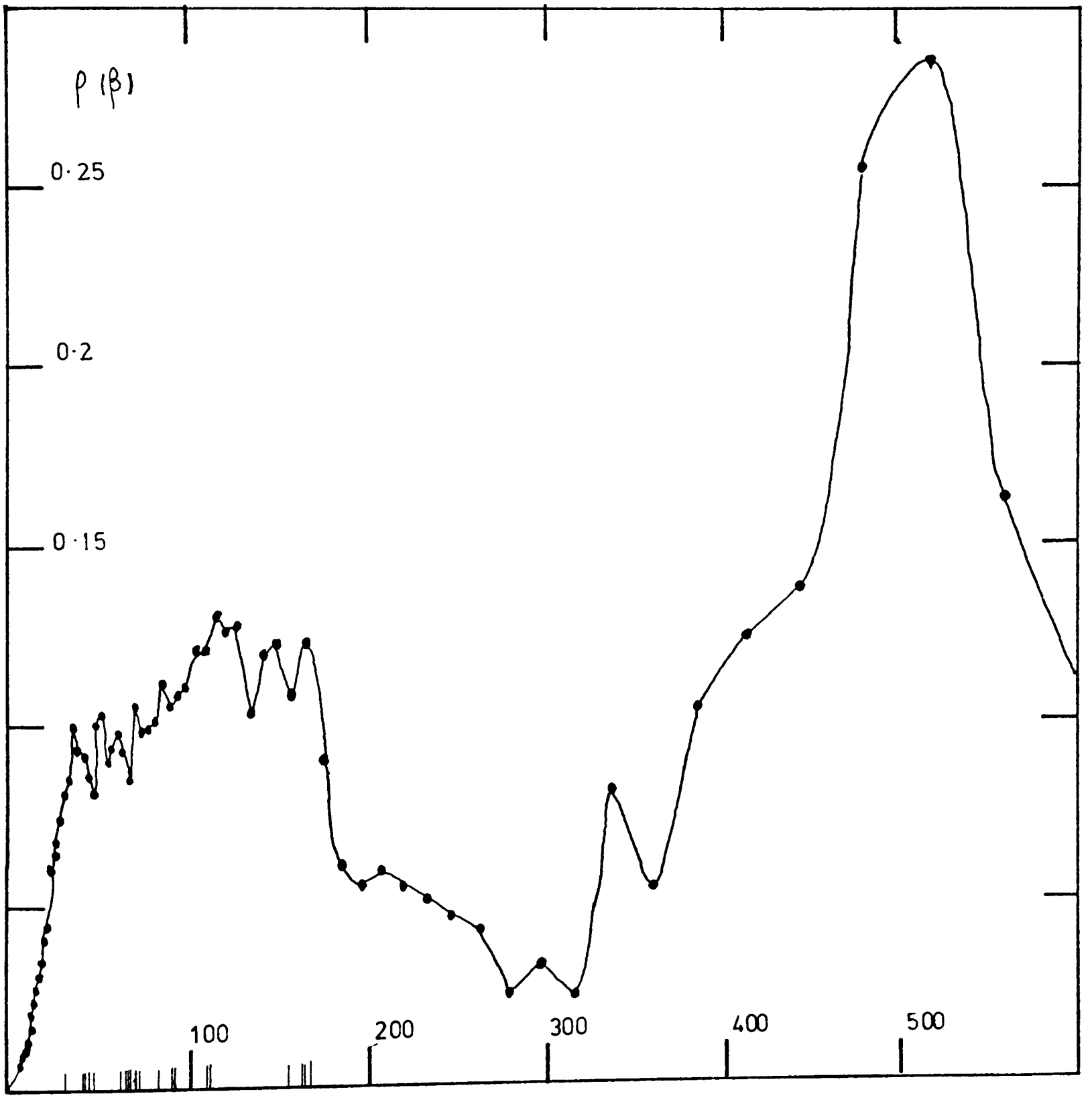


Fig. 7·18

Table 7.7

Intermolecular modes of $CS(NH_2)_2$

Density of States	Optical Measurements cm^{-1}		
cm^{-1}	Observed	Calculated	Assignment
36			
50	114	110	Ag
60		71	
70		29	
85		165	B_{1g}
115	94	91	
149		69	
165		90	B_{2g}
	60	60	
		45	
		169	B_{3g}
		63	
	44	42	
		156	Au
		91	
		38	
	90sh	83	B_{1u}
		67	
		0	
	163vs	165	B_{2u}
	(64)	65	
		0	
	106	109	B_{3u}
	42	40	
		0	

Debye temperature 143 K

Deviation from Debye behaviour 23 cm^{-1}

CHAPTER 8

The Measurement of Intramolecular Modes

8. The measurement of intramolecular modes

Inelastic neutron scattering is still a low resolution technique for determining the frequencies of normal modes of vibration of molecules when compared with readily available optical methods. The principal advantage of its use lies in the direct neutron nuclear interaction resulting in a differential cross-section fundamentally dependent on the displacement amplitudes of the atoms in the normal modes (eq. 1.42). Two systems will be briefly discussed here: the spectrum of the normal modes of naphthalene which lie below 1200 cm^{-1}; and the internal modes of urea in the same range of energy transfers.

8.1 Naphthalene

Two limitations of the utility of the time of flight spectrometer are the poor resolution at high energies, and the difficulty of obtaining statistically sound data with samples at low temperature. Since there is usually some coupling to the lattice modes at these low energies, dispersion effects are possible in the internal modes: Reynolds, Kjems and White, 1972, conclude that in their model system of p-$C_6H_4Cl_2$ and p -$C_6H_4Br_2$, the dispersion effects are in general less than the instrumental resolution, and that finite lifetimes of the optic phonons are the cause for the observed broadening at room temperatures, this being expressed in terms of a temperature dependent anharmonicity. This would also entail a multiphonon contribution manifesting itself as an increase in intensity proportional to Q^2 over the one phonon approximation arising from the terms in $(|Q.U|^2)^n$ in equation 6.4. The gradients of the extrapolations of the high energy modes do not deviate much from sonstant values.

The densities of states of $C_{10}H_8$ at 150 k, and 300 K, together with the density of states of $C_{10}D_8$ obtained from time

of flight experiments are shown in figure 8.1. The line spectrum is made up from the mean squared eigenvectors of the normal modes derived from the calculation of Cyvin and Cyvin, 1969. Though the relationship is evident, detailed comparison without the transformation to cartesian atom displacements is impossible. The relationship can however be compared to the spectrum of $C_{10}D_8$ since the atoms have similar scattering lengths, and the average overall nuclear displacements is observed. Accepting quite large frequency shifts for deuteration the correlations are reasonable. The grouped timing channels points corresponding to this spectrum are spaced apart by approximately one standard deviation of energy resolution. Corrections applied in obtaining $\rho(\beta)$ account for the general rise in the levels at higher energies where the data is poor initially.

The beryllium filter detector spectrometer has been used to extend these measurements to 1200 cm^{-1} at greater resolution. By using both the (311) and (511) aluminium monochromator planes, the take-off angle has been kept above 50^{o}. Under these conditions the resolution should be about 45 cm^{-1} FWHM, limited by the finite filter 'window'.

The spectrum of $C_{10}H_8$ measured at $90^{o}K$ and $4^{o}K$ is given in figure 8.2 together with the one phonon approximation to the spectrum using again the mean square of the eigenvectors. The rapid increase of the energy spread in the 'monochromatic' beam is evident at energies above 800 cm^{-1} for the uncorrected spectrum at 90 K. At $4^{o}K$ the corrected spectrum is shown. At very high take-off angles the beryllium filter dominates the resolution, dE, and again the corrected curve rises. The resolution estimated in the calculated spectrum was 48 cm^{-1} F.W.H.H. across the whole spectrum. The qualitative comparison with the

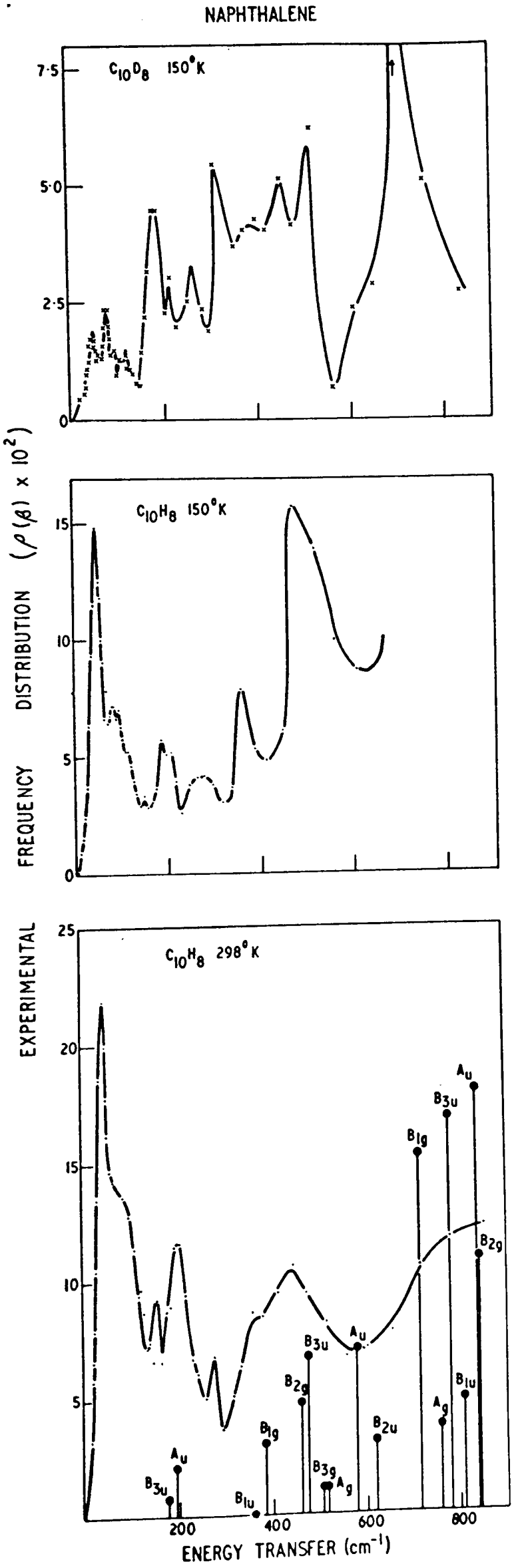

NAPHTHALENE
$C_{10}D_8$ 150°K
7·5
5·0
2·5
0
$C_{10}H_8$ 150°K
15
10
5
0
FREQUENCY DISTRIBUTION ($\rho(\beta)$ x 10^2)
EXPERIMENTAL
$C_{10}H_8$ 298°K
25
20
15
10
5
A_u
B_{3u}
B_{1g}
B_{2g}
B_{1u}
B_{2u}
B_{3g}
A_g
200
400
600
800
ENERGY TRANSFER (cm^{-1})

Fig. 8·1

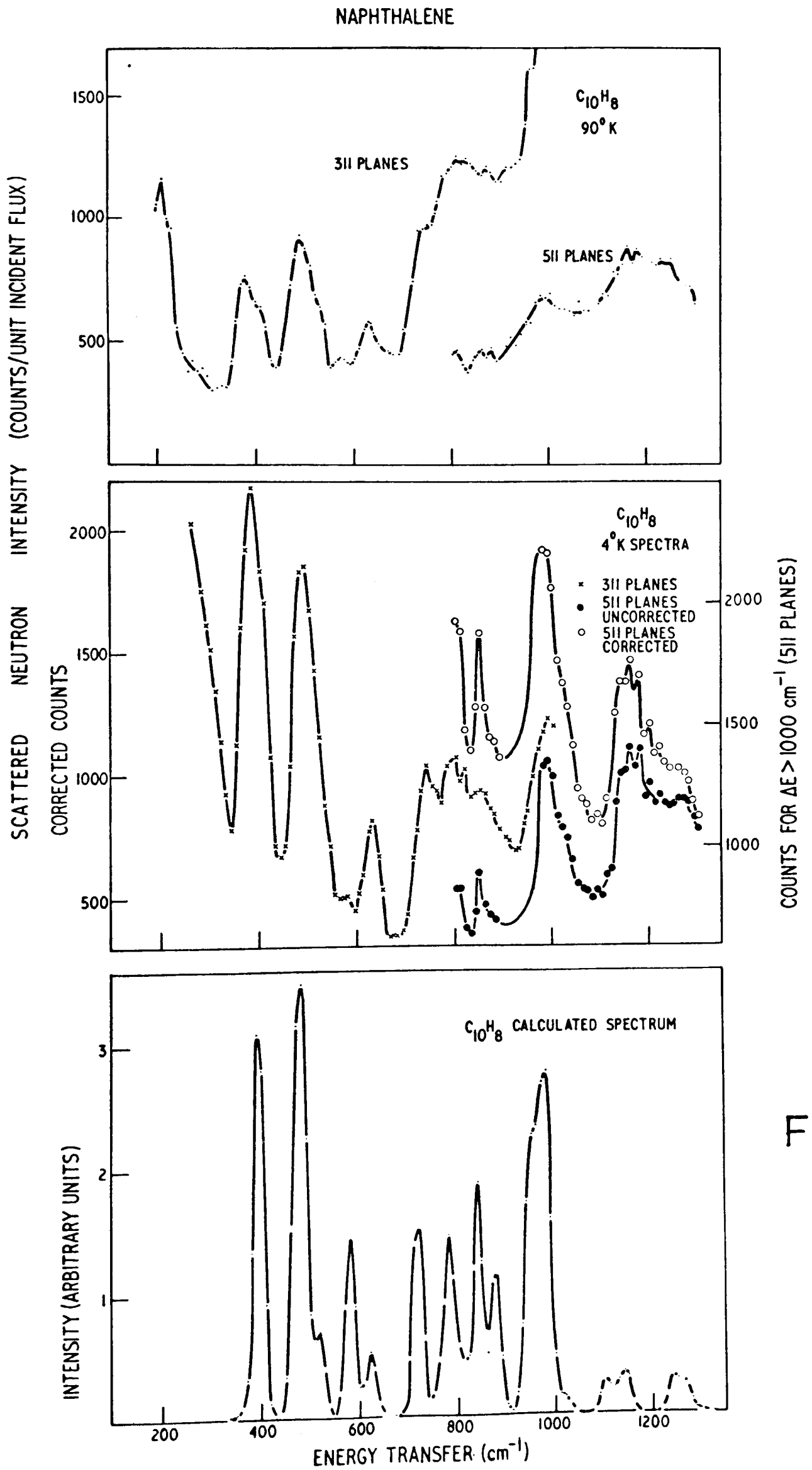

NAPHTHALENE
NEUTRON INTENSITY (COUNTS/UNIT INCIDENT FLUX)
$C_{10}H_8$
90°K
311 PLANES
511 PLANES
1500
1000
500
SCATTERED NEUTRON CORRECTED COUNTS
$C_{10}H_8$
4°K SPECTRA
311 PLANES
511 PLANES UNCORRECTED
511 PLANES CORRECTED
2000
1500
1000
500
COUNTS FOR ΔE > 1000 cm⁻¹ (511 PLANES)
$C_{10}H_8$ CALCULATED SPECTRUM
INTENSITY (ARBITRARY UNITS)
3
2
1
200
400
600
800
1000
1200
ENERGY TRANSFER (cm⁻¹)

Fig. 8-2

calculated spectrum is favourable but specific modes like the B_{1g} at 717 cm^{-1} are entirely absent in the neutron spectrum, though the mode is an out of plane hydrogen bending vibration which should give an intense neutron peak. To distinguish a multiphonon process the intensity of the B_{2u} mode at 618 cm^{-1} was studied at various angles over a range which allowed any Q^4 contributions to vary by 25%, but within the limits of reproducibility the scattering was isotropic. Each of the calculated eigenvalues of Cyvin had been fitted to a measured optic mode, so the initial assignments possibly have to be checked in greater detail. Lowering the temperature to 4 K does still give some improvement in the sharpening of peaks.

Table 8.1.

The intramolecular modes of Naphthalene

Density of States cm-1			Optic Modes cm-1
$C_{10}H_8$		$C_{10}D_8$	
150 K	298 K	170 K	
190	200	170	176
210	275	180	195
275	355sh	260	362
360	445	320	386
475	900 b	370	461
525sh		445	476
800 b		520	506
		720	512
			581
			618
			717
			763
			781
			809
			841
			845

Table 8 (Continued)

Beryllium Filter Spectra cm^{-1}		Calculated with Resolution of $47cm^{-1}$ FWHM
40K	90°K	
380	380	390
485	410 sh	-
580	490	480
-	535 sh	520
-	570	580
630	630	640
740	720 sh	720
795	790 sh	780
850	830	840
-	870	880
-		950 sh
985	990	980
1025sh	-	1100
1145	-	-
1160	1160	-
1180	-	1190
1265	1240	1260sh

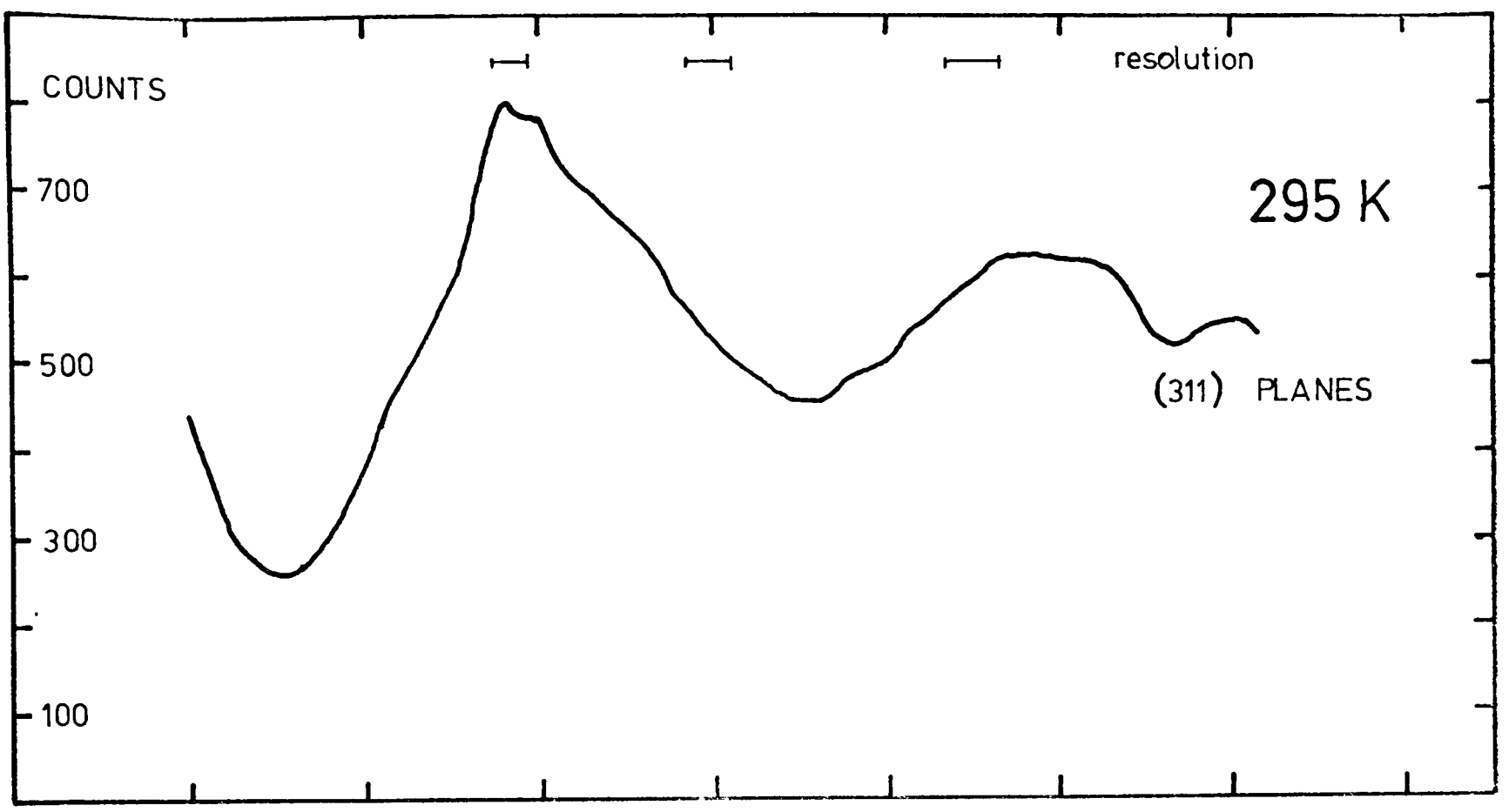
Table 8.2

Intramolecular modes of Urea

Neutron Spectrum cm^{-1}				Optical Measurement		
UH		UD		UH	UD	Assignment
90 K	295 K	90 K	295 K			
455		460	470		520w	NCN bend
550		520		560w	550w	NCN in plane rock
605	580	550		575w	720	NH_2 torsion
740				788	777	CONN out of plane bend
790					892	ND_2 rock
1020sh			1000	1005w		N-CN sym. stretch
					1052w	NHD rock
1140	1180			1147		NH_2 rock
					1212	NHD in plane stretch
					1247	ND_2 in plane bend

8.2 Urea

The characteristic amino group frequencies are not well enough resolved in the time of flight spectra to make accurate decisions on assignment. Complementary measurements were made using the beryllium filter technique both at 295 K and 90 K, fig. 8.3 Spectra of UD were also measured and are shown in fig. 8.4 Because of the weak dipole changes in the group vibrations these modes are difficult to assign using infra-red spectrometry. The problem that arises using the filter-technique is the effect of cooling on the samples of both UH and UD, explained by the contraction of the lattice and the whole system possibly becoming more harmonic with the smaller amplitude librations. The optical data given is that of Puranik, 1968, who has also performed a normal mode calculation for the CCNN skeleton, but this still leaves open the exact assignment of the three lowest branches. Assuming the horizontal hydrogen bonds become stronger (the lattice contracts more in this direction) then little change will be expected in the NCN in plane rock, nor will large deuteration shifts be seen. The NCN bend frequency would be higher for UH, and NH_2 and ND_2 torsions would be expected to shift to higher frequencies with the strengthening of the lattice. In a very strong lattice the mode with the largest amplitude will be the asymmetric NCN in plane rock, interacting least with the neighbours. Even at 90 K there appears to be some broadening of the mode at 450 cm^{-1}; while in the UD spectrum there appear to be additional modes at 300 cm^{-1}, but these may result from the rigid lattice modes.


$CO(NH_2)_2$
COUNTS
700
500
300
100
resolution
295 K
(311) PLANES

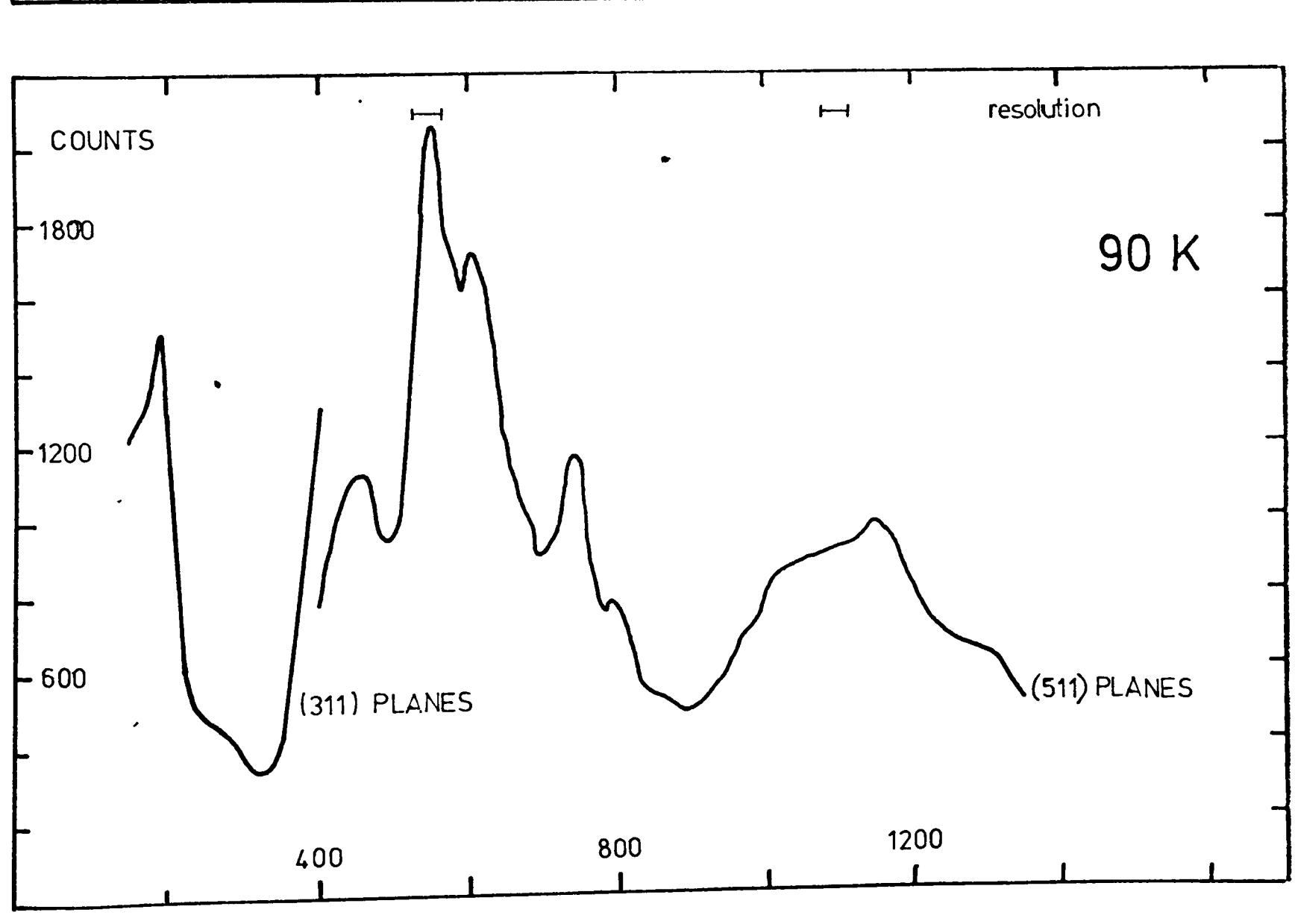
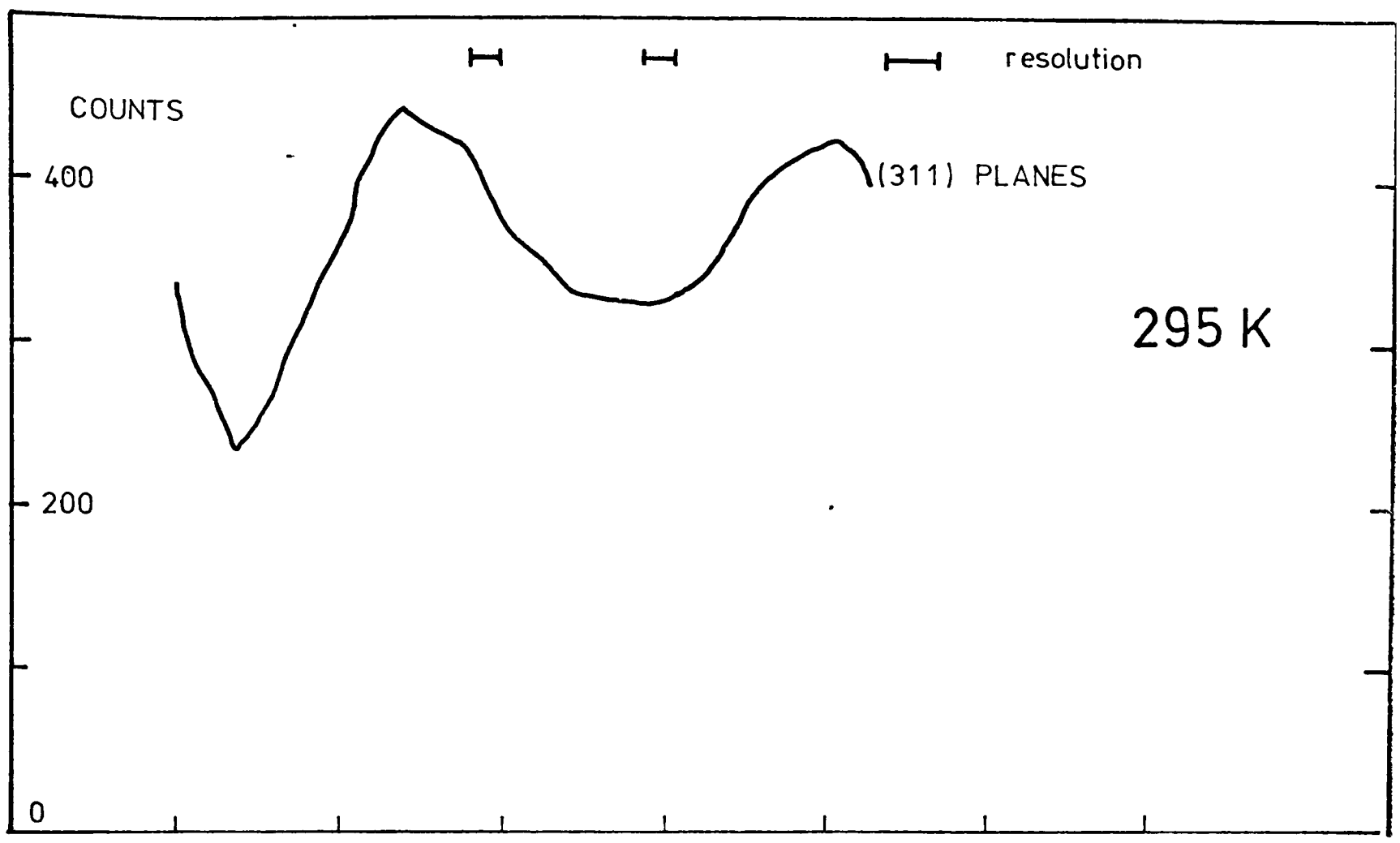
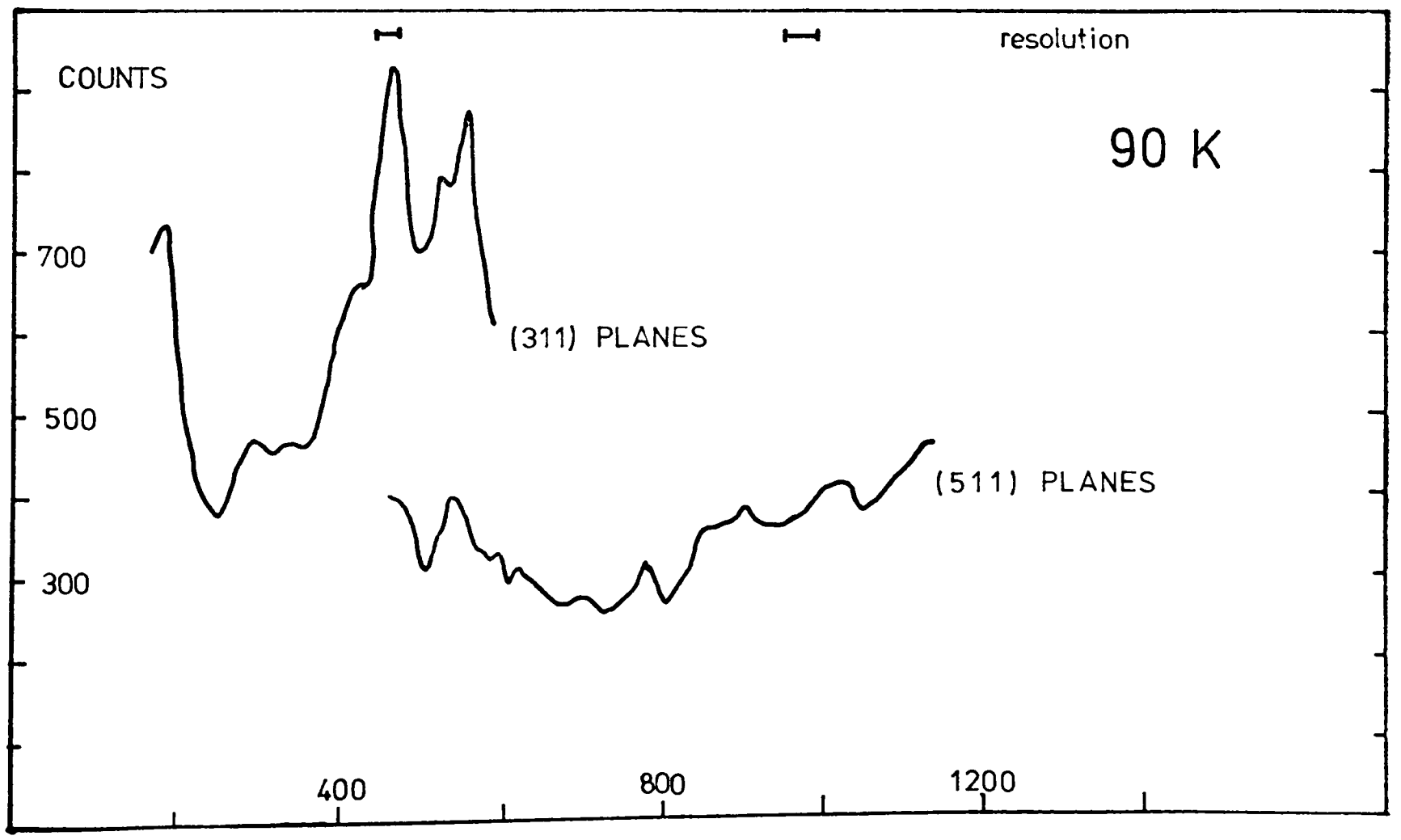

COUNTS
1800
1200
600
resolution
90 K
(311) PLANES
(511) PLANES
400
800
1200
ENERGY (cm^{-1})

Fig. 8·3

$CO(ND_2)_2$





ENERGY (cm^{-1})

Fig. 8·4

8.3 Conclusions

At the higher energy transfers both resolution and sensitivity of the neutron spectrometer in measuring the intramolecular mode frequencies are more limited than in readily available infra-red and Raman spectrometers. The advantages of incoherent neutron scattering are the large hydrogen cross-section and the intimate dependence of the differential cross-section in the nuclear displacements.

The motions of bound hydrogen closely follow the bonding atom and by this means group vibrations which do not directly include the proton are observed. A qualitative interpretation is readily made of a simple spectrum. For more complex cases where distinction is to be made between modes with similar characteristics only the full normal coordinate analysis, followed by conversion of the symmetry coordinates to atom cartesian coordinates is necessary to allow assignment. The filter spectrometer in general use is only semiquantitative since the thin samples required to reduce multiple scattering, multiphonon effects, and overall instrumental stability are difficult to predict, no simple sample lending itself well for use as a standard as vanadium does in the time-of-flight techniques. In addition to direct identification of normal modes of vibration, the coupling of these to the lattice motions may be observed from the increase in width of spectral features, though the resolution here is considerably limited by the use of beryllium as filter material. By using a polycrystalline filter with a larger real lattice, the transmission energy could be reduced from 40 cm^{-1}. The use of two filters successively in a different filter reduces the sensitivity still further.

Lattice vibrations may be studied by inference from the Brillouin centre optically active modes, and by acoustic measurements, though phosphorescence spectra may be used to probe the density of phonon states. Only neutron scattering techniques cover a sufficient range of energy and momentum transfer to allow full investigation across the Brillouin zone. Phonon cross-sections are small and coherent scattering poses considerable problems in measurement and analysis, but determination of the dispersion relations of the normal modes gives qualitative insight into the nature of the dynamics of the scatterer, and provides for a fundamental test of model calculations. The methods employed in these calculations always employ variable parameters adjusted to fit data available to minimise the difference. Complex solids normally have many more force constants than optically active modes and even by choosing specific interactions as being dominant, the parameterised model may be readily adjusted to fit the available data. Even though whole observed dispersion branches may be well fitted only symmetry directions are chosen for measurements for ease of analysis. Intensity measurements are proposed by Leigh, Szigeti and Newary (1971) as a test of model since these depend so specifically on the accuracy of the model. Though not so directly related to individual model parameters the density of phonon states as measured by incoherent neutron scattering provides a rather easier test for the normal coordinate analysis of both internal and lattice vibrations, and eventually, the combination of the two. An alternative refinement procedure to leave with the theoreticians is the refinement of a multiparameter model using the large numbers of phonons in off-symmetry directions in the Brillouin zone, which may be

easily obtained by the time-of-flight method. The identification here of twelve branches for two molecules suggests experimental limitation increase as rapidly as the model for more complex systems, but as shown by the experiments here even without these specialised calculations valuable deductions may be made from experiments alone for favourable systems.

Acknowledgements

The author thanks his supervisor, Dr. J.W. White for his enthusiastic guidance through this project and for all his valuable encouragement.

The experiments described in this thesis have been performed at A.E.R.E. Harwell, and grateful thanks is extended to the staff of Materials Physics Division for their generous help and advice for this work. Special acknowledgement is made to Mr. D.H.C. Harris for his able direction of the University support group.

References

Aldred B.K., (1969): Report USS/P16, unpublished.

Arnau J.L. and Giguere P.A. (1969), C.R. Acad, Sci. Paris 268B 245.

Ayerst, E.M. and Duke J.R.C. (1954), Acta Cryst 7, 588.

Becka L.N. (1962) J. Chem. Phys. 37 431.

Becka L.N. and Cruickshank, D.W.J., (1963), Proc. Roy. Soc. A273 455.

Born, M., and Huang, K., (1954). Dynamical theory of Crystal Lattices, Oxford.

Brockhouse, B.N., Becka, L.N., Rao, K.R. and Woods, A.D.B. (1963). Inelastic scattering of Neutrons in Solids and Liquids, IAEA, Vienna.

Bunce, L.J., Harris, D.H.C. and Stirling G.C. (1970) A.E.R.E. Report R6246.

Buyle-Bodin, M. (1957) C.R. Hebd. Seanc. Acad. Sci. Paris, 244 2495.

Caron, A. and Donohue, J. (1964) Acta. Cryst. 17 544.

Chen, S.H. and Dvorak, V. (1968). J. Chem. Phys. 48 4060.

Cheutin, A. and Mathieu, J.P., (1956), J. Chim. Phys. 53 106.

Chumbley, L., Dyer, R.F., Wallis D.E. (1968) J. Phys. E. Ser. II, 1, 528.

Cochran, W. (1960). Adv. In Phys. 9 387.

Cochran W. and Pawley, G.S. (1964), Proc. Roy. Soc. A273, 435.

Cochran, W. (1971) Lattice dynamics of Ionic and Coherent Crystals, C.R.C. Reviews in Solid State Sciences.

Couture-Mathieu, L. (1949), C.R. Acad. Sci. Paris 229 495.

Cruickshank, D.W.J. (1956), Acta. Cryst. 9 1005.

Cruickshank, D.W.J. (1957), Acta. Cryst. 10 504.

Cyvin, S.J., and Cyvin, B.N. (1969), J. Phys. Chem. 73 1430.

Das, T.P. (1957), J. Chem. Phys. 27 763.

Downes, J.S., Egelstaff, P.A. and White J.W. (1967). Chemistry in industry - Special publication on molecular sieves.

Duckworth, J.A.K. Willis B.T.M. and Pawley, G.S., (1969), Acta. Cryst. A25 482.

Durig, J.R., Brown S.C. and Hannum (1971), Mol. Cryst. and Liq. Cryst. 14 129.

Dyer, R.F. and Low, G.C. (1961). Inelastic scattering of Neutrons in Solids and Liquids, I.A.E.A., Vienna 179.

Egelstaff, P.A. (1962) Adv. in Phys. 11 203.

Egelstaff, P.A. and Schofield, P., (1962) Nucl. Sci. and Eng. 12 260.

Egelstaff P.A. (ed) (1965). Thermal Neutron Scattering, Academic Press, New York.

Elcombe, M.M. and Taylor, J.C. (1968), Acta. Cryst. A24 410 1968.

Emsley, J.W., and Smith, J.A.S. (1961), Trans. Faraday, Soc. 47 1233.

Fischer, G., and Zarembowitch, J. (1970), C.R. Acad. Sci. Paris, 270B 852.

Geddes, A.L., and Bottger, G.L. (1971), J. Chem. Phys. 55 1990.

Ghosh, R.E. (1971): Report USS/P18 unpublished.

Gordon, R.C. (1965), J. Chem. Phys. 43 1307.

Hadni, A. (1968), 'Phonons, Magnons and Excitons' (ed.) Zahlan, A.B., Cambridge.

Hahn, H., and Biem, W., (1963) Phys. Stat. Sol. 3 1911.

Hall, J. and Egelstaff, P.A., (1970) AERE Report R.6472.

Harada, J. and Shimanouchi, T. (1966), J. Chem. Phys. 44 2016.

Harris, D., Cocking, S.J., Egelstaff, P.A., and Webb, F.J. (1961). Inelastic scattering of Neutrons in Solids and liquids, IAEA, Vienna.

International Tables for X-ray Crystallography, (1960). The Kynoch Press, Birmingham.

Ito, M., Suzuke, M., and Yokoyama, T, (1968), 'Excitons, Magnons and Phonons' (ed.) Zahlan, A.B., Cambridge.

Kovalev O.V. (1965). Irreducible Representation of the Space Groups, Gordon and Breach, New York.

Kromhout and Moulton (1955), J. Chem. Phys. 23 1673.

Lefebre, J. and Wallart, F. (1970), C.R. Acad. Sci. Paris. 270B 227.

Leigh, R.S., Szigeti, B. and Tewary, V.K., (1971) Proc. Roy. Soc. A320 505.

Maradudin, A., Montroll, E.W., and Weiss, G.H., (1963). Solid State Physics, Suppl. 3, Academic Press, New York.

Haradudin, A.A. and Vosko, S.H., (1968), Rev. Mod. Phys. 40 1.

Marshall, W. and Lovesey, S.W. (1971). Theory of Thermal Neutron Scattering, Oxford.

Mckenzie, D.R. and Prior, A.W. (1971), J. Phys. C. 4 2304.

Meier, W. (1969), Dissertation, University of Munster.

Pawley, G.S. (1967), Phys. Stat. Sol. 20 347.

Pawley, G.S. and Yeats, E. (1969a), Solid State Comm. 7 385.

Pawley, G.S. and Yeats, E. (1969b), Acta. Cryst. B.25 2009.

Pawley, G.S. and Cyvin, S.J. (1970), J. Chem. Phys. 52 4073.

Page, D.I. (1968), Neutron Inelastic Scattering, Vol. I. IAEA, Vienna.

Peckham, G. (1965), J. Phys. Chem. Solids (Supplement) 1 49.

Powell, B.M. (1968). Neutron Inelastic Scattering IAEA, Vienna.

Prior, A.W. and Sanger, P.L. (1970), Acta. Cryst. A26 543.

Puranik, P.G. and Sirdeshmukh Lalitha (1968), Proc. Indian Acad. Sci. Sec. A., 67 99.

Rafizadeh, H.A. and Yip, S. (1970), J. Chem. Phys. 53 315.

Reynolds, P.A. Kjems, J., and White, J.W. (1972), J. Chem. Phys. 56 2940.

Reynolds, P.A., Kjems, J. and White, J.W. (1972), Neutron Inelastic Scattering, IAEA Vienna (to be published).

Richards, R.E. (1969), N.B.S. special publication no. 301 157.

Royston, J.R. (1962) Nucl. Inst. and Methods. 30 184.

Ruehrwein, R.A. and Huffman, H.M. (1946), J. Amer. Chem. Soc. 68 1759.

Rush, J.J. (1967), J. Chem. Phys. 47 4278.

Sklar, N., Senko, M.E., and Post, B. (1961). Acta. Cryst. 14 716.

Smith, G.W. (1962), J. Chem. Phys. 36 3081.

Sokolov, V.A. (1940), CA 34 5733.

Squires, G.L. (1966), Proc. Phys. Soc. 88 919.

Takahashi, H. Schrader, B., Meier, W., Gottlieb, K., (1967), J. Chem. Phys. 47 3842.

Gruter, M.R. (1967), Acta. Cryst. 22 556.

Turchin, V.F. (1965) 'Slow Neutrons), Israel program for scientific translations.

Twisleton, J.F. and White, J.W. (1972), Neutron Inelastic Scattering, IAEA Vienna (to be published).

Van Berkel (1958), Journee Automisation (Liege) Conference 74.

Van Hove, L. (1954) Phys. Rev. 95 249.

Van Vleck, J.H. (1948), Phys. Rev. 74 1184.

Vaughan, P. and Donohue, J. (1952), Acta. Cryst. 5 530.

Venkataraman, G. and Sahni, V.C., (1970), Rev. Mod. Phys. 42 409.

Waeber, W.B. (1969), J. Phys. C. Ser. 2, 2 903.

Worlton, T.C., and Warren, J.L., (1971) Phonons (ed.), Nusimovici, Flammarion Sciences Paris.

Wignall, G.D. (ed) (1967) A.E.R.E. Report M.1928.

Worsham, J.W., Levy, H.A. and Peterson (1957), Acta. Cryst. 10, 319.

Zemach, A.C. and Glauber, R.J. (1956), Phys. Rev. 101, 118.

List of Diagrams

Chapter 4

4.1 The DIDO cold neutron spectrometer 4H5.

4.2 Energy resolution of 7H and 4H5.

4.3 Momentum resolution of 7H and 4H5.

4.4 Accessible scans in (Q,ω) space.

4.5 Schematic diagram of a triple axis spectrometer.

4.6 The PLUTO triple-axis spectrometer

4.7 Crystal structure of urea

4.8 Crystallising apparatus for perdeutero urea.

4.9 Diffraction pattern from single crystal urea

Chapter 5

5.1 Results from the PLUTO triple axis experiments.

5.2 Brillouin zone of urea.

5.3 Experimental spectrum from urea.

5.4 Coherent scattering spectra of urea.

5.5 Graphical interpretation of phonon spectra

5.6 Measured dispersion curves along <001>

5.7 Measured dispersion curves along <110>

Chapter 6

6.1 Scattering by polycrystals.

6.2 The DIDO longwavelength spectrometer 6H

6.3 The 4H5 sample changer

6.4 The beryllium filter detector spectrometer.

Chapter 7

7.1 Hexamethylenetetramine: density of states spectrum.

7.2 Naphthalene: density of states spectra.

7.3 Naphthalene (d_8): density of states spectra.

7.4 Napthalene (d8): comparison of model with experimental spectra.

7.5 Urea: neutron diffraction by polycrystalline specimens.

7.6 Urea: time of flight spectra at 90 and 170 K.

7.7 Urea: time of flight spectra with 4.2 and 5.1 Å incident neutrons.

7.8 Urea: time of flight spectra at 390 and 413 K.

7.9 Urea: density of states spectra.

7.10 Urea (d_4): time of flight spectra at 190°K.

7.11 Urea (d_4): time of flight spectra with 4.2 and 5.2 Å incident neutrons.

7.12 Urea (d_4): density of states spectra.

7.13 Urea: extrapolation plots.

7.14 Urea (d_4) Crystal: time of flight spectra at two orientations.

7.15 Urea (d_4) Crystal: density of states in two directions.

7.16 Urea: calculated dispersion curves.

7.17 Oxamide: density of states spectrum.

7.18 Thiourea: density of states spectrum.

Chapter 8.

8.1 Naphthalene: density of states of intramolecular modes.

8.2 Naphthalene: neutron energy loss spectrum.

8.3 Urea: neutron energy loss spectrum.

8.4 Urea (d_4): neutron energy loss spectrum.